OUKA
The University of Osaka
Institutional Knowledge Archive

Title	Mechanisms of Thermal Atomic Layer Etching (ALE) for Metals
Author(s)	Yassin, Abdulrahman Hikmat Basher
Citation	大阪大学, 2020, 博士論文
Version Type	VoR
URL	https://doi.org/10.18910/77486
rights	
Note	

The University of Osaka Institutional Knowledge Archive : OUKA

https://ir.library.osaka-u.ac.jp/

The University of Osaka

Doctoral Dissertation

Mechanisms of Thermal Atomic Layer Etching (ALE) for Metals

Abdulrahman Hikmat Basher Yassin

June 2020

Quantum Engineering Design Course (QEDC)

Center for Atomic and Molecular Technologies

Graduate School of Engineering

OSAKA UNIVERSITY

Acknowledgments

First of foremost, I want to express my deep and sincere gratitude to my supervisor Prof. Satoshi Hamaguchi. It has been a great honor to be his Ph.D. student. I am thankful for the opportunities he has offered making me progress in my academic career. He has been always encouraging me to continue the research with great enthusiasm. Prof. Hamaguchi was not only a supervisor, he was giving unlimited support as a father to his son.

I am sincerely grateful to Prof. Ikutaro Hamada who was hand-to-hand with me to pass several difficulties and for developing my work. His constructive comments and suggestions helped me to further improve my research.

I would like to acknowledge Prof. Kazuhiro Karahashi and Dr. Tomoko Ito thoughtful advice on the experimental background of this research and Dr. Michiro Isobe for the kind advice in the weekly group meeting.

I also gratefully acknowledge Osaka University for financial support.

For the great opportunity to study at Karlsruhe Institute of Technology (KIT), I would like to show my greatest appreciation to Prof. Wolfgang Wenzel. I am particularly indebted to Dr. Marjan Krstić and Dr. Karin Fink who gave insightful comments and suggestions for my calculations and I have appreciated their collaboration. I also appreciate the support from Professional Development Consortium for Computational Materials Scientists (PCoMS), which allowed him to visit Prof. Wolfgang Wenzel and Dr. Marjan Krstić for the first time and the second time was supported by the Japan Society for the Promotion of Science (JSPS) Grants-in-Aid for Scientific Research (S) 15H05736, JSPS

Core-to-Core Program JPJSCCA2019002, and Germany`s Excellence Strategy – 2082/1 – 390761711 and GRK 2450.

I also thank Prof. Takae Takeuchi, Prof. Masato Kiuchi, and Dr. Pascal Friederich for helpful discussions and comments.

I am also thankful to all the members and staff in Hamaguchi group. They are so friendly and always eager to help. I could feel their eagerness pulling at me. Their warm friendship makes me feel like home so I can focus more on my studies.

For this dissertation, I would like to thank my dissertation committee members, Prof. Yoshitada Morikawa, Prof. Tamio Oguchi, and Prof. Ikutaro Hamada who have shared their valuable time for discussions and comments to further refine and improve this dissertation from both theoretical and experimental perspectives.

Lastly, I would like to express my deepest love to my mother, my father, and my family for supporting and encouraging me. They are my source of power. With their love and support, I am able to have a happy abroad life in japan and continue my research with confidence. Therefore, I dedicate this work to them.

Abdulrahman Hikmat Basher Yassin

June 2020

Osaka University

Abstract

Atomic layer etching (ALE) is one of the vital manufacturing technologies that is used to contrive nano-scale electronic devices as it can be utilized for precise and damageless etching of substances. Materials and metals can be etched layer by layer in a controlled manner, typically starting with the modification step of the metal surface followed by the removal step to remove the modified layer(s). These two steps or a cycle will be repeated to decrease the film thickness precisely and at least one of these steps must be stopped automatically without a temporal adjustment of process conditions that is called sequential self-limiting reactions.

The early and widely used ALE technique for metals was based upon etching the top thin layer of the metal surface that has been either oxidized or halogenated (the surface modification step) followed by low energy (less than physical spattering energy) ion bombardments for anisotropic ALE. However, ion bombardment may cause atomic-scale surface damages even at low ion incident energy. Therefore, a new thermal ALE technique has been investigated for isotropic etching processes.

Thermal atomic layer etching (ALE) may be used for difficult-to-etch materials precisely such as Ni, Co, NiFe, MgO, and CoFeB, which can be used for magneto-resistive random access memory (MRAM) devices. In thermal ALE, volatile molecules are employed instead of ion bombardment that can be desorbed as a metal complex when the surface temperature is increased. For example, thermal ALE for a Ni surface by organic molecule has been studied experimentally. It can be performed in the following manner: First, the surface of a Ni film is modified to form a thin nickel oxide (NiO) layer. Second,

the film is exposed to a hexafluoroacetylacetone (hfacH) gas. If the surface temperature is in the range of 300 ~ 400 °C, volatile nickel hexafluoroacetylacetonate $Ni(hfac)_2$ and water H_2O molecules that are formed on the surface and the NiO layer is removed. In this process, no further etching occurs after the NiO layer is removed and a new metallic Ni surface appears, which ensures the self-liming nature of this process. In contrast, when hfacH is exposed to a metallic Ni surface, it decomposes and does not form $Ni(hfac)_2$ complexes or H_2O molecules and therefore no etching of Ni takes place.

The main goal of this study is to provide qualitative insight into the mechanisms of the adsorption of hfacH on a NiO surface, formation and desorption of $Ni(hfac)_2$ complexes and H_2O molecules that can process thermal ALE of a Ni surface after its oxidization. Moreover, this work aims to prove the self-limiting nature of thermal ALE for Ni with an hfacH gas by confirming the decomposition of hfacH molecules on a metallic Ni surface that clarifies the experimental observations. These goals have been achieved in this study as the following:

First, the stability of the adsorbate enol hfacH on NiO fcc (100) and metallic Ni fcc (100) monolayers was examined using density functional theory (DFT) with the B3LYP functional. It was shown that an hfacH molecule could be deprotonated and form a hexafluoroacetylacetonate anion ($hfac^-$) bonded stably with positively-charged Ni atoms of the surface. On a metallic Ni surface, however, an hfacH molecule can be unstable and dissociated. The results are qualitatively consistent with observations of the interaction of hfacH with NiO and Ni surfaces in earlier experiments. The results also explain the mechanisms of the adsorption steps in thermal atomic ALE of Ni-based on the cyclic processes of surface oxidation and formation of volatile organo-nickel complexes.

Second, adsorption of hfacH molecules was evaluated on a NiO fcc (100) surface with more realistic surface material models, the possible formation and desorption of volatile nickel hexafluoroacetylacetonate $Ni(hfac)_2$ on a NiO surface was investigated. Dispersion corrected DFT (PBE-D3, PBE0-D3, and B3LYP-D3) and the cluster embedding method were used. It has been confirmed that an hfacH molecule approaching a NiO surface deprotonates without a potential barrier and adsorb on the surface exothermically with the adsorption energy close to that obtained in the previous study. In this study, stable adsorption of two deprotonated hfacH molecules on a NiO (100) surface was found to occur not on a single Ni atom but over a few Ni atoms instead, which makes the formation of a $Ni(hfac)_2$ complex on the flat surface very unlikely even at elevated temperature. However, if the surface is rough and a Ni atom protrudes from the surrounding atoms, two $hfac^-$'s can bond to the Ni atom stably, which suggests a possibility of desorption of a $Ni(hfac)_2$ complex from the surface at elevated temperature. Given the experimentally observed fact that desorption of $Ni(hfac)_2$ complexes typically takes place on a NiO surface at a temperature of 300 ~ 400 °C, our DFT calculations indicate that surface roughness of oxidized Ni surface facilitates the formation and desorption of organometallic complexes $Ni(hfac)_2$, and therefore, the resulting Ni surface after ALE can be smoother than the initial surface.

After the adsorption and desorption mechanisms of thermal ALE processes of a NiO surface by hfacH molecules were explained, the interaction between hfacH molecules with a metallic Ni surface was studied to prove the etching processes will be stopped automatically, i.e., called self-limiting, once NiO layers are removed which is the third part of this work. A precise evaluation of the adsorption energies for deprotonated and

dissociated hfacH molecules on periodic Ni fcc (100), (110), and (111) surfaces have been investigated using periodic DFT with van der Waals density functional. An hfacH molecule is found unlikely to be deprotonated, i.e., to break an O-H bond of hfacH. Rather, it is more likely to be dissociated, e.g., one of the possible dissociations is defluorination, i.e., breaking of an F-C bond. Therefore, hfacH will be decomposed once a Ni surface appears that ensures the self-liming nature of this process. In this way, the simulation demonstrated the self-limiting nature of thermal ALE for Ni with an hfacH gas. The results are qualitatively consistent with the experimental observations.

In this study, mechanisms of thermal ALE for a Ni surface after its oxidization was investigated using hfacH molecules as an organic gas. These mechanisms are not limited to thermal ALE for a Ni surface with hfacH molecules as an etchant gas. They can be generalized for any metals with different organic gases, at least a β-diketone type such as acetylacetone (acacH) and trifluoroacetylacetone (tfacH) gases, that are deferred for future studies.

Contents

Title ····· **I**

Acknowledgments ····· **II**

Abstract ····· **IV**

Contents ····· **VIII**

List of figures ····· **XII**

List of tables ····· **XVIII**

CHAPTER 1: Introduction ·····**- 1 -**

1.1 Atomic layer etching (ALE) and its importance·····**- 2 -**

1.2 ALE categories ·····**- 2 -**

1.2.1 Plasma-enhanced ALE ·····**- 2 -**

1.2.2 Thermal ALE ·····**- 4 -**

1.3 Motivation for this study and the literature ·····**- 8 -**

1.4 Objective of this study ·····**- 9 -**

1.5 Structure of this thesis·····**- 11 -**

1.6 References ·····**- 13 -**

CHAPTER 2: Theoretical and Computational Fundamentals ·····- 16 -

2.1 Introduction ·····- 17 -

2.2 Many-particle Schrödinger equation ·····- 17 -

2.3 Hartree-Fock approximation·····- 19 -

2.4 Density functional theory (DFT)·····- 22 -

2.4.1 Hohenberg-Kohn theorem ·····- 23 -

2.4.2 Kohn-Sham density function theory·····- 23 -

2.4.3 Exchange-correlation functionals ·····- 26 -

a. The local density approximation (LDA) and the generalized gradient approximation (GGA) ·····- 26 -

b. Hybrid exchange-correlation functionals ·····- 27 -

2.5 Dispersion correction ·····- 29 -

2.5.1 Dispersion correction by Grimme (DFT-D2/DFT-D3) ·····- 30 -

2.5.2 The van der Waals density functional (vdW-DF) ·····- 33 -

2.6 Basis function ·····- 36 -

2.6.1 Gaussian type orbital ·····- 36 -

2.6.2 Plane wave basis ·····- 36 -

2.7 Pseudopotential or effective core potential (ECP) ‥- 38 -

2.8 References ……- 39 -

CHAPTER 3: Stability of Hexafluoroacetylacetone Molecules on Metallic and Oxidized Nickel Surfaces in Atomic Layer Etching (ALE) Processes ……- 44 -

3.1 Introduction ……- 45 -

3.2 Methodology ……- 45 -

3.3 Results and discussion ……- 49 -

3.4 Summary ……- 60 -

3.5 References ……- 62 -

CHAPTER 4: Formation and Desorption of Nickel Hexafluoroacetylacetonate Ni(hfac)$_2$ on a NiO Surface in Atomic Layer Etching (ALE) Processes ……- 65 -

4.1 Introduction ……- 66 -

4.2 Methodology ……- 67 -

4.3 Results and discussion ……- 74 -

4.4 Summary ……- 86 -

4.5 References ……- 89 -

CHAPTER 5: Self-Limiting Processes in Thermal Atomic Layer Etching (ALE) of Nickel by Hexafluoroacetylacetone ····- 92 -

5.1 Introduction ·····- 93 -

5.2 Methodology ·····- 94 -

5.3 Results and discussion ·····- 95 -

5.4 Summary ·····- 101 -

5.5 References ·····- 103 -

CHAPTER 6: Summary·····- 106 –

Research Achievement ·····- 113 –

List of figures

Figure №	Page
Fig. 1-1: Concept of plasma-enhanced ALE of Al_2O_3 using BCl_3 radicals and Ar-plasma	4
Fig. 1-2: Concept of thermal ALE of a Ni surface using O and hfacH gases	6
Fig. 1-3: Interaction between a Ni surface with hfacH molecules	7
Fig. 3-1: Top views of the single-monolayer surface models used in the simulations. (a) 8.89 × 8.89 $Å^2$ square (100) surface of fcc NiO and (b) 7.48 × 4.98 $Å^2$ rectangular (100) surface of fcc Ni.	48
Fig. 3-2: Simulated optimized structures of (a) keto-type and (b) enol-type hfacH molecules. The enol-type hfacH is more stable than the keto-type, with an energy difference of −0.285 eV.	49
Fig. 3-3: NBO charge distribution from -1.5 *e* (red color) to 1.5 *e* (green color) of (a) keto-type and (b) enol-type hfacH molecules. It is seen that oxygen atoms are most negatively charged in each molecule.	50
Fig. 3-4: NBO charge distribution from -1.5 *e* (red color) to 1.5 *e* (green color) of model surfaces of (a) NiO and (b) Ni given in Fig. 3-1. It is seen that NiO is an ionic crystal that consists of positively-charged Ni and negatively-charged O atoms whereas Ni of the metallic surface is nearly charge neutral.	51
Fig. 3-5: "NiO + hfacH", where an hfacH molecule is vertically placed on a NiO monolayer; (a) front view and (b) side view.	52

Figure №	Page
Fig. 3-6: "NiO + inv. hfacH", where an inverted hfacH molecule is vertically placed on a NiO monolayer; (a) front view and (b) side view.	53
Fig. 3-7: "NiO ~ 56° hfacH", where an hfacH is tilted at an angle of 56° on a NiO monolayer; (a) front view and (b) side view.	53
Fig. 3-8: Interaction energies between the NiO surface and hfacH molecules with the three different orientations given in Figs. 3-5, 3-6, and3-7 as a function of the distance between the surface and the hfacH molecule, defined as the position of the O atoms of the hfacH molecule measured from the NiO surface plane. It should be noted that no geometry optimization is performed in this simulation so that the atomic configuration of an hfacH atoms is the same as that of Fig. 3-2(b) (of enol type) and the surface model is given by Fig. 3-4(a). The curves and lines are guides for the eye.	54
Fig. 3-9: Optimized structure of an hfacH adsorbed on the NiO model surface; (a) front view and (b) side view. It is seen that, after structure optimization of hfacH (with a fixed NiO structure), hfacH is deprotonated and $hfac^-$ is stably bonded with the surface.	56
Fig. 3-10: NBO charge distribution from -1.0 *e* (red color) to 1.0 *e* (green color) of the system given in Fig. 3-9.	57
Fig. 3-11: Optimized structure of an hfacH molecule placed near a metallic Ni model surface given in Fig. 3-1(b); (a) front view and (b) side view.	59
Fig. 3-12: NBO charge distribution from -1.0 *e* (red color) to 1.0 *e* (green color) of the system given in Fig. 3-11.	59

Figure №	Page
Fig. 4-1: Atomic configurations of the NiO four shell surface material model used in our DFT calculations. All atoms are in the lattice sites of the rectangular NiO crystalline structure with a dimension of $29.33 \times 29.33 \times 18.86$ $Å^3$, having a (100) top surface. It consists of the QM region, represented by the collection of gray, red, and green spheres located near the center of the top surface and the embedding region represented by the blue and red dots occupying the NiO lattice sites outside the QM region. All calculations were performed for this rectangular box in the presence of the embedding region with different models of the QM region. Here, gray, red, and green spheres represent Ni, O, and Mg atoms, respectively, and blue and red dots represent PCs. For details, the reader is referred to the main text.	68
Fig. 4-2: Optimized structures of the (a) "four shell model" and (b) "six shell model" of the QM region having a NiO (100) surface, whose arrangement of atoms is given in Table I.	69
Fig. 4-3: Optimized structures of rough surface models with (a) Ni and O atoms added to the surface of the four shell model and (b) 5 Ni and 5 O atoms arranged in a pyramid-like structure added to the four shell model.	73
Fig. 4-4: Optimized structure of an enol-type hfacH molecule. Here, dark gray, red, blue, and white spheres represent C, O, F, and H atoms, respectively.	74
Fig. 4-5: Optimized structure of the four shell model for a NiO (100) surface with an adsorbed hfacH molecule after deprotonation.	75
Fig. 4-6: Mulliken partial charge distribution state of Fig. 4-5.	77

Figure №	Page
Fig. 4-7: Optimized structure of a $Ni(hfac)_2$ complex. Here, dark gray, red, blue, and white spheres represent Ni, O, F, and H atoms, respectively.	77
Fig. 4-8: Optimized structure of the four shell model for a NiO (100) surface with two adsorbed hfacH molecules after deprotonation.	78
Fig. 4-9: Optimized structures of the rough surface models of (a) Figs. 4-3 (a) and 4-3 (b) with two adsorbed hfacH molecules after deprotonation. In each surface, a $Ni(hfac)_2$-like structure is formed around the topmost Ni atom.	79
Fig. 4-10: System energy as a function of the position of the topmost Ni when two hfacH molecules are adsorbed around the protruding Ni atom of a rough surface. The black and red curves represent the cases of Figs. 4-9 (a) and 4-9 (b). The abscissa represents the distance of the Ni atom measured from its initial position given in Fig. 4-9 in each case. The ordinate represents the change in energy measured from the initial system energy prior to adsorption, i.e., the total energy of the system consisting of the surface material model of Fig. 4-3 and two hfacH molecules of Fig. 4-4 away from the surface.	81
Fig. 4-11: System energies of different states of atomic configurations. The initial state prior to the adsorption of two hfacH molecules on the rough surface of Fig. 4-3 (a) is depicted in (a), where the system energy is set to be zero. The state of two hfacH molecules adsorbed on the surface [i.e., Fig. 4-9 (a)] is shown in (b). The final state where both an H_2O molecule and a $Ni(hfac)_2$ complex have desorbed from the surface is depicted in (c). The structural optimization among all Ni, O, C, F, and H atoms was performed for each state.	82

Figure №	Page
Fig. 4-12: System energies of different states of atomic configurations. The initial state prior to the adsorption of two hfacH molecules on the rough surface of Fig. 4-3(b) is depicted in (a), where the system energy is set to be zero. The state of two hfacH molecules adsorbed on the surface [i.e., Fig. 4-9 (b)] is shown in (b). The state of H_2O molecule desorption from (b) while two hfac groups remain adsorbed on the surface is presented in (c). The final state where both an H_2O molecule and a $Ni(hfac)_2$ complex desorbed from the surface is depicted in (d). The structural optimization among all Ni, O, C, F, and H atoms was performed for each state.	83
Fig. 4-13: The energy diagram of Fig. 4-11 including a similar H_2O desorption state.	84
Fig. 4-14: System energies of different states of atomic configurations. The initial state prior to the adsorption of two hfacH molecules on the Ni (100) surface of Fig. 4-2(a) is depicted in (a), where the system energy is set to be zero. The state of two hfacH molecules adsorbed on the surface [i.e., Fig. 4-8] is shown in (b). The state of H_2O molecule desorption from (b) while two hfac groups remain adsorbed on the surface is presented in (c). The final state where both an H_2O molecule and a $Ni(hfac)_2$ complex desorbed from the surface is depicted in (d). The structural optimization among all Ni, O, C, F, and H atoms was performed for each state.	85
Fig. 5-1: (a) Top and (b) side views of an hfacH molecule physisorbed on a Ni (100) surface.	96

Figure №	Page
Fig. 5-2: (a) Top and (b) side views of an hfacH molecule physisorbed on a Ni (110) surface.	96
Fig. 5-3: (a) Top and (b) side views of an hfacH molecule physisorbed on a Ni (111) surface.	97
Fig. 5-4: (a) Top and (b) side views of an hfacH molecule chemisorbed on a Ni (110) surface.	98
Fig. 5-5: (a) Top and (b) side views of the charge density difference of hfacH on a Ni (110) surface. The red (blue) isosurface indicates negative (positive) charge accumulation.	98
Fig. 5-6: Energy diagram of the deprotonation process of an hfacH molecule on a Ni (110) surface obtained with CINEB calculation.	99
Fig. 5-7: Energy diagram of the defluorination (dissociation) process of a hfacH molecule on a Ni(110) surface obtained with the CINEB calculation.	101

List of tables

Table №	Page
TABLE 4-1: Information on atomic configurations in the QM regions of two NiO surface material models used in this study. In the "Coordinates" column, "Fixed" indicates that the atoms listed in the same row are set immobile during structural optimization.	71
TABLE 4-2: Reaction energies of Fig. 4-5 for the adsorption of a single hfacH on a NiO (100) surface, evaluated with different functionals and assumptions of the dispersion effects.	76

CHAPTER 1:

Introduction

1.1 Atomic layer etching (ALE) and its importance

Atomic layer etching (ALE) is one of the key manufacturing technologies for nano-scale electronic devices as it can be used for precise and damageless etching of materials [1-3]. It is a technique to etch materials layer by layer in a controlled manner, typically repeating a cycle of a surface modification step and a step to remove the surface layer affected by the preceding step [4-8]. In ALE, at least one of the steps must be self-limiting in a sense that the surface modification or removal step ends automatically without a temporal adjustment of process conditions [9-12]. In general, ALE is considered as the reverse of atomic layer deposition (ALD) [3,6]. ALE and ALD together enable the atomic layer with highly controlled removal and growth of materials, which are based on sequential and self-limiting reactions [6,12]. They were first investigated in the 80's of the last century and several papers have been published as well in the 90's [13-18]. However, these techniques were not interested at that time since microdevices were in the range of micro-scale, which made using these techniques so expensive as too much time would be needed to fabricate those devices. In contrast, their practical importance has grown rapidly in recent years as they have been applied for the manufacturing of semiconductor devices whose dimensions are approaching the atomic scale [4,10,19,20].

1.2 ALE categories

In general, ALE processes may be divided into two groups as follows:

1.2.1 Plasma-enhanced ALE

In a typical plasma-enhanced ALE, a modified surface layer is removed by the impact of low-energy plasma-generated ions incident upon the surface [7,10,11,19-21].

The surface modification may also be performed with free radicals generated by chemically reactive plasmas. The kinetic energy of incident ions is set sufficiently low so that the etching process automatically stops once the chemically modified surface layer is completely removed. The major advantages of plasma-enhanced ALE are that the etching can be performed at low surface temperature and anisotropic etching can be achieved owing to the directionality of incident ion motion. Possible disadvantages of plasma-enhanced ALE are that ion bombardment may cause atomic-scale surface damages even at low ion incident energy and ions with energy lower than the etching threshold energy will be deposited on the surface [7,8,10,11]. For example, K.S. Min *et al*. (2013) reported the processes of plasma-enhanced ALE of aluminum oxide (Al_2O_3) using boron tri-chloride (BCl_3) radicals and argon (Ar) plasma as shown in Fig. 1.1 [20]. First, the sample will be prepared by covering areas that do not want to be etched by polymethyl methacrylate (PMMA) mask, as shown in Fig 1.1 (a). Second, a monolayer of BCl_3 will be deposited and adsorbed on an Al_2O_3 surface that will weaken the bonds in the surface which will interact with BCl_3 molecules, as shown in Fig 1.1 (b). Then by switching on Ar-plasma, $AlCl_3$ and BClO molecules will be desorbed, i.e., Fig 1.1 (c), and a monolayer of Al_2O_3 will be etched as shown in Fig. 1.1 (d). The $AlCl_3$ and BClO molecules are formed and desorb from the surface through the reaction:

$$Al_2O_3 + 3BCl_3 \xrightarrow{\text{Ar plasma}} 2AlCl_3 + 3BClO$$

There is no etching occurred once the BCl_3 layer is removed, i.e., self-limiting, because the energy of used plasma is much less than the physical spattering energy of Al_2O_3. This is known as a full cycle that will be repeated to etch Al_2O_3 substrate layer by layer using a plasma-enhanced ALE technique.

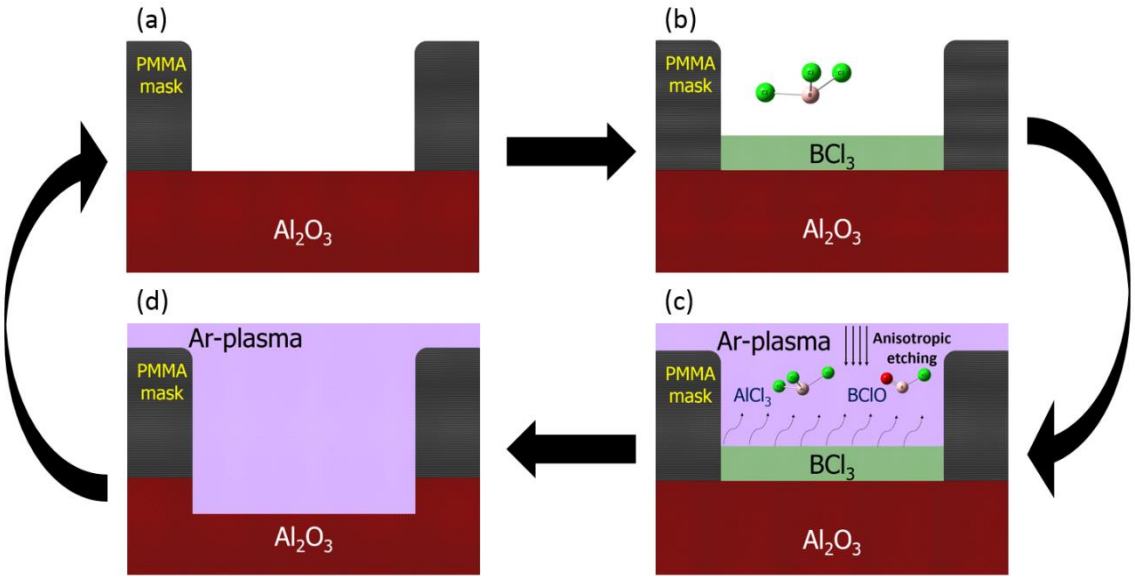


Fig. 1-1: Concept of plasma-enhanced ALE of Al_2O_3 using BCl_3 radicals and Ar-plasma.

Plasma enhanced ALE is out of the scope of this work. However, I gave a short brief about it since it may give more understanding of ALE techniques as well as it can show the difference with thermal ALE that is the main concept to be demonstrated in this work.

1.2.2 Thermal ALE

In a typical thermal ALE, a modified surface is removed by chemical reactions that form volatile molecules [10,12,22-24]. The removal process is self-limiting because the surface chemical reactions are designed not to proceed further once the modified surface is completely removed. The major advantages of thermal ALE are that the process hardly leaves any damage to the surface and isotropic etching can be achieved because the surface reactions are typically non-directional. Its possible disadvantage is that it requires an elevated surface temperature to promote the surface reactions for desorption [6,9,10,21-27].

Thermal ALE of metal may be performed in the following manner; a top thin layer of the metal surface is either oxidized or halogenated first (the surface modification step) and then the oxidized/halogenated surface is exposed to organic molecules at an elevated surface temperature. In the following step, volatile organometallic complexes are formed and remove metal atoms from the oxidized/halogenated metal surface (removal step). The etching stops when the oxidized/halogenated layer is exhausted in the desorption step because such organic molecules typically do not react with pure metallic surfaces [8,9,25-28]. For instance of thermal ALE, I am going to explain what was done in Hamaguchi lab by my collage T. Ito [25] that can be considered as the experimental reference of this study beside H. L. Nigg and R. I. Masel experiment [22]. Ito's experiment is performed to etch a metallic Ni surface by an organic gas hexafluoroacetylacetone (hfacH). First, she deposited a mask of tantalum nitride (TaN) to cover areas that she wanted not to etch, as shown in Fig. 1.2 (a). Second, the Ni film was exposed to an oxygen gas to form a thin nickel oxide (NiO) layer as shown in Fig. 1.2 (b) , i.e.,

$$Ni + O \rightarrow NiO$$

This is known as the surface modification step. In the desorption step, the NiO surface was exposed to an hfacH gas to form loosely a monolayer of hfacH molecules to form nickel hexafluoroacetylacetonate $Ni(hfac)_2$ complexes and water molecules (H_2O) as shown in Fig. 1.2 (c). by increasing the surface temperature of 300 ~ 400 °C, $Ni(hfac)_2$ complexes and H_2O molecules were desorbed, i.e., desorption step is shown in Fig. 1.2 (d), from the surface through the reaction

$$NiO + 2\ hfacH \rightarrow Ni(hfac)_2 + H_2O$$

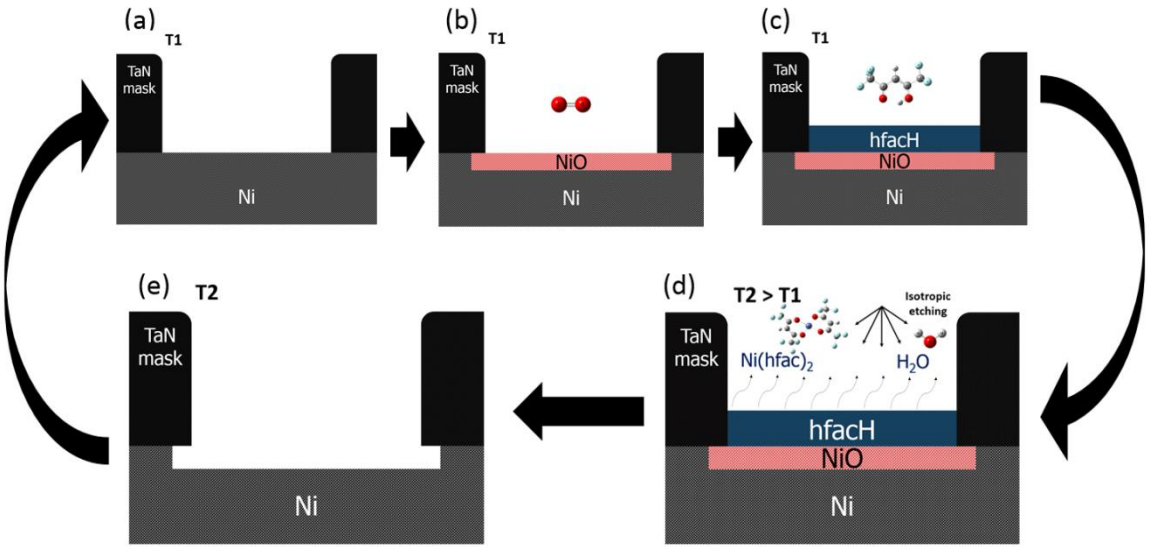


Fig. 1-2: Concept of thermal ALE for a Ni surface using O_2 and hfacH gases.

In this way, the oxidized layer formed on the Ni film was etched isotopically, as shown in Fig. 1.2 (e). There is no etching occurred once the NiO layer is removed, i.e., self-limiting and it will be explained next because formation and desorption of $Ni(hfac)_2$ do not take place on a metallic Ni surface. This is known as a full cycle that will be repeated to etch Ni substrate layer by layer using the thermal ALE technique.

Instead of using just thermal energy to form organometallic complexes, ligand exchange reactions among several organometallic complexes can also be used to perform thermal ALE [6]. Reaction mechanisms of such thermal ALE are out of the scope of this study.

When a Ni surface was exposed to an hfacH gas, hfacH molecules did not deprotonate, i.e., O-H bond in hfacH will be broken, and form $hfac^-$ whereby can form $Ni(hfac)_2$ complexes or H_2O molecules as it has been just explained. However, it will be adsorbed stably as enol hfacH molecules at very low temperatures, as shown in Fig. 1.3 (b). By increasing the surface temperature, adsorbed hfacH molecules were dissociated to

small fragments, as shown in Fig. 1.3 (c). As a result, no etching of Ni takes place without oxidizing the surface, which assures the self-liming of these processes.

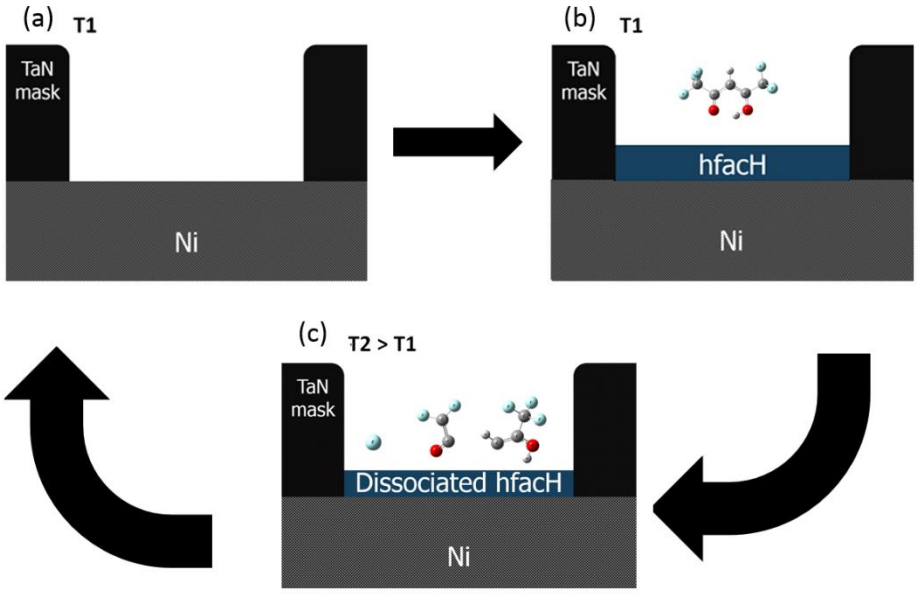


Fig. 1-3: Interaction between a Ni surface with hfacH molecules.

The mechanisms of Fig. 1.2 will be shown in chapter 3 and 4 as well as Fig 1.3 will be shown in chapter 3 and 5 using first-principles quantum mechanical (QM) calculations based on density functional theory (DFT).

The theoretical calculations have become a powerful tool to disclose the unknown physical and chemical properties as well as the chemical reaction mechanism of experiments. Furthermore, theoretical studies can sometimes provide efficient and meaningful predictions for future experiments. Therefore, several scientists awarded Nobel-Prize for developing methods or for understanding mechanisms of chemical reactions. In 2007, Gerhard Ertl was the last one for his work in fundamental molecular processes at the gas-solid interface.

Thermal ALE is still a new technique and a few papers have been published yet. Moreover, there is no a specific paper that has discussed the mechanisms of thermal ALE

processes for any metal before this work. Therefore, Prof. Satoshi Hamaguchi decided to investigate the mechanism of thermal ALE processes for a nickel (Ni) surface by organic molecules in his laboratory using first-principles quantum mechanical (QM) calculations as well as experimentally. In this thesis, I am discussing the simulation part of this project only since I have to give all my effort to proceed, run, and explain the calculations whereas Dr. Tomoko Ito was running the experiments with Prof. Kazuhiro Karahashi. The first-principles QM calculations and the experiments were running simultaneously and supervised by Prof. Satoshi Hamaguchi.

1.3 Motivation for this study and the literature

The motivation of this study comes from the interest of developing damageless etching technologies for magnetic metals such as Co, Fe, and Ni, which are typically used as materials for magnetic tunnel junctions (MTJs) in magneto-resistive random access memories (MRAMs). One of the major obstacles for the development of highly integrated MRAMs is the miniaturization of an MTJ, which consists of multiple thin layers of ferromagnetic metals and an insulating tunneling barrier layer [19]. As the dimensions of MTJ cells decrease, damages incurred by the ion impact of Ar ion milling or plasma etching in the manufacturing process of MTJ cells degrade their functionality, which prevents further miniaturization of MRAMs. Therefore, the use of a damageless thermal ALE using organic molecules is an attractive alternative for MTJ manufacturing processes.

Several organic molecules have been tested with Ni and other metals for thermal ALE processes experimentally [21, 22, 28]. For instance, Chen *et al.* [29,30] performed ALE of Fe, Cu, Co, Pd, Pt, and CoPt with a wet chemical etch by acetylacetone (acacH),

hfacH, ethylenediaminetetraacetic acid (edta), nitrilotriacetic acid (nta), pyridine-2,6-dicarboxylic acid (pdca), oxalic acid (oa), and formic acid (fa). Konh *et al.* studied thermal dry ALE of Co by chlorination and hfacH/acacH-based desorption [28]. Dry thermal ALE of Ni and Co by oxidation and hfacH/acacH-based desorption was also demonstrated by Ito *et al.* [25] as hfacH with Ni and NiO surfaces were illustrated in section 1.2.2.

1.4 Objectives of this study

The main objective of this study is to present qualitative insight into the mechanisms of the adsorption of hfacH molecules on an oxidized Ni surface, formation and desorption of nickel hexafluoroacetylacetonate $Ni(hfac)_2$ complexes and water H_2O molecules that can process thermal ALE of a NiO surface. The decomposition of hfacH molecules on a metallic Ni surface investigated to prove the self-limiting nature of thermal ALE for Ni with an hfacH gas that clarifies earlier experimental observations.

In this study focusing on thermal ALE of metallic Ni by oxidation and hfacH gas exposure, the surface reaction mechanisms of an oxidized Ni surface exposed to gaseous hfacH molecules was examined, using first-principles quantum mechanical (QM) calculations. First, simple monolayers models, i.e., to minimize the computational complexity, were used to discover the roadmap of this work. This research was started by evaluating the reaction energies of adsorption processes of hfacH on metallic Ni and NiO surfaces using GAUSSIAN 09 program, i.e., running QM calculations based on density functional theory (DFT), which will be reported in chapter 3. The stability of hfacH molecules adsorbed on Ni and NiO surfaces was examined in chapter 3. In chapter 4, the reported values in chapter 3 of reaction energies of hfacH adsorption on a NiO surface were

re-evaluated with more realistic multi-layer surface material models using an embedded cluster method (ECM) as implemented in TURBOMOLE, which is another QM program. In addition, the mechanisms of the formation of nickel hexafluoroacetylacetonate $Ni(hfac)_2$ complexes on a NiO surface and their desorption were investigated in chapter 4, too. After the adsorption and desorption mechanisms to processes thermal ALE of oxidized Ni layers by hfacH molecules were explained, the interaction between hfacH molecules with a metallic Ni surface was studied to prove the etching processes will be stopped automatically, i.e., called self-limiting, once NiO layers are removed and a metallic Ni surface appears which is the subject of chapter 5. However, if there is no self-limiting during the etching processes, this technique will not be ALE while it may be called chemical vapor etching (CVE) as the inverse of chemical vapor deposition (CVD). Therefore, what is found experimentally was demonstrated by first-principles QM calculations that when an hfacH molecule is an exposure to a pure metallic Ni surface, it is unlikely to be deprotonated and form $hfac^-$ whereby can form $Ni(hfac)_2$. On the other hand, it is more likely to be dissociated, stop the etching process, and the self-limiting condition is achieved. More specifically, the aim of chapter 5 is to clarify the mechanisms of hfacH decomposition on a metallic Ni surface. Moreover, a precise evaluation of the adsorption energies for a deprotonated and dissociated hfacH molecule on a periodic Ni surface has been discussed in chapter 5 using STATE code, i.e., in-house plane-wave pseudopotential code, to present a more realistic surface model.

1.5 Structure of this dissertation

This thesis is organized as follows:

The first chapter is giving a general introduction of ALE with a short brief of previous studies and the practical background of this work. The motivation and objectives of this study are introduced in this chapter, too.

The theoretical and computational background of the first-principles QM programs that are used in this study will be presented in chapter two: "Theoretical and Computational Fundamentals".

In chapter three, the stability of hexafluoroacetylacetone (hfacH) molecules on metallic and oxidized nickel surfaces in atomic layer etching (ALE) processes, i.e., a published paper [A. H. Basher, M. Krstić, T. Takeuchi, M. Isobe, T. Ito, M. Kiuchi, K. Karahashi, W. Wenzel, and S. Hamaguchi, "Stability of hexafluoroacetylacetone molecules on metallic and oxidized nickel surfaces in atomic layer etching (ALE) Processes," J. Vac. Sci. Technol. A 38, 022610 (2020)], will be shown.

Chapter four will present formation and desorption of nickel hexafluoroacetylacetonate $Ni(hfac)_2$ on a NiO surface in ALE processes, which is reporting an accepted paper to be published in JVST A [A. H. Basher, M. Krstić, F. Karin, T. Ito, K. Karahashi, W. Wenzel, and S. Hamaguchi, "Formation and desorption of nickel hexafluoroacetylacetonate $Ni(hfac)_2$ on a nickel oxide surface in atomic layer etching (ALE) processes," J. Vac. Sci. Technol. A, (*in press* 2020)].

In chapter five, mechanism of a self-limiting process in thermal atomic layer etching (ALE) of a Ni surface by hfacH that is the third paper accepted from this research [Abdulrahman H. Basher, Ikutaro Hamada, and Satoshi Hamaguchi, "Self-limiting

processes in thermal atomic layer etching of nickel by hexafluoroacetylacetone," Jpn. J. Appl. Phys., (*in press* 2020)] will be illustrated.

In the last chapter, summarize of this study is going to be given with the conclusion in chapter six.

1.6 References

[1] G. S. Oehrlein and S. Hamaguchi, Plasma Sources Sci. Technol. 27, 023001 (2018).

[2] K.J. Kanarik, S. Tan, and R.A. Gottscho, J. Phys. Chem. Lett. 9, 4814 (2018).

[3] W. Xie and G.N. Parsons, J. Vac. Sci. Technol. A 38, 022605 (2020).

[4] S. Rauf, T. Sparks, P.L.G. Ventzek, V. V. Smirnov, A. V. Stengach, K.G. Gaynullin, and V.A. Pavlovsky, J. Appl. Phys. 101, 033308 (2007).

[5] A. Agarwal and M. J. Kushner, J. Vac. Sci. Technol., A 27, 37 (2009).

[6] S.M. George, Chem. Rev. 110, 111 (2010).

[7] D. Metzler, R.L. Bruce, S. Engelmann, E.A. Joseph, and G.S. Oehrlein, J. Vac. Sci. Technol., A 32, 020603 (2014).

[8] G. Yuan, N. Wang, S. Huang, and J. Liu, "A brief overview of atomic layer deposition and etching in the semiconductor processing," in 2016 17th Int. Conf. Electron. Packag. Technol. (ICEPT, Wuhan, China, 2016), 1365 (2016).

[9] K. J. Kanarik, T. Lill, E. A. Hudson, S. Sriraman, S. Tan, J. Marks, V. Vahedi, and R. A. Gottscho, J. Vac. Sci. Technol. A 33, 020802 (2015).

[10] P.C. Lemaire and G.N. Parsons, Chem. Mater. 29, 6653 (2017).

[11] 10 K. J. Kanarik, S. Tan, and R. A. Gottscho, J. Phys. Chem. Lett. 9, 4814 (2018).

[12] A. Fischer, A. Routzahn, Y. Lee, T. Lill, and S.M. George, J. Vac. Sci. Technol. A 38, 022603 (2020).

[13] M. N. Yoder, U.S. Pat. 4756794 (1988).

[14] Y. Horiike, T. Tanaka, M. Nakano, S. Iseda, H. Sakaue, A. Nagata, H. Shindo, S. Miyazaki, and M. Hirose, J. Vac. Sci. Technol. A 8, 1844 (1990).

[15] P. Walker and W.H. Tarn, *Handbook of Metal Etchants*, CRC Press, (1991).

[16] Y. Aoyagi, K. Shinmura, K. Kawasaki, T. Tanaka, K. Gamo, S. Namba, and I. Nakamoto, Appl. Phys. Lett. 60, 968 (1992).

[17] T. Matsuura, J. Murota, Y. Sawada, and T. Ohmi, Appl. Phys. Lett. 63, 2803 (1993).

[18] M. A. George, D. W. Hess, S. E. Beck, K. Young, D. A. Bohling, G. Voloshin, and A. P. Lane, J. Electrochem. Soc. 143, 3257 (1996).

[19] W. Boullart, D. Radisic, V. Paraschiv, S. Cornelissen, M. Manfrini, K. Yatsuda, E. Nishimura, T. Ohishi, and S.Tahara, Proc. of SPIE Advanced Lithography (San Jose, USA, 2013) SPIE 8685, 86850F (2013).

[20] K.S. Min, S.H. Kang, J.K. Kim, Y.I. Jhon, M.S. Jhon, G.Y. Yeom,Microelectronic Eng. 110, 457 (2013).

[21] C. T. Carver, J. J. Plombon, P. E. Romero, S. Suri, T. A. Tronic, and R. B. Turkot, ECS J. Solid State Sci. Technol. 4, N5005 (2015).

[22] H. L. Nigg and R. I. Masel, J. Vac. Sci. Technol. A 17, 3477 (1999).

[23] S. M. George and Y. Lee, ACS Nano 10, 4889 (2016).

[24] Y. Lee and S.M. George, J. Phys. Chem. C 123, 18455 (2019).

[25] T. Ito, K. Karahashi, and S. Hamaguchi, in Proceedings of the 39th International Symposium on Dry Process, Tokyo, Japan, 16–17 November 2017, edited by K. Kinoshita et al. (DPS Organizing Committee, 2017), Vol. E-4, p. 45.

[26] J. Zhao, M. Konh, and A. V. Teplyakov, Appl. Surf. Sci. 455, 438 (2018).

[27] A.I. Abdulagatov and S.M. George, J. Vac. Sci. Technol. A 38, 022607 (2020).

[28] M. Konh, C. He, X. Lin, X. Guo, V. Pallem, R. Opila, A. Teplyakov, Z. Wang, and B. Yuan, Vac. Sci. Technol. A 37, 021004 (2019).

[29] J. K. Chen, T. Kim, N. D. Altieri, E. Chen, and J. P. Chang, J. Vac. Sci. Technol. A 35, 031304 (2017).

[30] J. K. Chen, N. D. Altieri, T. Kim, E. Chen, T. Lill, M. Shen, and J. P. Chang, J. Vac. Sci. Technol. A 35, 05C305 (2017).

CHAPTER 2:

Theoretical and Computational Fundamentals

2.1 Introduction

The first-principles calculation based on density functional theory (DFT) has been widely used to investigate the geometric and electronic structure, dynamics, and chemical reactions of molecules and condensed matter systems. Walter Kohn was awarded the Nobel Prize of chemistry "for developing density-functional theory (DFT)," sharing with John A. Pople "for his efforts in computational and quantum chemistry" in 1998.

In this chapter, I shall concentrate on the theoretical background of the first principle calculations codes that are used in my study starting from the Schrödinger equation for many-particle systems. Then, I will present several approximations that are used to let such a complicated equation solved.

2.2 Many-particle Schrödinger equation

The total energy of the system E can be obtained by solving the following Schrödinger equation

$$\widehat{H}_{\text{tot}}\Psi(\{\boldsymbol{r_i}\},\{\boldsymbol{R}_I\}) = E\Psi(\{\boldsymbol{r}_i\},\{\boldsymbol{R}_I\}) \tag{2.1}$$

or equivalently by calculating the expectation value

$$E = \frac{\langle\Psi|\widehat{H}_{\text{tot}}|\Psi\rangle}{\langle\Psi|\Psi\rangle}, \tag{2.2}$$

where $\Psi(\{\boldsymbol{x}_i\},\{\boldsymbol{R}_I\}) = \Psi(\boldsymbol{x}_1,\boldsymbol{x}_2,\cdots,\boldsymbol{R}_1,\boldsymbol{R}_2,\cdots)$ is the many-particle wave function as a function of the electron coordinates $\{\boldsymbol{r}_i\}$, which is composed of the spatial coordinates $\{\boldsymbol{r_i}\}$ and spin coordinate $\{\sigma_i\}$, and nuclear coordinate $\{\boldsymbol{R}_I\}$. The Hamiltonian of the total system is given by

$$\widehat{H}_{\text{tot}} = -\sum_i \frac{\hbar^2}{2m_e}\nabla_i^2 + \frac{1}{2}\sum_{ij\ (i\neq j)}\frac{e^2}{|r_i-r_j|} - \sum_I\sum_i\frac{Z_I^2e^2}{|r_i-R_I|} - \sum_I\frac{\hbar^2}{2M_I}\nabla_I^2 + \frac{1}{2}\sum_{IJ\ (I\neq J)}\frac{Z_IZ_Je^2}{|R_I-R_J|}, \tag{2.3}$$

where m_e is the mass of the electron, e is the elementary charge, Z_I and M_I are the charge and mass of the ion I, respectively.

In order to solve the many-particle Schrödinger equation, many approximations have to be introduced. Since the nuclei are much heavier than the electrons, the electron movement is much faster than that of nuclei. Therefore, the nuclear position can be assumed as fixed during the electron motion. The separation of the electronic and nuclear motions is called the Born-Oppenheimer (BO)/adiabatic approximation. Assuming that $m_e \gg M_I$, the fourth term in the total Hamiltonian can be neglected to obtain

$$\hat{H}_{\text{tot}} = \hat{T} + \hat{V}_{ee} + \hat{V}_{Ne} + \hat{V}_{NN}, \qquad (2.4)$$

where the kinetic energy operator for the electrons is given by

$$\hat{T} = -\sum_i \frac{\hbar^2}{2m_e} \nabla_i^2, \qquad (2.5)$$

the electron-electron interaction is given by

$$\hat{V}_{ee} = \frac{1}{2} \sum_{ij\ (i \neq j)} \frac{e^2}{|r_i - r_j|}, \qquad (2.6)$$

the electron-nuclei interaction is given by

$$\hat{V}_{Ne} = -\sum_I \sum_i \frac{Z_I^2 e^2}{|r_i - R_I|}, \qquad (2.7)$$

and the interaction between nuclei is given by

$$\hat{V}_{NN} = \frac{1}{2} \sum_{IJ\ (I \neq J)} \frac{Z_I Z_J e^2}{|R_I - R_J|}. \qquad (2.8)$$

The nuclei are often considered as point charges and treated classically, and $\hat{V}_{NN}$is regarded as a constant term when the electronic part of the Schrödinger equation is concerned. The electronic part of the Schrödinger equation is then given by

$$\hat{H}_{\text{el}} = \hat{T} + \hat{V}_{ee} + \hat{V}_{Ne} \qquad (2.9)$$

This separation of electronic and nuclear degrees of freedom allows one to treat a wave function as a function of electronic coordinate $\{\boldsymbol{r}_i\}$ at given nuclear coordinates $\{\boldsymbol{R}_I\}$, and the task is reduced to solve the Schrödinger equation for the (many-)electron system

$$\widehat{H}_{\mathrm{el}}\Psi(\{\boldsymbol{r}_i\}) = E\Psi(\{\boldsymbol{r}_i\}). \tag{2.10}$$

For simplicity, nuclear coordinates are omitted. Despite this simplification, one still needs to solve many particle system, and further approximation has to be made.

2.3 Hartree-Fock approximation

In the Hartree-Fock approximation,

$$\Psi = \frac{1}{\sqrt{N!}} \begin{vmatrix} \phi_1^{\sigma 1}(\boldsymbol{r}_1)\ \phi_2^{\sigma 1}(\boldsymbol{r}_1) \ldots. & \phi_N^{\sigma 1}(\boldsymbol{r}_1) \\ \phi_1^{\sigma 2}(\boldsymbol{r}_2)\ \phi_2^{\sigma 2}(\boldsymbol{r}_2) \ldots. & \phi_N^{\sigma 2}(\boldsymbol{r}_2) \\ \vdots & \vdots \\ \phi_1^{\sigma_N}(\boldsymbol{r}_N)\ \phi_2^{\sigma_N}(\boldsymbol{r}_N) \ldots. & \phi_N^{\sigma N}(\boldsymbol{r}_N) \end{vmatrix}, \tag{2.11}$$

where $\{\phi_i^{\sigma_i}(r_i)\}$ are one electron spin orbital defined by $\phi_i^{\sigma_i}(r_i) = \psi_i^{\sigma_i}(r_i) \times \alpha_i(\sigma_i)$ with $\psi_i^{\sigma_i}(r_i)$ and $\alpha_i(\sigma_i)$ being the spatial orbital and spin function, respectively, and this satisfies the Pauli exclusion principle the Fermions have to obey.

Now, the total energy of an *N*-electron system can be rewritten by using the Slater determinant as

$$E = \sum_{i,\sigma} h_i^{\sigma} + \frac{1}{2}\sum_{i,j}\sum_{\sigma_i,\sigma_j}\left(J_{ij}^{\sigma_i,\sigma_j} - K_{ij}^{\sigma_i}\delta_{\sigma_i\sigma_j}\right) + E_{nn}, \tag{2.12}$$

where

$$h_i^{\sigma} = \langle \psi_i^{\sigma} \left| -\frac{1}{2}\nabla^2 + \hat{V}_{ext} \right| \psi_i^{\sigma} \rangle\,, \tag{2.13}$$

$$J_{ij}^{\sigma_i,\sigma_j} = \iint d\boldsymbol{r}d\boldsymbol{r}'\ \psi_i^{\sigma_i}(\boldsymbol{r})\psi_j^{\sigma_j}(\boldsymbol{r}')\frac{1}{|\boldsymbol{r}-\boldsymbol{r}'|}\psi_i^{\sigma_i}(\boldsymbol{r})\psi_j^{\sigma_j}(\boldsymbol{r}')\,, \tag{2.14}$$

$$K_{ij}^{\sigma} = \iint d\boldsymbol{r}d\boldsymbol{r}'\ \psi_i^{\sigma}(\boldsymbol{r})\psi_j^{\sigma}(\boldsymbol{r}')\frac{1}{|\boldsymbol{r}-\boldsymbol{r}'|}\psi_j^{\sigma}(\boldsymbol{r})\psi_i^{\sigma}(\boldsymbol{r}'), \tag{2.15}$$

with

$$V_{ext}(r_i) = \sum_I \frac{Z_I e^2}{|r_i - R_I|}, \tag{2.16}$$

and the last term is the classical inter-nuclear interaction. The total energy is variational with respect to the spin-orbitals and the ground-state total energy and spin-orbitals are obtained by minimizing the total energy E with respect to the spin-orbitals subject to the orthonormal condition for the spin-orbital

$$\int dr\, \psi_i^{\sigma_i *}(r)\psi_j^{\sigma_j}(r) = \delta_{ij}\delta_{\sigma_i\sigma_j}. \tag{2.17}$$

This is achieved via the Lagrange method as follows. We define the constrained total energy

$$E' = E - \sum_{i,j,\sigma} \Lambda_{ij}^{\sigma}\left(\int dr\, \psi_i^{\sigma *}(r)\psi_j^{\sigma}(r) - \delta_{ij}\right), \tag{2.18}$$

where Λ_{ij} is the Lagrange multiplier, and from the stationary condition

$$\frac{\delta E'}{\delta \psi_i^{\sigma *}(r)} = 0\ . \tag{2.19}$$

The following Euler-Lagrange equation is obtained.

$$\widehat{H}_{\mathrm{HF}}\psi_i^{\sigma}(r) = \sum_j \Lambda_{ij}^{\sigma}\psi_j^{\sigma}(r)\ , \tag{2.20}$$

where

$$\widehat{H}_{\mathrm{HF}} = -\frac{\hbar^2}{2m_e}\nabla^2 + \hat{V}_{ext} + \hat{J} - \hat{K}. \tag{2.21}$$

Here, the external potential is defined by

$$V_{\mathrm{ext}}(r) = \sum_I \frac{Z_I e^2}{|r - R_I|}, \tag{2.22}$$

and the Coulomb operator $\hat{J}$ and the exchange operator $\hat{K}$ are defined as

$$\hat{J}\psi_i^{\sigma}(r) = \sum_{j,\sigma'} \int dr' \psi_j^{\sigma'}(r')\psi_j^{\sigma'}(r')\frac{1}{|r - r'|}\psi_i^{\sigma}(r)\ , \tag{2.23}$$

and

$$\hat{K}\psi_i^\sigma(r) = \sum_j \int dr' \psi_j^\sigma(r')\psi_i^\sigma(r') \frac{1}{|r-r'|}\psi_j^\sigma(r)\,. \qquad (2.24)$$

Because $\hat{H}_{\mathrm{HF}}$ is a Hermitian operator, the Hamiltonian and the total energy of the system are unchanged under a certain unitary transformation. By applying a unitary transformation which diagonalizes the Lagrange multiplier, one arrives at the canonical Hartree-Fock equation

$$\hat{H}_{\mathrm{HF}}\tilde{\psi}_i^\sigma(r) = \varepsilon_i\tilde{\psi}_i^\sigma(r), \qquad (2.25)$$

where

$$\varepsilon_i\delta_{ij} = \sum_k U_{ik}\Lambda_{kl}U_{lj}^\dagger, \qquad (2.26)$$

and

$$\tilde{\psi}_i^\sigma(r) = \sum_j U_{ij}\psi_j^\sigma(r). \qquad (2.27)$$

In these equations, each electron moves independently with each other in the mean-field of other nuclei and electrons. The complex many-particle problem is simplified as a set of one-electron problems. This is another approximation that will be used and it is called "one-electron approximation."

The above framework is called the Hartree-Fock (HF) approximation or method, which is also called the self-consistent field (SCF) method. It has been widely applied to not only atom or molecule but also condensed matter. In the HF approximation, the electron-electron correlation, except for those in the same spin is not taken into account. Several methods have been developed to account for the electron-correlation missing in the HF approximation, such as configuration interaction, many-body perturbation theories. Such "beyond HF" methods are proven accurate in describing molecular as well as periodic systems, but are computationally very expensive and limited to relatively simple systems.

Thus, in order to study complex systems, such as surfaces and interfaces, more practical methods are required.

2.4 Density functional theory (DFT)

The Hamiltonian of the interacting electros in an external potential $V_{\text{ext}}(r)$ can be written as

$$\hat{H} = -\frac{\hbar^2}{2m_e}\sum_i \nabla_i^2 + \sum_i V_{\text{ext}}(r_i) + \frac{1}{2}\sum_{i,j\ (i\neq j)} \frac{e^2}{|r_i - r_j|}, \qquad (2.28)$$

where the ion-ion interaction is omitted for simplicity and $V_{ext}(r)$ is not necessarily the potential from the nuclei. The total energy of the electron system is given by

$$E = \langle \Psi | \hat{T} + \hat{V}_{\text{ext}} + \hat{V}_{ee} | \Psi \rangle. \qquad (2.29)$$

This can be rewritten by using the one electron density as

$$E = \left\langle \Psi \middle| \hat{T} + \hat{V}_{ee} \middle| \Psi \right\rangle + \int dr\, V(r) n(r), \qquad (2.30)$$

where

$$n(\boldsymbol{r}) = \int \cdots \int d\sigma_1 d\boldsymbol{x}_2\, d\boldsymbol{x}_3 \cdots dx_N \Psi^*(\boldsymbol{r}\sigma_1, \boldsymbol{x}_2, \cdots \boldsymbol{x}_N)\Psi(\boldsymbol{r}\sigma_1, \boldsymbol{x}_2, \cdots \boldsymbol{x}_N)\,. \qquad (2.31)$$

The original density functional of the non-interacting homogeneous electron system was proposed by Thomas [1] and Fermi [2], which was later extended by Dirac [3,4], which is given by

$$E[n] = C_1 \int d\boldsymbol{r} n^{\frac{5}{3}}(\boldsymbol{r}) + \int d\boldsymbol{r}\, V_{\text{ext}}(\boldsymbol{r}) n(\boldsymbol{r}) + C_2 \int d\boldsymbol{r} n^{\frac{4}{3}}(\boldsymbol{r}) + \frac{1}{2}\int d\boldsymbol{r} \frac{d\boldsymbol{r}' n(\boldsymbol{r}) n(\boldsymbol{r}')}{|\boldsymbol{r} - \boldsymbol{r}'|}, \qquad (2.32)$$

with $C_1 = \frac{3}{10}(3\pi^2)^{\frac{2}{3}}$ and $C_2 = -\frac{3}{4}\left(\frac{3}{\pi}\right)^{\frac{1}{3}}$. The first and third terms are the approximate kinetic and exchange energies, respectively.

2.4.1 Hohenberg-Kohn theorem

The formulation by Hohenberg and Kohn is exact for many-particle systems, and basis of modern DFT [5]. The Hohenberg-Kohn theorem states that:

- For any system of interacting particles in an external potential $V_{\text{ext}}(r)$, the potential $V_{\text{ext}}(r)$ is determined uniquely by the ground state density $n(r)$, except for a constant
- A universal functional $E[n]$ is uniquely determined for any potential $V_{\text{ext}}(r)$, and the density that minimizes the functional is the exact ground state density $n(r)$.

The first theorem indicates that the Hamiltonian is fully determined except for the constant and therefore the wave functions of the many-particle states are determined. This also means that all the property of the system is determined.

2.4.2 Kohn-Sham density functional theory

Kohn and Sham [6] introduced a set of one-electron orbitals to obtain a practical, yet exact form of the total energy (Eq. 2.32), by introducing an auxiliary non-interaction many-electron system that has the same electron density as the real system. The electron density of a non-interacting many-electron system can be written exactly in terms of one-electron orbitals as

$$n(\boldsymbol{r}) = \sum_{\sigma}\sum_{i}|\psi_i^{\sigma}(\boldsymbol{r})|^2 \,, \tag{2.33}$$

and the kinetic energy of a non-interacting system can be written as

$$T_s[n] = -\frac{\hbar^2}{2m_e}\sum_{\sigma}\sum_{i}\langle\psi_i^{\sigma}|\nabla^2|\psi_i^{\sigma}\rangle. \tag{2.34}$$

The classical electrostatic interaction between electrons can be given by

$$E_H[n] = \frac{1}{2}\iint d\boldsymbol{r}\, d\boldsymbol{r}' \frac{n(\boldsymbol{r})n(\boldsymbol{r}')}{|\boldsymbol{r}-\boldsymbol{r}'|}\,. \tag{2.35}$$

Then, the total energy of the (electron) system can be written as

$$E[n] = \langle\Psi|\hat{T} + \hat{V}_{ee}|\Psi\rangle + \int d\boldsymbol{r}\, V_{ext}(\boldsymbol{r})n(\boldsymbol{r}) \tag{2.36}$$

$$E[n] = T[n] + \int d\boldsymbol{r}\, V_{ext}(\boldsymbol{r})n(\boldsymbol{r}) + \langle\Psi|\hat{V}_{ee}|\Psi\rangle \tag{2.37}$$

$$E[n] = T_s[n] + \int d\boldsymbol{r}\, V_{\text{ext}}(\boldsymbol{r})n(\boldsymbol{r}) + E_H[n] + E_{xc}[n]\,, \tag{2.38}$$

where the exchange-correlation functional is defined by

$$E_{xc}[n] = T[n] - T_s[n] + \langle\Psi|\hat{V}_{ee}|\Psi\rangle - E_H[n], \tag{2.39}$$

which contains the differences between kinetic and interaction energies of the true interacting and non-interacting systems. The Kohn-Sham total energy functional is variational with respect to the one-electron (Kohn-Sham) orbitals under the orthonormal condition

$$\left\langle \psi_i^{\sigma_i} \middle| \psi_j^{\sigma_j} \right\rangle = \delta_{ij}\delta_{\sigma_i\sigma_j} \tag{2.40}$$

This is achieved by introducing the Lagrange multiplier $\Lambda_i j^{\sigma}$ as

$$E'[n] = E[n] - \sum_\sigma \sum_{ij} \Lambda_{ij}^{\sigma}\left(\langle\psi_i^{\sigma}|\psi_j^{\sigma}\rangle - \delta_{ij}\right). \tag{2.41}$$

The stationary condition

$$\frac{\delta E[n]}{\delta\langle\psi_i^{\sigma}|} = 0 \tag{2.42}$$

leads to the following Euler-Lagrange equation

$$\hat{H}_{KS}|\psi_i^{\sigma}\rangle = \sum_j \Lambda_{ij}^{\sigma}|\psi_j\rangle\,, \tag{2.43}$$

where the Kohn-Sham Hamiltonian is defined by

$$H_{KS}(\boldsymbol{r}) = -\frac{\hbar^2}{2m_e}\nabla^2 + V_{ext}(\boldsymbol{r}) + V_H(\boldsymbol{r}) + V_{xc}(\boldsymbol{r}) \tag{2.44}$$

with the Hartree potential

$$V_H(\boldsymbol{r}) = \int d\boldsymbol{r}' \frac{n(\boldsymbol{r}')}{|\boldsymbol{r}-\boldsymbol{r}'|} \qquad (2.45)$$

and the exchange-correlation potential

$$V_{xc}(\boldsymbol{r}) = \frac{\delta E_{xc}}{\delta n(\boldsymbol{r})}. \qquad (2.46)$$

Because the Kohn-Sham Hamiltonian is a Hermitian operator and invariant under the unitary transformation. By introducing the unitary transformation that diagonalizes the Lagrange multiplier, we arrive at the following Kohn-Sham equation

$$\hat{H}_{KS}\left|\tilde{\psi}_i^\sigma\right\rangle = \varepsilon_i^\sigma \left|\tilde{\psi}_i^\sigma\right\rangle, \qquad (2.47)$$

where the canonical Kohn-Sham orbital is given by

$$\tilde{\psi}_i^\sigma(\boldsymbol{r}) = \sum_j U_{ij}\psi_j^\sigma(\boldsymbol{r}) \qquad (2.48)$$

and

$$\varepsilon_i\delta_{ij} = \sum_k U_{ik}\Lambda_{kl}U_{lj}^\dagger. \qquad (2.49)$$

The problem of the *N*-electron system is now recast into a set of *N* one-electron problems. The Kohn-Sham equation is a nonlinear differential equation and has to be solved self-consistently. In principle, the solution of these equations leads to the exact ground state energy, if the exact exchange-correlation functional were known. In practice, we need to introduce a tractable approximation to the exchange-correlation functional, which is discussed below. Note also that the Kohn-Sham energies (ε_i^σ) is introduced as Lagrange multiplier to enforce the orthonormal condition of the one-particle orbitals and in principle have not physical significance, although the Kohn-Sham energies are often used to interpret the experimental data (and often found to be useful).

2.4.3 Exchange-correlation functionals

a. The local density approximation (LDA) and the generalized gradient approximation (GGA)

The main difficulty in DFT is that the exact exchange-correlation functional is unknown. Therefore, it can be considered that the development of efficient exchange-correlation functionals is the key to the success of DFT.

Solid-state systems can be considered to be close to the homogeneous electron gas, where the exchange and correlation effect is local, which leads to local density approximation (LDA)/local spin density approximation (LSDA). In LSDA the exchange-correlation functional is given by

$$E_{xc}[n_\uparrow, n_\downarrow] = \int d\boldsymbol{r}\, \epsilon_{xc}^{unif}(n_\uparrow, n_\downarrow) n(\boldsymbol{r}) = \int d\boldsymbol{r}\, [\epsilon_x^{unif}(n_\uparrow, n_\downarrow) + \epsilon_c^{unif}(n_\uparrow, n_\downarrow)] n(\boldsymbol{r}), \quad (2.50)$$

where n_σ ($\sigma = \uparrow, \downarrow$) is the spin density with $n = n_\uparrow + n_\downarrow$, and $\epsilon_{xc}^{unif}(n_\uparrow, n_\downarrow)$ is the exchange-correlation energy per electron for the homogeneous electron gas. ϵ_x^{unif} can be calculated analytically. For the correlation energy, there is an accurate result by using the quantum Monte Carlo method by Ceperley and Alder [7] and several functional [8-10] forms for ϵ_c^{unif} exist to reproduce the Monte Carlo results. The correlation energy is often described in terms of the Seitz radius $r_s = \left(\frac{3}{4\pi n}\right)^{\frac{1}{3}}$ and the polarization $\zeta = \frac{n_\uparrow - n_\downarrow}{n}$. The LDA/LSDA has proven accurate and useful to understand and predict the physical properties of diverse solid systems.

A step to improve the accuracy of LDA/LSDA is to introduce the magnitude of the gradient of the density $|\nabla n_\sigma|$, which is called the generalized gradient approximation (GGA).

A general form of the exchange-correlation within GGA is given by

$$E_{xc}^{GGA}[n_\uparrow, n_\downarrow] = \int d\boldsymbol{r}\, f(n_\uparrow, n_\downarrow, |\nabla n_\uparrow|, |\nabla n_\downarrow|), \qquad (2.51)$$

which can be divided into the exchange and correlation part ($E_{xc}^{GGA} = E_x^{GGA} + E_c^{GGA}$). The exchange energy functional can be written by using the scaling relationship as

$$E_x[n_\uparrow, n_\downarrow] = \frac{1}{2}\{E_x[2n_\uparrow], E_x[2n_\downarrow]\}\,, \qquad (2.52)$$

where $E_x[n]$ is the exchange energy given by

$$E_x^{GGA}[n] = \int dr\, F_x(s) n(r) \qquad (2.53)$$

with the exchange enhancement factor F_x as a function of the reduced density gradient $s = |\nabla n|/2k_F n$ and $k_F = (3\pi^2 n)^{1/3}$. The correlation energy functional is given by

$$E_c[n_\uparrow, n_\downarrow] = \int d\boldsymbol{r}\, n\left[\, \epsilon_c^{unif}(r_s, \zeta) + H(t, r_s, \zeta)\right], \qquad (2.54)$$

where $t = |\nabla n|/2\phi k_s n$ is a dimensionless density gradient and $\phi = \phi(\zeta) = \frac{\left[(1+\zeta)^{\frac{2}{3}} + (1-\zeta)^{\frac{2}{3}}\right]}{2}$ is a spin-scaling factor. The popular GGA functional is the one by Perdew and Wang (PW91) [11], which was simplified by Perdew, Burke, and Ernzerhof (PBE) [12]. The PBE functional has been mostly used in the condensed matter field. Several variants of the PBE functional exist, including revPBE by Zhang and Yang [13], RPBE by Hammer et al. [14], PBEsol [15], and WC of Wu and Cohen [16]. The RPBE functional has been widely used in the DFT study of heterogeneous catalysis, and PBEsol and WC are shown to be superior for solids and surfaces.

b. Hybrid exchange-correlation functionals

Hybrid functionals are a more accurate class of approximations to the exchange-correlation functionals in DFT that incorporate a portion of exact exchange [17]. Hybrid

functionals are progressively approaching the desired accuracy in many molecular properties, but they are computationally much more expensive than GGA functionals. Among others, PBE0 [17,18] and B3LYP functionals [19] are the most widely used ones in materials science and molecular science fields, and the ones used in this work. The PBE0 functional is given by

$$E_{\mathrm{xc}}^{\mathrm{PBE0}} = E_{\mathrm{XC}}^{\mathrm{PBE}} + 0.25\left(E_{\mathrm{X}}^{\mathrm{HF}} - E_{\mathrm{X}}^{\mathrm{PBE}}\right), \qquad (2.55)$$

where $E_{\mathrm{XC}}^{\mathrm{PBE}}$ is the PBE exchange-correlation, $E_{\mathrm{X}}^{\mathrm{PBE}}$ is the GGA exchange, and $E_{\mathrm{X}}^{\mathrm{HF}}$ is the HF exchange. The B3LYP functional is defined by

$$E_{\mathrm{XC}}^{\mathrm{B3LYP}} = E_{\mathrm{X}}^{\mathrm{LDA}} + 0.20\left(E_{\mathrm{X}}^{\mathrm{HF}} - E_{\mathrm{X}}^{\mathrm{LDA}}\right) + 0.72\left(E_{\mathrm{X}}^{\mathrm{B88}} - E_{\mathrm{X}}^{\mathrm{LDA}}\right) + E_{\mathrm{C}}^{\mathrm{VWN}} + 0.81\left(E_{\mathrm{C}}^{\mathrm{LYP}} - E_{\mathrm{C}}^{\mathrm{VWN}}\right), \qquad (2.56)$$

where $E_{\mathrm{X}}^{\mathrm{B88}}$ is the Becke exchange [20], $E_{\mathrm{X}}^{\mathrm{LDA}}$ is the LDA exchange, $E_{\mathrm{C}}^{\mathrm{LYP}}$ is the GGA correlation functional of Lee, Yang, and Parr [21], and $E_{\mathrm{C}}^{\mathrm{VWN}}$ is the Vosko-Wilk-Nusair LDA correlation functional [22].

It is important to mention that the B3LYP functional is not appropriate for periodic systems since the correlation energy part is incorrect in the homogeneous electron gas limit [23]. Although much progress has been made in the methodological and algorithmic development of the hybrid functional especially for solids, the computational cost is still much higher compared with GGA. An alternative way to mitigate the shortcoming of GGA, such as small band gaps for semiconductors and insulators, is to introduce the correction of the on-site Coulomb interaction, known as DFT plus Hubbard *U* correction (DFT+*U*) [24,25]. The DFT+*U* approach has been successfully applied to the strongly correlated electron system such as NiO. It is worth mentioning that Verma and Truhlar [26] found that a hybrid functional always improves results for band gaps compared to a local

functional, while the addition of the Hubbard correction to a local functional does not always improve results. In addition, they found that the Hubbard correction showed improvement in the bandgap when applied to the valence *d* orbitals of metal, while the improvement is not necessarily significant when applied to the *s* and *p* orbitals. For nickel oxide (NiO), the bandgap is improved by using a Hubbard correction, and the improvement is comparable to B3LYP [27].

2.5 Dispersion correction

The dispersion forces, also known as the London (dispersion) forces, are a type of (attractive) interaction acting on atoms and molecules. The charge density of atoms and molecules fluctuates in time, which induces the instantaneous charge density fluctuation, giving rise to the instantaneous dipole-induced dipole interaction, whose leading term is $-1/R^6$, where R is the distance between atoms or molecules. Standard LDA/GGA exchange-correlation functionals are not able to describe the dispersion forces properly, because these functionals are static and local by construction, and nonlocal, and cannot capture the dynamic and nonlocal nature of the dispersion forces. A practical way to correct for the missing dispersion forces is to add a term containing the leading $-1/R^6$ term[28-30]. The numerous progress has been made in this direction. Another DFT-based approach is the nonlocal van der Waals density functional (vdW-DF)[31-34], which introduces a nonlocal correlation functional and able to describe the dispersion interaction within DFT. We refer some recent reviews [35,36] for interested readers. In the following, the dispersion correction proposed by Grimme (DFT-D2/DFT-D3) [37-39] and the vdW-DF are briefly outlined.

2.5.1 Dispersion correction by Grimme (DFT-D2/DFT-D3)

A general form of the dispersion corrected DFT total energy is given by

$$E_{\text{tot}} = E_{\text{DFT}} + E_{\text{disp}}, \qquad (2.57)$$

Where E_{DFT} is the total energy within LDA/GGA or that with the hybrid exchange-correlation functional and E_{disp} is the dispersion correction, which can be computed at a different level of approximation. Grimme proposed the following form of the dispersion correction [37]:

$$E_{\text{disp}} = -\frac{1}{2} s_6 \sum_{A \neq B} f_{\text{dmp}}(R_{AB}) \frac{C_6^{AB}}{R_{AB}^6}, \qquad (2.58)$$

where A and B denote atoms in the system, R_{AB} is the distance between atoms A and B, C_6^{AB} is the so-called dispersion coefficient (or C_6 coefficient), which depends on the pairs A and B, and s_6 is a parameter, which depends on the local/semi-local functional used. f_{dmp} is the damping function introduced to avoid the R_{AB}^6 singularity, given by

$$f_{\text{dmp}}(R_{AB}) = \frac{1}{1+e^{-d\left(\frac{R_{AB}}{R_r}-1\right)}}, \qquad (2.59)$$

where R_r is the sum of the vdW radii of atom I and J, and d is a damping parameter. There is no unique expression for the damping function and indeed, several functional forms have been proposed. In principle the dispersion coefficient C_6^{AB} depends on (A, B) and can be calculated by using the Casimir and Polder formulation

$$C_6^{AB} = \frac{3}{\pi} \int_0^{\infty} d\omega \alpha_A(i\omega) \alpha_B(i\omega), \qquad (2.60)$$

where $\alpha_{A(B)}$ is the polarizability of atom A (B), but in practice, it is calculated as

$$C_6^{AB} = \sqrt{C_6^A C_6^B}, \qquad (2.61)$$

where $C_6^{A(B)}$'s are calculated from the atomic ionization potential and polarizability with the PBE0 functional as tabulated in Ref. [37]. In DFT-D2, there are arbitrary choices of

dispersion coefficients for some elements, e.g., alkali and alkali earth atoms, for which average of the previous noble gas and group III atoms is used. Also the s_6 coefficient has to be determined depending on which local/semilocal (or dispersionless) DFT functional is used, and how to determine the value is arbitrary.

DFT-D3 is the newer version of dispersion corrected DFT by Grimme and co-workers, and considered to be more accurate [38]. It is less empirical than its predecessors, covers the first 94 elements in the periodic table, and the dispersion coefficients and vdW/cutoff radii are computed on the fly and system dependent. The pairwise part of the original DFT-D3 dispersion correction is given by

$$E_{\mathrm{disp}} = -\frac{1}{2}\sum_{A\neq B}\sum_{n=6,8} s_n f_{\mathrm{dmp}}^{n}(R_{AB})\frac{C_n^{AB}}{R_{AB}^{n}}, \qquad (2.62)$$

where the damping function f_{dmp}^{n} was originally proposed for the dispersion corrected ω-B97X functional by Chai and Head-Godon [40], given by

$$f_{\mathrm{dmp}}^{6}(R_{AB}) = \frac{1}{1+6\left(\frac{R_{AB}}{s_r^6 R_0^{AB}}\right)^{-\alpha_6}} \qquad (2.63)$$

and

$$f_{\mathrm{dmp}}^{8}(R_{AB}) = \frac{1}{1+6\left(\frac{R_{AB}}{R_0^{AB}}\right)^{\alpha_6+2}}, \qquad (2.64)$$

where s_r^6 is a scaling factor, R_0^{AB} is the cutoff radius for the atom pair (A,B), and α_6 is a parameter, which controls the steepness of the damping functions and is determined in such a way that it gives accurate dispersion correction for specific systems. The original method with the Chai-Head-Godon damping is often referred to as DFT-D3(0) (DFT-D3(zero)), because the damping function approaches zero in the $R_{AB} \rightarrow 0$ limit (zero damping).

In the DFT-D3 method, the C_6 coefficients are determined by taking into account the coordination number as follows: First, the coordination numbers are calculated as

$$\mathrm{CN}^A = \sum_{B \neq A} \frac{1}{1+\exp\left[-16\left(\frac{4\left(R_{A,\mathrm{cov}}+R_{B,\mathrm{cov}}\right)}{3R_{AB}}-1\right)\right]}, \qquad (2.65)$$

where $R_{A(B),\mathrm{cov}}$is the covalent radius determined by Pyykkö and Atsumi [41]. Then the reference C_6 coefficient is calculated by a variation of the Casimir-Polder formulation as

$$C_{6,\mathrm{ref}}^{AB}(\mathrm{CN}^A, \mathrm{CN}^B) = \frac{3}{\pi}\int_0^\infty d\omega \frac{1}{m}\left[\alpha^{A_mH_n}(i\omega) - \frac{n}{2}\alpha^{H_2}(i\omega)\right] \times \frac{1}{k}\left[\alpha^{B_kH_l}(i\omega) - \frac{l}{2}\alpha^{H_2}(i\omega)\right], \qquad (2.66)$$

where A_mH_n and B_kH_l are element hydride molecules, which represent specific coordination numbers. Finally, the coordination number dependent C_6 coefficient is calculated as

$$C_6^{AB}(\mathrm{CN}^A, \mathrm{CN}^B) = \frac{\sum_i^{N_A}\sum_j^{N_B} C_{6,\mathrm{ref}}^{AB}\left(\mathrm{CN}_j^A, \mathrm{CN}_j^B\right)L_{ij}}{\sum_i^N \sum_j^N L_{ij}} \qquad (2.67)$$

with

$$L_{ij} = \exp\left\{-4[\left(\mathrm{CN}^A - \mathrm{CN}_i^A\right)^2 + \left(\mathrm{CN}^B - \mathrm{CN}_j^B\right)^2\right\}, \qquad (2.68)$$

where $N_A(N_B)$ is the number of supporting point i (j) (reference points for different coordination numbers). The C_8 coefficient is calculated as

$$C_8^{AB} = 3C_6^{AB}\sqrt{Q_AQ_B} \qquad (2.69)$$

with

$$Q_A = \frac{\frac{1}{2}\sqrt{Z_A}\langle r^4\rangle_A}{\langle r^2\rangle_A} \qquad (2.70)$$

where $Z_A$is the nuclear charge of the atom A, and $\langle r^4 \rangle_A$, and $\langle r^2 \rangle_A$ are quadrupole and dipole moments based on the atomic density of the atom A.

In contrast to DFT-D2, the scaling parameter s_n in DFT-D3 is set to unity for most of DFT for $n = 6$, and s_8 is adjusted to minimize the error in the dispersion correction.

A variant of DFT-D3 based on the damping function by Becke and Johnson (DFT-D3(BJ)) [42] is given by

$$E_{disp} = -\frac{1}{2}\sum_{A\neq B}\sum_{n=6,8} s_n \frac{C_n^{AB}}{R_{AB}^n + \left(a_1 R_{BJ}^{AB} + a_2\right)^n}, \qquad (2.71)$$

where $a_1$and a_2 are adjustable parameters determined by using a specific data set. The cutoff radius R_{BJ}^{AB} is calculated by

$$R_{BJ}^{AB} = \sqrt{\frac{C_8^{AB}}{C_6^{AB}}} = \sqrt{\frac{3}{2}\sqrt{Z_A}\frac{\langle r^4 \rangle_A}{\langle r^2 \rangle_A}\sqrt{Z_B}\frac{\langle r^4 \rangle_B}{\langle r^2 \rangle_B}} \qquad (2.72)$$

DFT-D3 (BJ) is consider to be slightly superior than the original DFT-D3(0) though the difference is very small. There is another variant of DFT-D3, which relies only on the six-order term (C_6 only), therefore termed DFT-D3(CSO). In this work, we use DFT-D3(BJ) in the TURBOMOLE calculation (chapter 4).

2.5.2 The van der Waals density functional (vdW-DF)

In the dispersion corrected DFT methods, dispersion coefficients need to be obtained from the literature or be calculated. Also, some empirical parameters are included, which have to be determined a priori. It is desirable to use a method with least empiricism based on DFT as the system of our interest is becoming more and more complex, and the state-of-the-art wave-function-based methods or many-body perturbation theory based methods cannot afford such complex systems. The van der Waals density functional (vdW-

DF) [43-46] is a method based purely on the electron density and in principle does not rely on empirical parameters. Starting from the exact exchange-correlation energy within the adiabatic-connection fluctuation-dissipation theorem, Langreth, Lundqvist, and coworkers devised the nonlocal correlation, which is based on the approximation based on the physical constraint, such as *f*-sum rule, but without any empirical parameters. The nonlocal correlation can be regarded as a correction to the local exchange-correlation functional as

$$E_{\mathrm{xc}} = E_{\mathrm{xc}}^{0} + E_{\mathrm{c}}^{\mathrm{nl}}, \tag{2.73}$$

where E_{xc}^{0} is the local exchange-correlation functional and E_{c}^{nl} is given by

$$E_{\mathrm{c}}^{\mathrm{nl}} = \iint d\boldsymbol{r}\, d\boldsymbol{r}' n(\boldsymbol{r})\phi(\boldsymbol{r},\boldsymbol{r}')n(\boldsymbol{r}'), \tag{2.74}$$

with $\phi(r,r')$ being the so-called vdW kernel. The kernel depends on the scaled electron coordinate

$$d = q_0(\boldsymbol{r})|\boldsymbol{r}-\boldsymbol{r}'| \tag{2.75}$$

$$d' = q_0(\boldsymbol{r}')|\boldsymbol{r}-\boldsymbol{r}'| \tag{2.76}$$

where $q_0(\boldsymbol{r})$ depends on $n(\boldsymbol{r})$ and $|\nabla n(\boldsymbol{r})|$. It is shown that the kernel vanishes in the uniform electron density limit and that $\phi \to C|r-r'|^{-6}$ in the asymptotic limit $|r-r'| \to \infty$, guaranteeing that the nolocal correlation is able to describe the dispersion forces.

In their first vdW-DF for general geometries (vdW-DF1), Dion *et al* proposed the following form [44]

$$E_{\mathrm{xc}} = E_{\mathrm{x}}^{\mathrm{revPBE}} + E_{\mathrm{c}}^{\mathrm{LDA}} + E_{\mathrm{c}}^{\mathrm{nl}}, \tag{2.77}$$

where $E_{\mathrm{x}}^{\mathrm{revPBE}}$ and $E_{\mathrm{c}}^{\mathrm{LDA}}$ are the revPBE exchange and LDA correlation functionals, respectively. The choice of the revPBE exchange was made, because the exchange functional best mimics the interaction energy obtained by using the exact exchange when vdW-DF1 was proposed. The LDA was used for the local correlation, because the nonlocal

correlation contains the density gradient and avoid possible double counting of the gradient correction to the correlation energy.

Despite its simplicity, the vdW-DF is shown to describe the diverse systems reasonably accurately, ranging from covalent, ionic, and vdW bondings on the same footing. However, it turned out that although vdW-DF1 predicts the binding energies reasonably accurately, it consistently overestimates the bond length, lattice constant, and binding distance, needing further improvement of the vdW-DF functional. Among others[47-50], Hamada proposed rev-vdW-DF2 [51] , which is based on the nonlocal correlation functional of vdW-DF2 by Lee *et al.* [52] and on the revised Becke exchange (B86b) [53]. The revised B86b, termed B86R [54] is designed to satisfy the gradient expansion approximation in the slowly varying density limit which is exact, and to reproduce the large density gradient behavior set in the original B86b exchange, as it is developed for the inhomogeneous electron density region relevant to the vdW bondings and its exchange enhancement factor is proportional to $s^{\frac{2}{5}}$ where s is the reduced density gradient, the s dependence suggested for an accurate exchange functional by Murray, Lee, and Langreth [55]. The rev-vdW-DF2 has been show to describe a variety of systems including small molecular complexes, inorganic/organic solids, and adsorption systems [51]. To study the adsorption and chemical reaction of hfacH molecule on metallic Ni surfaces (chapter 5), we used rev-vdW-DF2 as implemented in the STATE code. The implementation of the simplified $O(N\log N)$ implementation of vdW-DF [56,57] is described in Ref. [58].

2.6 Basis function

2.6.1 Gaussian type orbital

In the calculation of a molecular/cluster system it is common to use the linear combination of atomic orbitals (AOs), and to define the AOs, the Slater type orbital (STO) is used [59]:

$$\chi_{\zeta,n,l,m}(r,\theta,\phi) = Nr^{n-1}Y_{lm}(\theta,\phi)e^{-\zeta r}, \qquad (2.78)$$

where r is the distance between the electron and the nucleus at which the STO is centered, θ and ϕ are angular coordinates, N is a normalization constant, Y_{lm} is a spherical harmonic function, ζ is called the orbital exponent. Here n is the principle quantum number, l is the azimuthal quantum number, and m is the magnetic quantum number. In the modern quantum chemistry, however, it is common to use the follow Gaussian type orbitals (GTO) [60]

$$\chi_{\zeta,n,l,m}(r,\theta,\phi) = Nr^{2n-2-l}Y_{lm}(\theta,\phi)\mathrm{e}^{-\zeta r^2}, \qquad (2.79)$$

or in the Cartesian coordinate as

$$\chi_{\zeta,i,j,k}(x,\mathrm{y},z) = Nx^i y^j z^k \mathrm{e}^{-\zeta r^2}, \qquad (2.80)$$

where ζ is the orbital exponent which defines the radial extent of the function, and i, j, k define the angular momentum of the AOs.

2.6.2 Plane wave basis

It is a common practice to use a basis set to express the solution of the Schrodinger (Hartree-Fock/Kohn-Sham) equation. In a solid state calculation, the crystal is described

by using the periodic boundary condition and the one-electron wave functions must obey the Bloch theorem

$$\psi_{\boldsymbol{k}}(\boldsymbol{r}+\boldsymbol{R}) = e^{i\boldsymbol{k}\cdot\boldsymbol{R}}\psi_{\boldsymbol{k}}(\boldsymbol{r}), \qquad (2.81)$$

where $\boldsymbol{k}$ is the wave vector of the wave function and $\boldsymbol{R}$ is a real-space lattice vector. A natural choice for the basis function under the periodic boundary condition is the plane-wave, as it inherently obeys the Bloch theorem. A wave function of crystal under the periodic boundary condition characterized by the wave vector $\boldsymbol{k}$ can be given by

$$\psi_{\boldsymbol{k}}(\boldsymbol{r}) = \frac{1}{\Omega}\sum_{\boldsymbol{G}} c_{\boldsymbol{k}}(\boldsymbol{G}) e^{i(\boldsymbol{k}+\boldsymbol{G})\cdot\boldsymbol{r}}, \qquad (2.82)$$

where Ω is the volume of the whole crystal, $\boldsymbol{G}$ is the reciprocal lattice vector, and $c_{\boldsymbol{k}}(\boldsymbol{G})$ is the expansion coefficient. In principle the expansion is exact when the infinite number of the reciprocal lattice vectors are used, but in practice, it is truncated at the cutoff wave vector $G_{\mathrm{cut}}^{\mathrm{wf}}$ defined by

$$E_{\mathrm{cut}}^{\mathrm{wf}} = \frac{\hbar^2}{2m}\left|k + G_{\mathrm{cut}}^{\mathrm{wf}}\right|^2 \qquad (2.83)$$

and $E_{\mathrm{cut}}^{\mathrm{wf}}$ is called the kinetic energy cutoff (for the wave functions). Similary, the electron density can be expanded in terms of the plane-wave basis, and the expansion is truncated at the cutoff vector $G_{\mathrm{cut}}^{\mathrm{den}}$ defined by

$$E_{\mathrm{cut}}^{\mathrm{den}} = \frac{\hbar^2}{2m}\left|G_{\mathrm{cut}}^{\mathrm{den}}\right|^2. \qquad (2.84)$$

In the case of the normconserving pseudopotential (without the nonlinear core correction for the pseudopotential), $E_{\mathrm{cut}}^{\mathrm{den}} = 4 \times E_{\mathrm{cut}}^{\mathrm{wf}}$ or $G_{\mathrm{cut}}^{\mathrm{den}} = 2 \times G_{\mathrm{cut}}^{\mathrm{wf}}$, and in the case of the ultrasoft pseudopotential (USPP) or projector augmented wave (PAW) methods, this relation does not hold, and a large cutoff energy for the electron density is required because of the augmentation charge inherent in USPP and PAW methods.

2.7 Pseudopotential or effective core potential (ECP)

Because of the very attractive Coulomb potentials in the vicinity of nuclei, the wave functions for the core states are highly localized and oscillate strongly, and therefore tremendous number of basis functions is required to describe them with a plane wave basis set accurately. To alleviate this problem, different types of basis functions have been proposed, including the augmented plane-wave, mixed basis, numerical atomic orbital, and Gaussian type orbital, name only a few. An alternative approach is the use of pseudopotentials, or effective core potentials (ECP), in which bare Coulomb potential is replaced with that effectively screened by the electrons in the core states. The basic idea is that the electrons in the core states are bound by the strong Coulomb electrons and are chemically inert and only the electrons in the valence states contribute to the chemical bonding in molecules and/or solids. The pseudopotential method allows one to use the plane-wave basis set and keeps the formulation of e.g., total energy and its derivatives. The nonempirical pseudopotential (or *ab initio* pseudopotential) is, however, not uniquely constructed, and there are several types of pseudopotentials, including the norm-conserving pseudopotential (NCPP) [61-66] and ultrasoft pseudopotential (USPP) [67]. An alternative formulation exists, which is called projector augmented wave (PAW) method [68]. The PAW method is an all-electron method, i.e., it can treat core states when necessary, but it works with the pseudo-wave functions (valence electron states) within the frozen core approximation in practice, and its complexity of the formulation and computational cost are similar to those of USPP.

2.8 References

[1] E. Fermi, Z. Physik 48, 73 (1928).

[2] L. H. Thomas, Proc. Camb. Phil. Soc. 23, 542 (1926).

[3] P. A. M. Dirac, Proc. Camb. Phil. Sot., 26, 376 (1930).

[4] N.H. March, Advances in Physics, 6, 1 (1957).

[5] P. Hohenberg and W. Kohn, Phys. Rev. 136 (3B), B864 (1964).

[6] W. Kohn and L.J. Sham, Physical Review 140, A1133 (1965).

[7] D. M. Ceperley and B. J. Alder, Phys. Rev. Lett. 45, 566 (1980).

[8] S. H. Vosko, L. Wilk, and M. Nusair, J. Phys. 58, 1200, (1980).

[9] J. P. Perdew and A. Zunger, Phys. Rev. B 23, 5048 (1981).

[10] J. P. Perdew and Y. Wang, Phys. Rev. B 45, 13244 (1992).

[11] J. P. Perdew, *in Electronic Structure of Solids '91*, edited by P. Ziesche and H. Eschrig, Akademie Verlag, Berlin, 11 (1991).

[12] J. P. Perdew, K. Burke, and M. Ernzerhof, Phys. Rev. Lett. 77, 3865 (1996).

[13] Y. Zhang and W. Yang, Phys. Rev. Lett. 80, 890 (1998).

[14] B. Hammer, L. B. Hansen, and J. K. Norskov, Phys. Rev. B 59, 7413 (1999).

[15] J. P. Perdew, A. Ruzsinszky, G. I. Csonka, O. A. Vydrov, G. E. Scuseria, L. A. Constantin, X. Zhou, and K.Burke, Phys. Rev. Lett. 100, 136406 (2008).

[16] Z. Wu and R. E. Cohen, Phys. Rev. B 73, 235116 (2006).

[17] C. Adamo and V. Barone, J. Chem. Phys.110, 6158 (1999).

[18] J. P. Perdew, M. Ernzerhof, and K. Burke, J. Chem. Phys. 105, 9982 (1996).

[19] A. D. Becke, J. Chem. Phys. 98, 5648 (1993).

[20] A. D. Becke, Phys. Rev. A. 38, 3098 (1988).

[21] C. Lee, W. Yang, and R. G. Parr, Phys. Rev. B 37, 785 (1988).

[22] S. H. Vosko, L. Wilk, and M. Nusair, Can. J. Phys. 58, 1200 (1980).

[23] J. Paier, R. Hirschl, M. Marsman, and G. Kresse, J. Chem. Phys. 122, 234102 (2005).

[24] P. Verma, and D. G. Truhlar, Theor. Chem. Acc. 135, 182 (2016).

[25] V. I. Anisimov, J. Zaanen, and O. K. Andersen, Phys. Rev. B 44, 943 (1991).

[26] S. L. Dudarev, G. A. Botton, S. Y. Savrasov, C. J. Humphreys, and A. P. Sutton, Phys. Rev. B 57, 1505 (1998).

[27] S. Mandal, K. Haule, K.M. Rabe, and D. Vanderbilt, Npj Comput. Mater. 5, 1 (2019).

[28] M. Elstner, P. Hobza, T. Frauenheim, S. Suhai, and E. Kaxiras, J. Chem. Phys. 114, 5149 (2001).

[29] X. Wu, M. C. Vargas, S. Nayak, V. Lotrich, and G. Scoles, J. Chem. Phys. 115, 8748 (2001).

[30] Q. Wu and W. Yang, J. Chem. Phys. 116, 515 (2002).

[31] D.C. Langreth, M. Dion, H. Rydberg, E. Schröder, P. Hyldgaard, and B.I. Lundqvist, Int. J. Quantum Chem. 101, 599 (2004).

[32] M. Dion, H. Rydberg, E. Schröder, D.C. Langreth, and B.I. Lundqvist, Phys. Rev. Lett. 92, 246401 (2004).

[33] D.C. Langreth, B.I. Lundqvist, S.D. Chakarova-Käck, V.R. Cooper, M. Dion, P. Hyldgaard, A. Kelkkanen, J. Kleis, L. Kong, S. Li, P.G. Moses, E. Murray, A. Puzder, H. Rydberg, E. Schröder, and T. Thonhauser, J. Phys.: Condens. Matter 21, 084203 (2009).

[34] K. Berland, V.R. Cooper, K. Lee, E. Schröder, T. Thonhauser, P. Hyldgaard, and B.I. Lundqvist, Rep. Prog. Phys. 78, 066501 (2015).

[35] J. Klimeš and A. Michaelides, J. Chem. Phys. 137, 120901 (2012).

[36] J. Herman, R. DiStasio Jr. A. Tkatchenko, Chem. Rev. 117, 4714 (2017).

[37] S. Grimme, J. Comput. Chem. 27, 1787 (2006).

[38] S. Grimme, J. Antony, S. Ehrlich, and H. Krieg, J. Chem. Phys. 132, 154104 (2010).

[39] S. Grimme, S. Ehrlich, and L. Goerigk, J. Comput. Chem. 32, 1456 (2011).

[40] D. Chai and M. Head-Gordon, Phys. Chem. Chem. Phys. 10, 6615 (2000).

[41] P. Pyykkö and M. Atsumi, Chem. 15, 12770 (2009).

[42] E. R. Johnson, and A. D. Becke, J. Chem. Phys., 123, 024101 (2005).

[43] D.C. Langreth, M. Dion, H. Rydberg, E. Schröder, P. Hyldgaard, and B.I. Lundqvist, Int. J. Quantum Chem. 101, 599 (2004).

[44] M. Dion, H. Rydberg, E. Schröder, D.C. Langreth, and B.I. Lundqvist, Phys. Rev. Lett. 92, 246401 (2004).

[45] D.C. Langreth, B.I. Lundqvist, S.D. Chakarova-Käck, V.R. Cooper, M. Dion, P. Hyldgaard, A. Kelkkanen, J. Kleis, L. Kong, S. Li, P.G. Moses, E. Murray, A. Puzder, H. Rydberg, E. Schröder, and T. Thonhauser, J. Phys.: Condens. Matter 21, 084203 (2009).

[46] K. Berland, V.R. Cooper, K. Lee, E. Schröder, T. Thonhauser, P. Hyldgaard, and B.I. Lundqvist, Rep. Prog. Phys. 78, 066501 (2015).

[47] J. Klimeš, D.R. Bowler, and A. Michaelides, J. Phys.: Condens. Matter 22, 022201 (2010).

[48] J. Klimeš, D.R. Bowler, and A. Michaelides, Phys. Rev. B 83, 195131 (2011).

[49] V.R. Cooper, Phys. Rev. B 81, 161104 (2010).

[50] I. Hamada and M. Otani, Phys. Rev. B 82, 153412 (2010).

[51] I. Hamada, Phys. Rev. B 89, 121103 (2014).

[52] K. Lee, É.D. Murray, L. Kong, B.I. Lundqvist, and D.C. Langreth, Phys. Rev. B 82, 081101 (2010).

[53] A.D. Becke, J. Chem. Phys. 85, 7184 (1998).

[54] A. D. Becke, J. Chem. Phys. 107, 8554 (1997).

[55] E. D. Murray, K. Lee, and D. C. Langreth, J. Chem. Theory Comput. 5, 2754 (2009).

[56] G. Román-Pérez and J.M. Soler, Phys. Rev. Lett. 103, 096102 (2009).

[57] J. Wu and F. Gygi, J. Chem. Phys. 136, 224107 (2012).

[58] Y. Hamamoto, I. Hamada, K. Inagaki, and Y. Morikawa, Phys. Rev. B 93, 245440 (2016).

[59] J. C. Slater, Phys. Rev. 36, 57 (1930).

[60] S. F. Boys, Proc. Roy. Soc. London Ser A 200, 542 (1950).

[61] D.R. Hamann, M. Schlüter, and C. Chiang, Phys. Rev. Lett. 43, 1494 (1979).

[62] G. B. Bachelet, D. R. Hamann, and M. Schlüter, Phys. Rev. B 26, 4199 (1982).

[63] N. Troullier and J. L. Martins, Phys. Rev. B 43, 1993 (1991).

[64] A. M. Rappe, K. M. Rabe, E. Kaxiras and J. D. Joannopoulos, Phys. Rev. B41, 1227 (1990).

[65] P. E. Blöchl, Phys. Rev. B 41, 5414(R) (1990).

[66] D. Vanderbilt, Phys. Rev. B 32, 8412 (1985).

[67] D. Vanderbilt, Phys. Rev. B 41, 7892(R) (1990).

[68] P. E. Blöchl, Phys. Rev. B 50, 17953 (1994).

CHAPTER 3:

Stability of Hexafluoroacetylacetone Molecules on Metallic and Oxidized Nickel Surfaces in Atomic-Layer-Etching (ALE) Processes*

---

* Abdulrahman H. Basher, M. Krstić, T. Takeuchi, M. Isobe, T. Ito, M. Kiuchi, K. Karahashi, W. Wenzel, and S. Hamaguchi, "Stability of hexafluoroacetylacetone molecules on metallic and oxidized nickel surfaces in atomic layer etching (ALE) Processes," J. Vac. Sci. Technol. A 38, 022610 (2020). https://doi.org/10.1116/1.5127532

3.1 Introduction

Atomic layer etching (ALE) by the formation of volatile organic metal complexes is expected to establish low damage and atomically controlled etching processes [1-9]. Hexafluoroacetylacetone (hfacH) may be used as an etchant gas for etching of various metal oxides including magnetic materials [1,5,6,10,11]. The expected sequence of hfacH etching of a Ni surface is illustrated in the first chapter in section 1.2.2.

Interactions between enol hexafluoroacetylacetone (hfacH) with nickel oxide (NiO) fcc (100) and metallic Ni fcc (100) surfaces have been examined in this chapter with the use of first-principles quantum mechanical (QM) simulation. It is shown that an hfacH molecule is unlikely to be deprotonated but can be dissociated on a Ni metal surface. On the other hand, an hfacH molecule can be deprotonated on a NiO surface, forming a hexafluoroacetylacetonate anion ($hfac^-$) bonded with positively charged Ni atoms of the NiO surface. As the first step for understanding why an hfacH molecule is decomposed on a Ni surface while it forms $Ni(hfac)_2$ on a NiO surface, we have examined the stability of adsorbed hfacH molecules on Ni and NiO surfaces, using the first-principles QM simulations. The stability of hfacH molecules on Ni and NiO surfaces can be considered as the first step to understand the thermal ALE processes of a Ni surface by hfacH gas specifically and the thermal ALE processes of a metal surface by organic gas in general which is discussed in this chapter.

3.2 Methodology

The simulation of this study was performed with GAUSSIAN 09 Revision D.01 [12] software. The QM simulation is based on the density functional theory (DFT) with the

B3LYP functional [13-15] and the 6-311G (d) AO basis set [16]. The QM simulation was used to evaluate the total energy of a system consisting of multiple atoms (e.g., a single molecule or a system of a molecule interacting with a surface) in its ground state when the positions of all nuclei were fixed in space. The QM simulation was also used to obtain the most stable atomic configuration (geometric configuration) of a system at zero temperature. The latter is called geometry optimization. Partial geometry optimization can be performed with the positions of some selected atoms being fixed.

The accuracy of system energy evaluated by such simulation depends on the assumptions used in the numerical techniques. In the DFT framework, the most suitable functionals need to be selected for the quantitative evaluation of the system energy. However, it cannot be known a priori in which functionals are the most suitable for the system one wants to calculate. It is generally believed that B3LYP offers reasonable computational results for organic systems as well as systems containing transition metals such as Ni [13-15]. This is why we used B3LYP in our simulation presented in this study. However, there have been many studies comparing various functionals for DFT calculations [14,15,17-20], which typically show that the selection of best functionals depends on the system and the physical quantities (such as reaction energies, bond lengths, band structures, vibrational frequency shifts, etc.) to be evaluated. Discussion on the most appropriate selection of DFT functionals is beyond the scope of the present work and deferred to a future study.

Similarly, we used the 6-311G(d) basis set as it is widely used in DFT calculations in general [16]. It should be noted, however, that the 6-311G(d) basis set does not include the diffuse functions, the use of which could improve the representation of highly polarized

atoms. Furthermore, we did not include the dispersion interaction (i.e., van der Waals interaction) in this simulation for the sake of simplicity. The dispersion interactions have much lower attractive interaction energies than those of typical covalent bond interactions but are of much longer range. In this study, we assume that the effects of dispersion interactions on adsorption energies are relatively minor and do not alter this conclusion on the adsorption mechanisms of hfacH on Ni and NiO surfaces. However, the inclusion of dispersion interactions is necessary for the quantitative evaluation of adsorption energies and barriers.

Owing to the high cost of QM simulations in general, it is practically impossible to employ, as a computational model system, a realistic system comprising an hfacH molecule incident upon a surface material that consists of a large number of atoms. Therefore, to represent the material surfaces, we used reduced models of single monolayers that can capture the essential nature of the real NiO and Ni surfaces. Figure 3-1 shows the top views of the (100) single-monolayer rectangular surfaces of fcc NiO (8.89 Å × 8.89 Å) and Ni (7.48 Å × 4.98 Å). In each case, the total net charge was assumed to be zero. In the geometry optimization of an hfacH adsorption process performed in this study, the positions of all surface atoms were fixed while the geometric structure of an hfacH molecule was optimized. In reality, as an adsorbate molecule approaches the surface, the positions of surface atoms interacting with the adsorbate can change. However, we assumed that such changes in the positions of surface atoms were sufficiently small. The geometry optimization was performed with gradient minimization techniques.

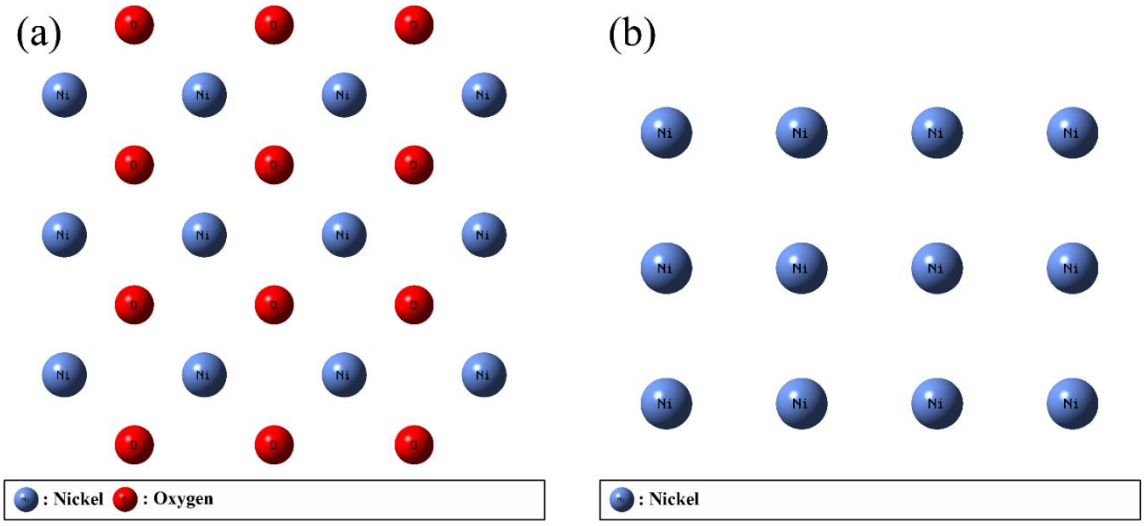


Fig. 3-1: Top views of the single-monolayer surface models used in the simulations. (a) 8.89 × 8.89 $Å^2$ square (100) surface of fcc NiO and (b) 7.48 × 4.98 $Å^2$ rectangular (100) surface of fcc Ni.

As mentioned earlier, the goal of this study is to present qualitative insight into the mechanisms of the adsorption of hfacH on Ni and NiO surfaces. As the first step, we looked at the adsorption processes of an hfacH molecule with Ni and NiO simple single-layer surface models mentioned above. To simplify the simulation further, we have employed several approximations for DFT calculations, as discussed earlier. The validity of the surface models as well as the use of the approximations for DFT calculations must be validated eventually. However, our preliminary DFT calculations of the same adsorption processes with larger and more realistic surface models based on different DFT calculation methods including dispersion interactions have also shown that the results are qualitatively consistent with what is presented in this article. Therefore, we are confident that our simulation results presented in this article help me understand, at least qualitatively, the mechanisms on how an hfacH molecule interacts with a Ni or NiO surface. A systematic

study of the accuracy of the simulation results presented in this article is deferred to the next chapters.

3.3 Results and discussion

First, we optimized the structures of the keto and enol types of hfacH using our simulation, which are shown in Fig. 3-2. The enol-type hfacH is known to be more stable than the keto-type. The energy difference obtained from our simulation is −27.48 kJ/mol (−0.285 eV), which is consistent with the results of earlier studies [21-25]. This result implies that the majority of hfacH in the gas phase exists in the enol form and therefore, in the simulations herein, we used only the enol-type hfacH as an adsorbate.

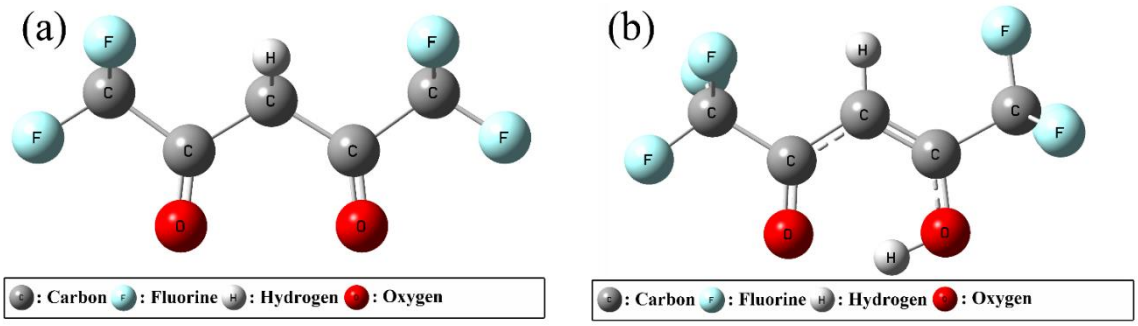


Fig. 3-2: Simulated optimized structures of (a) keto-type and (b) enol-type hfacH molecules. The enol-type hfacH is more stable than the keto-type, with an energy difference of −0.285 eV.

To obtain partial charge distributions, we used a natural bond orbital (NBO) population analysis. Figure 3-3 shows the NBO charge distributions of both types of hfacH. Figure 3-3(a) shows that the oxygen atoms are the most negatively charged with a charge of −0.448 *e* (with *e* being the elementary charge) in the keto-type. Further, Fig. 3-3(b) shows that the oxygen bonded with the hydrogen atom has a charge of −0.615 *e* while the

other oxygen atom has a charge of −0.570 *e* for the enol-type. It should be noted that the fluorine atoms are negatively charged (−0.335 to −0.356 *e*) whereas the carbon atoms of trifluoromethyl (−CF_3) groups are highly positively charged (+1.050 to +1.075 *e*), which makes hfacH a highly polarized molecule.

We also examined the charge distributions of the model surfaces, as shown in Fig. 3-4. As expected, the simulation shows that NiO is an ionic crystal that consists of positively-charged Ni and negatively-charged O atoms. In contrast, the Ni atoms of the metallic Ni surface are nearly charge-neutral.

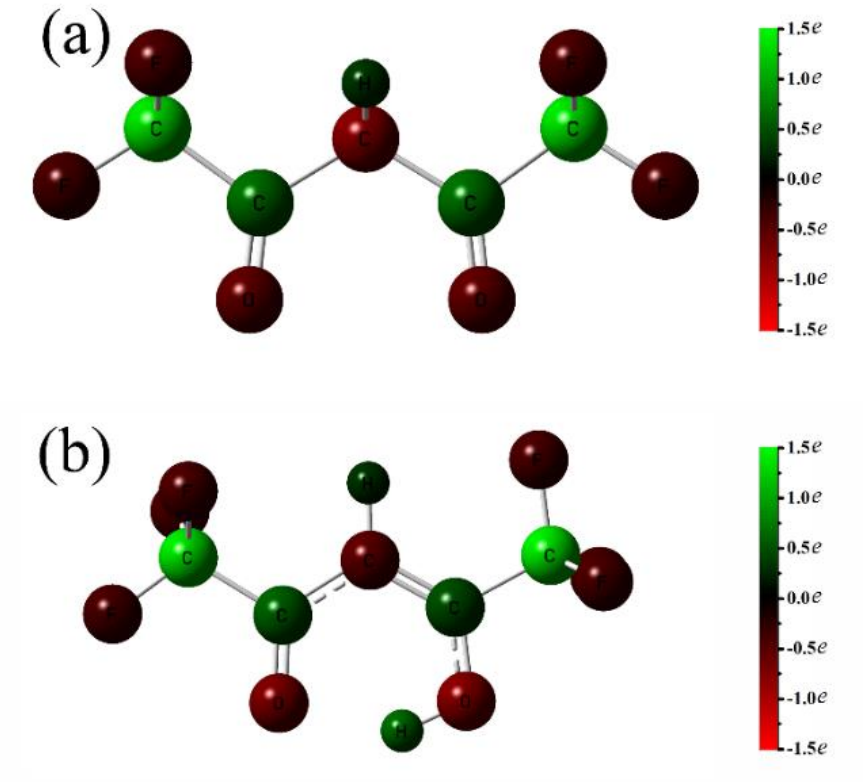


Fig. 3-3: NBO charge distribution from -1.5 *e* (red color) to 1.5 *e* (green color) of (a) keto-type and (b) enol-type hfacH molecules. It is seen that oxygen atoms are most negatively charged in each molecule.

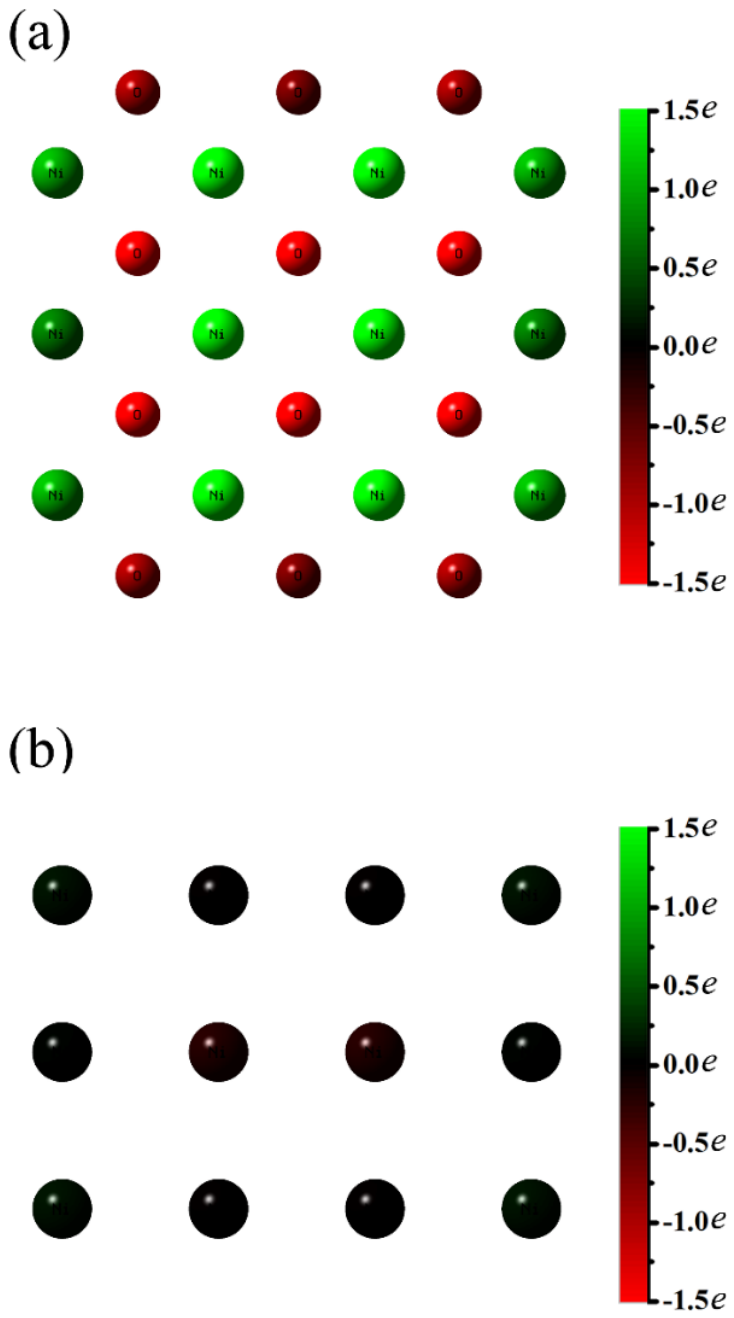


Fig. 3-4: NBO charge distribution from −1.5 *e* (red color) to 1.5 *e* (green color) of model surfaces of (a) NiO and (b) Ni given in Fig. 3-1. It is seen that NiO is an ionic crystal that consists of positively charged Ni and negatively charged O atoms, whereas Ni of the metallic surface is nearly charge neutral.

Now, we examine how an hfacH molecule interacts with the model NiO surface of Fig. 3-4 (a) when it approaches the surface.

There are many possibilities for the orientation of an hfacH molecule when it approaches a surface. In this study, we studied three different orientations of an hfacH molecule: (1) an hfacH molecule vertically aligned toward the NiO surface with the oxygen atoms closer to the surface, as shown in Fig. 3-5 (this atomic configuration was called "NiO + hfacH"); (2) an hfacH molecule vertically aligned toward the surface but in the opposite direction, with the F atoms being closer to the surface, as shown in Fig. 3-6 ("NiO + inv. hfacH"); and (3) an hfacH molecule tilted at an angle of 56° from the configuration, as shown in Fig. 3-7 ("NiO ~56° hfacH"). The tilting angle was measured from the surface normal so that the vertical hfacH was defined as tilted at an angle of 0°. In all three cases, each O atom of the hfacH molecule was placed nearly above one of the two central Ni atoms of the surface with the same distance from the NiO surface plane.

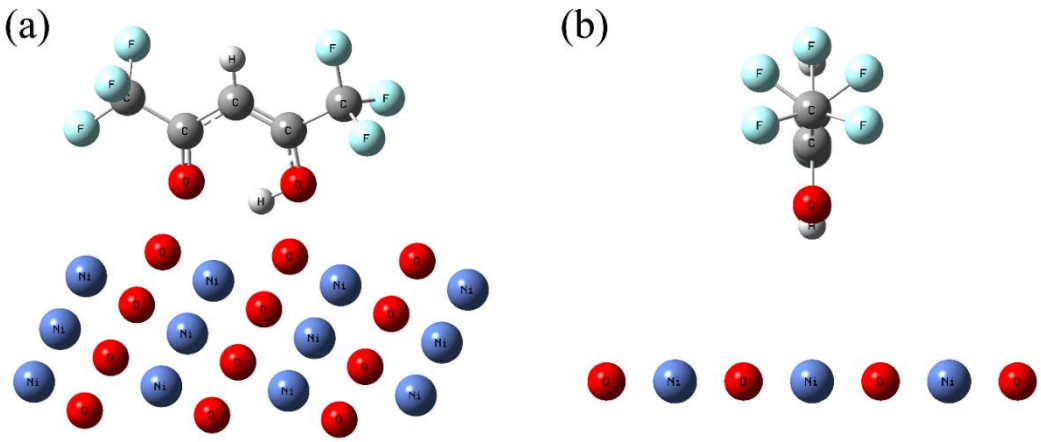


Fig. 3-5: "NiO + hfacH", where an hfacH molecule is vertically placed on a NiO monolayer; (a) front view and (b) side view.

In the simulation, we first evaluated the "interaction energy" between an hfacH molecule of a fixed geometric configuration and the fixed model surface as a function of the distance between the molecule and the model surface. The distance between the hfacH molecule and the surface was defined as the position of the O atoms of the hfacH molecule

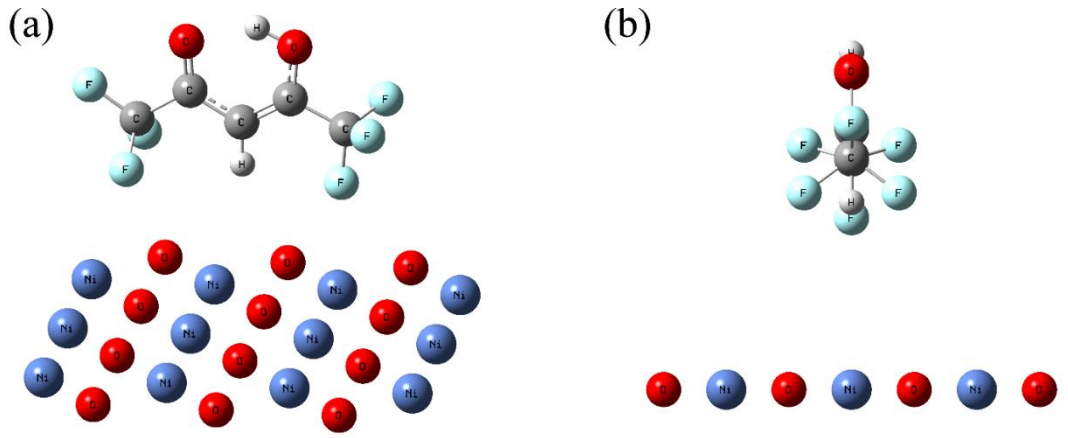


Fig. 3-6: "NiO + inv. hfacH", where an inverted hfacH molecule is vertically placed on a NiO monolayer; (a) front view and (b) side view.

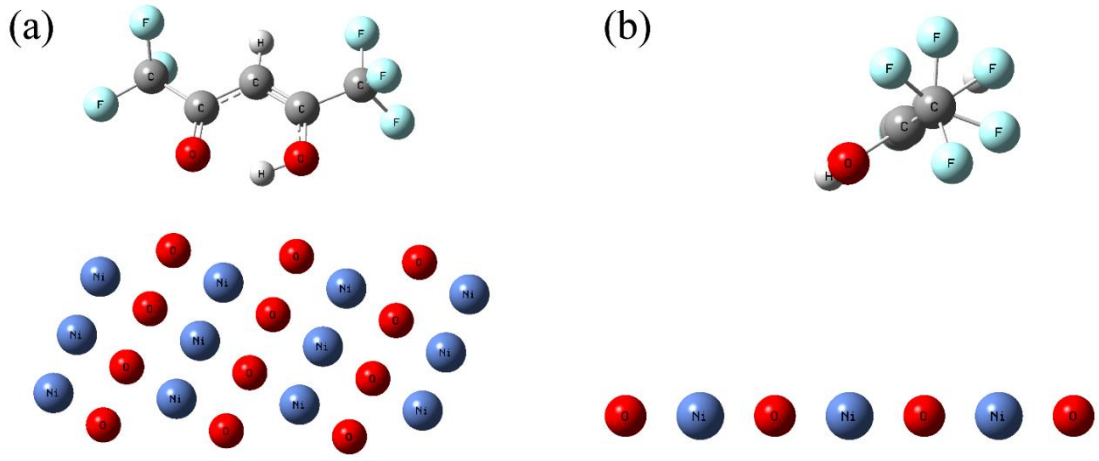


Fig. 3-7: "NiO ~ 56° hfacH", where an hfacH is tilted at an angle of 56° on a NiO monolayer; (a) front view and (b) side view.

measured from the NiO surface plane. In this configuration, the two O atoms were placed parallel to the NiO surface plane. The "interaction energy" was defined as

$$\text{Interaction energy} = E_t - E_1 - E_2, \qquad (3.1)$$

where E_t is the total energy of the system, E_1 is the total energy of the hfacH molecule, and E_2 is the total energy of the NiO model surface, all at zero temperature. Figure 3-8 gives the interaction energy from Eq. (1) for an hfacH molecule with an atomic configuration of Fig. 3-2(b) and orientation of Figs. 3-5, 3-6 or 3-7, and the model (100) NiO surface of Fig. 3-4(a), as functions of the distance between the hfacH molecule and the surface. No

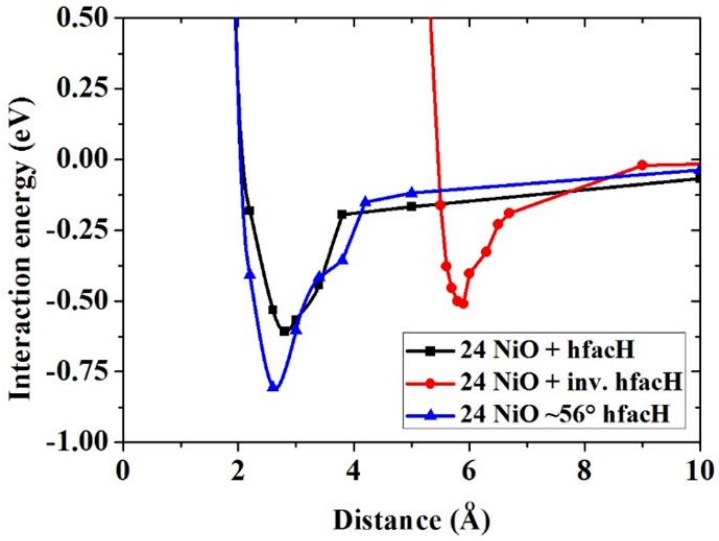


Fig. 3-8: Interaction energies between the NiO surface and hfacH molecules with the three different orientations given in Figs. 3-5,3-6, and3-7 as a function of the distance between the surface and the hfacH molecule, defined as the position of the O atoms of the hfacH molecule measured from the NiO surface plane. It should be noted that no geometry optimization is performed in this simulation so that the atomic configuration of an hfacH atoms is the same as that of Fig. 3-2(b) (of enol-type) and the surface model is given by Fig. 3-4(a). The curves and lines are guides for the eye.

geometry optimization was performed for this evaluation. In this sense, these calculation results only present a rough idea of how hfacH molecules in the three different orientations given in Figs. 3-5, 3-6, and 3-7 interact with the NiO surface. Figure 3-8 suggests that the tilted hfacH molecule interacts with the NiO surface most stably with the lowest interaction energy among the three cases examined here.

Based on this observation, we placed a 56° tilted hfacH molecule at a distance of 2.6 Å (i.e., the lowest-energy position in Fig. 3-8) above the NiO surface as the initial configuration and performed a geometry optimization. As mentioned earlier, all surface Ni and O atoms were assumed to be immobile but the positions of all atoms of the hfacH molecule were optimized. The atomic configuration of the minimum energy state of this system is shown in Fig. 3-9. It is seen that the hfacH molecule is deprotonated, with the hydrogen (H) atom between its two oxygen atoms transferred to one of the oxygen atoms of the NiO surface. As a result, the hexafluoroacetylacetonate anion ($hfac^-$) is bonded with the NiO surface with an interaction of the two O atoms of $hfac^-$ with two adjacent Ni atoms of the NiO surface. At least qualitatively, the simulation result here showing that an hfacH molecule is adsorbed stably (in the form of an $hfac^-$ anion) on a NiO surface is consistent with the experimental observations of Refs. [1] and [7].

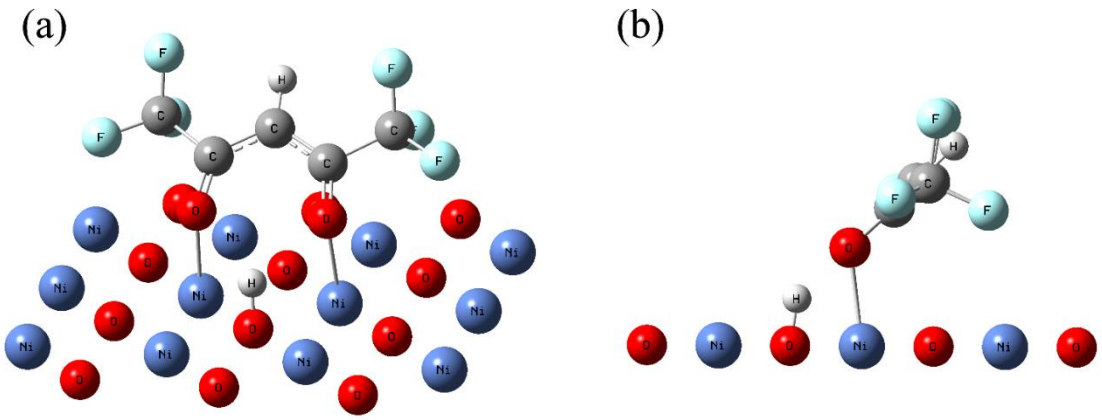


Fig. 3-9: Optimized structure of an hfacH adsorbed on the NiO model surface; (a) front view and (b) side view. It is seen that, after structure optimization of hfacH (with a fixed NiO structure), hfacH is deprotonated and $hfac^-$ is stably bonded with the surface.

The interaction energy, as defined in Eq. (1) with the optimization of E_t with fixed positions of all NiO model surface atoms (whose atomic configuration is given in Fig. 3-9), is −2.02 eV, with the zero-point corrected total energy [12]. This is the adsorption energy, or the "reaction energy", of an hfacH molecule's adsorption on the NiO surface for the model system. The bond length between an O atom of $hfac^-$ and its closest Ni atom of the NiO surface is about 2.05 Å and the $hfac^-$ is tilted with an angle of about 46° against the surface normal. The adsorption energy and the bond length obtained in this study are similar to those reported on the adsorption of hfacH on a ZnO surface by Kung and Teplyakov[26]. It should be noted, however, the adsorption energy, bond length, and tilting angle are given above are obtained from our DFT calculations of simplified models and should not be construed as the exact values of the real system, as we cautioned in the previous section.

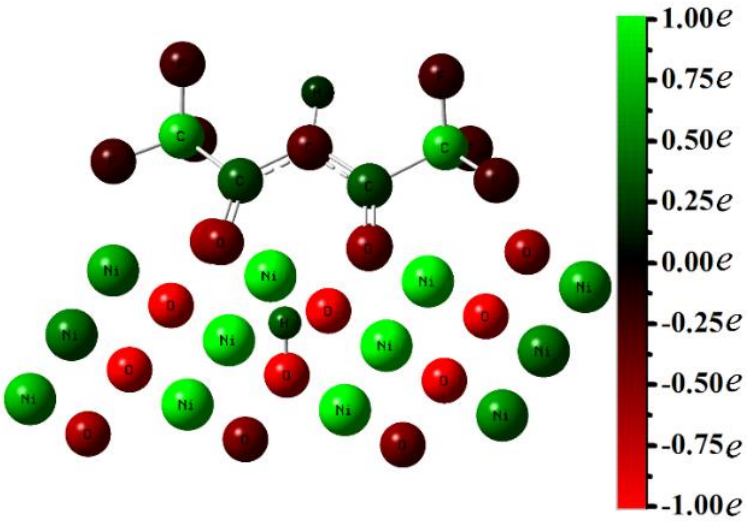


Fig. 3-10: NBO charge distribution from -1.0 *e* (red color) to 1.0 *e* (green color) of the system given in Fig. 3-9.

The electrical charge distribution (NBO population) of the system of Fig. 3-9 is shown in Fig. 3-10. The NBO charge distribution of the H atom on the NiO surface is 0.844 *e* and the total charge of $hfac^-$ shown in Fig. 3-10 is −0.844 *e*. The simulation result suggests that deprotonation of an hfacH molecule occurs because of the presence of negatively-charged O atoms on the surface. In addition, it is clearly seen that the negatively-charged O atoms of $hfac^-$ are bonded with positively-charged Ni atoms. In other words, the presence of ionic bonds; i.e., the fact that Ni atoms are positively charged and O atoms are negatively charged in the NiO surface; is the main reason for the deprotonation and stable adsorption of an hfacH molecule. A similar mechanism should also function for the adsorption of polarized molecules such as diketones on a surface with ionic bonds, such as an oxidized or halogenated metal surface.

We now discuss hfacH adsorption on a metallic Ni surface. It is known that hfacH molecules are dissociated when they approach a metallic Ni surface at room temperature or higher, which has been observed experimentally [1,7]. Figure 3-11 shows the optimized

structure of an hfacH molecule placed at the center of the 7.48 Å × 4.98 Å Ni monolayer surface given in Fig. 3-1(b). The molecule was initially placed at a distance of 2.2 Å above the surface plane with a tilt angle of 56°, in a fashion similar to Fig. 3-9. As before, the distance was defined as the position of the O atoms of the hfacH molecule measured from the surface plane. The two O atoms were originally placed above the two Ni atoms near the center of the rectangular Ni monolayer surface. It is seen in Fig. 3-11 that, after a geometry optimization (with the positions of all Ni atoms being fixed), the hfacH molecule moved closer to the Ni surface and was decomposed without deprotonation. Dissociated F atoms went to the opposite side of the monolayer surface, which of course may not occur in an actual Ni surface. The reaction energy for the atomic configurations given in Fig. 3-11 is −8.70 eV, with the zero-point corrected total energy [12]. This large absolute value of the reaction energy arises from the formation of Ni–F and Ni–C bonds after some F atoms are removed from the hfacH molecule. On a metallic Ni surface, such reaction energy varies depending on how the adsorbed hfacH molecule is decomposed on the surface.

The NBO charge distribution of the system of Fig. 3-11 is shown in Fig. 3-12. It is seen that Ni atoms of the surface are nearly charge-neutral except for those interacting closely with the F and C atoms. The simulation result suggests that, in the case of a metal surface, the negatively-charged O atoms and the positively-charged H atom between them in an hfacH molecule have no particular surface atoms with which to bond because all surface metal atoms are charge-neutral. Therefore, deprotonation of hfacH is unlikely to occur and, if the hfacH molecule is tilted down further, some of its F and C atoms can form bonds with Ni atoms on the surface, as seen in Fig. 3-11.

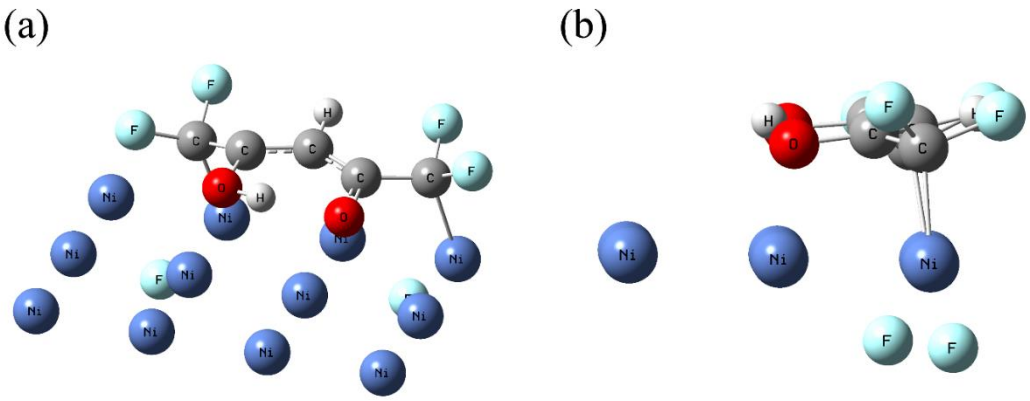


Fig. 3-11: Optimized structure of an hfacH molecule placed near a metallic Ni model surface given in Fig. 3-1(b); (a) front view and (b) side view.

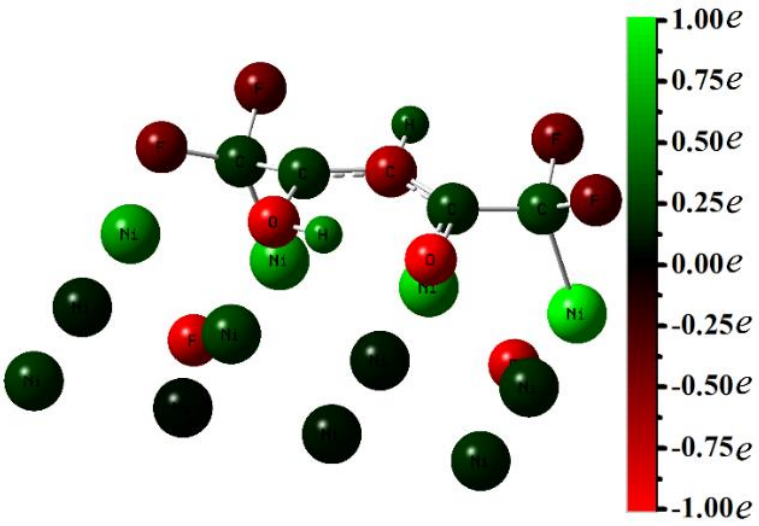


Fig. 3-12: NBO charge distribution from -1.0 *e* (red color) to 1.0 *e* (green color) of the system given in Fig. 3-11.

3.4 Summary

In this chapter, DFT-based first-principles QM simulations were used to clarify why hfacH can be adsorbed stably on a NiO surface while it can be dissociated on a metallic Ni surface. The simulation results showed that, when a stable enol hfacH molecule approaches a NiO surface, its negatively-charged O atoms are attracted to Ni atoms of the NiO surface, where all Ni atoms are positively charged. If the distance between the hfacH molecule and the NiO surface is sufficiently short, the system becomes more stable once the H atom located between the two O atoms of hfacH is transferred to a nearby surface O atom. In this process, the dissociated H atom is positively charged and the remaining part, i.e., $hfac^{-}$, is negatively charged (i.e., deprotonation of hfacH). Because of this charge transfer, the two negatively-charged O atoms of $hfac^{-}$ are bonded more strongly with positively-charged surface Ni atoms. Once this structure is established, the adsorbed $hfac^{-}$ anion may be slightly tilted but will not fall down on the NiO surface. This prevents the strong interaction of its C and F atoms with surface atoms and the breakdown of the $hfac^{-}$ anion on the surface, as our simulation indicates. In this sense, the adsorption of $hfac^{-}$ anion on a NiO surface is stable.

Conversely, on a Ni metallic surface, every Ni surface is equally charged, or charge-neutral if the surface is charge-neutral. Therefore, when an hfacH molecule approaches a metallic Ni surface, there are no particular preferential sites to which it can stably attach and it is less likely to transfer its H atom or H^{+} cation to the surface (i.e., to deprotonate). At room temperature or higher, accidental tilting of an hfacH molecule allows its C and F atoms to be bonded with surface Ni atoms, resulting in dissociation of hfacH on a metallic surface.

These results are qualitatively consistent with experimental observations obtained in earlier studies [1,5,7]. The results of this work indicate that the adsorption of hfacH or other diketones (or even other polarized molecules) on a surface is promoted by the presence of ionic bonds (or polarization) on the surface. On an oxidized or halogenated metal surface, surface atoms are polarized, and approaching diketones may similarly deprotonate and have their O atoms bonded with positively-charged metal atoms on the surface. On a metal surface, however, such polarized molecules cannot find any preferred adsorption sites and may disintegrate when they approach the surface closely.

As discussed earlier, small surface models were employed herein to represent Ni and NiO surface for analysis via first-principles QM simulations. Furthermore, we have not yet tested various DFT functionals with dispersion interactions or basis sets with the diffuse functions. Therefore, the values of adsorption energies and other physical quantities obtained in this study should not be construed to represent the true values of a real system, where the surface size is far greater than the hfacH molecule. A more accurate evaluation of the reaction energies via DFT-based first-principles QM simulations for larger systems will be discussed in the next chapters.

Stable adsorption of hfacH is only the first step of the thermal ALE process of a metal surface. At an elevated surface temperature, adsorbed $hfac^-$ anions on a metal oxide surface form volatile organometallic complexes such as $Ni(hfac)_2$. Analysis of the formation process of such organometallic complexes is also beyond the scope of the present study and is deferred to reported results in chapter 4.

3.5 References

[1] H. L. Nigg and R. I. Masel, J. Vac. Sci. Technol. A, 17, 3477 (1999).

[2] G. O. Hunter and B. D. Leskiw, Rapid Commun. Mass Spectrom., 26, 369 (2012).

[3] Y. Duan, F. Gao, and A. V. Teplyakov, J. Phys. Chem., C 119, 27018 (2015).

[4] S. M. George and Y. Lee, ACS Nano 10, 4889 (2016).

[5] J. K. Chen, T. Kim, N. D. Altieri, E. Chen, and J. P. Chang, J. Vac. Sci. Technol. A 35, 031304 (2017).

[6] J. K. Chen, N. D. Altieri, T. Kim, E. Chen, T. Lill, M. Shen, and J. P. Chang, J. Vac. Sci. & Technol. A 35, 05C305 (2017).

[7] T. Ito, K. Karahashi, and S. Hamaguchi, the 10th EU-Japan JSPP2017, Okinawa, Japan, (2017).

[8] K. J. Kanarik, S. Tan, and R. A. Gottscho, J. Phys. Chem. Lett. 9, 4814 (2018).

[9] J. Zhao, M. Konh, and A. V. Teplyakov, Appl. Surf. Sci. 455, 438 (2018).

[10] M. Konh, C. He, X. Lin, X. Guo, V. Pallem, R. Opila, A. Teplyakov, Z. Wang, and B. Yuan, J. Vac. Sci. Technol. A 37, 021004 (2019).

[11] T. Ito, K. Karahashi, and S. Hamaguchi, in Proceedings of the 39th International Symposium on Dry Process, Tokyo, Japan, 16–17 November 2017, edited by K. Kinoshita et al. (DPS Organizing Committee, 2017), Vol. E-4, p. 45.

[12] M. J. Frisch, G. W. Trucks, H. B. Schlegel, G. E. Scuseria, M. A. Robb, J. R. Cheeseman, G. Scalmani, V. Barone, B. Mennucci, G. A. Petersson, H. Nakatsuji, M. Caricato, X. Li, H. P. Hratchian, A. F. Izmaylov, J. Bloino, G. Zheng, J. L. Sonnenberg, M. Hada, M. Ehara, K. Toyota, R. Fukuda, J. Hasegawa, M. Ishida, T. Nakajima, Y. Honda, O. Kitao, H. Nakai, T. Vreven, J. A. Montgomery, J. E. Peralta, F. Ogliaro, M.

Bearpark, J. J. Heyd, E. Brothers, K. N. Kudin, V. N. Staroverov, T. Keith, R. Kobayashi, J. Normand, K. Raghavachari, A. Rendell, J. C. Burant, S. S. Iyengar, J. Tomasi, M. Cossi, N. Rega, J. M. Millam, M. Klene, J. E. Knox, J. B. Cross, V. Bakken, C. Adamo, J. Jaramillo, R. Gomperts, R. E. Stratmann, O. Yazyev, A. J. Austin, R. Cammi, C. Pomelli, J. W. Ochterski, R. L. Martin, K. Morokuma, V. G. Zakrzewski, G. A. Voth, P. Salvador, J. J. Dannenberg, S. Dapprich, A. D. Daniels, O. Farkas, J. B. Foresman, J. V. Ortiz, J. Cioslowski, and D. J. Fox, Gaussian, Inc., Wallingford CT (2010).

[13] S. Grimme, J. Chem. Phys. 124, 034108 (2006).

[14] M. Steinmetz and S. Grimme, ChemistryOpen, 2, 115 (2013).

[15] S. Paranthaman, S. Sampathkumar, and N. K. Murugasenapathi, J. Chem. Sci. 130, 164 (2018).

[16] R. Krishnan, J. S. Binkley, R. Seeger, and J. A. Pople, J. Chem. Phys. 72, 650 (1980).

[17] M. C. Holthausen, J Comp. Chem. 26, 1505 (2005).

[18] R. Valero, J. R. B. Gomes, D. G. Truhlar, and F. Illas, J. Chem. Phys. 132, 104701 (2010).

[19] X. Xu and D. G. Truhlar, J. Chem. Theory Comput. 8, 80 (2012).

[20] Y. Sert, F. Ucun, G. A. El-Hiti, K. Smith, and A. S. Hegazy, J. Spectro. 2016, 5396439 (2016).

[21] M. da Silva, L. Santos, and E. Giera, J. Chem. Thermodynamics 39, 361 (2007).

[22] K. Manbeck, N. Boaz, N. Bair, A. Sanders, and A. Marsh, J. Chem. Educ. 88, 1444 (2011).

[23] S. Engmann, B. Ómarsson, M. Lacko, M. Stano, Š. Matejcík, and O. Ingólfsson, J. Chem. Phys. 138, 234309 (2013).

[24] D. L. Howard, H. G. Kjaergaard, J. Huang, and M. Meuwly, J. Phis. Chem. A 119, 7980 (2015).

[25] H. Kung and A. Teplyakov, J. Catalysis 330, 145 (2015).

CHAPTER 4:

Formation and Desorption of Nickel Hexafluoroacetylacetonate Ni(hfac)$_2$ on a Nickel Oxide Surface in Atomic Layer Etching (ALE) Processes*

---

* Abdulrahman H. Basher, M. Krstić, F. Karin, T. Ito, K. Karahashi, W. Wenzel, and S. Hamaguchi, "Formation and desorption of nickel hexafluoroacetylacetonate Ni(hfac)$_2$ on a NiO surface in ALE processes," J. Vac. Sci. Technol. A, (*in press* 2020). https://doi.org/10.1116/6.0000293

4.1 Introduction

In the last chapter, we could show that an enol hexafluoroacetylacetone (hfacH) molecule is deprotonated and interacted stably with a NiO surface as a hexafluoroacetyl-acetonate anion ($hfac^-$) unlike when it interacted with a Ni surface [1]. However, we could not show if there is a barrier and transition energy between the two states, i.e., from hfacH to $hfac^-$, on a NiO surface. The formation of a nickel hexafluoroacetylacetonate $Ni(hfac)_2$ complex and its desorption could not be shown, i.e., the primary yield in thermal ALE processes as illustrated in the first chapter, since the two negatively-charged O atoms of $hfac^-$ are bonded strongly with two of the positively-charged surface Ni atoms. Besides simple monolayers NiO surface model was used to minimize the computational complexity, various DFT functionals with dispersion corrections as well as basis sets with the diffuse functions were not tested. Therefore, we decided to investigate the mechanism of the interaction of hfacH molecules with a more realistic NiO surface model.

In this chapter, focusing on thermal ALE of metallic Ni by oxidation and hfacH exposure, we have examined the surface reaction mechanisms of an oxidized Ni surface exposed to gaseous hfacH molecules, using TURBOMOLE [2] as a first-principles quantum mechanical (QM) calculations program.

The first goal of this chapter is, therefore, to re-evaluate the previously reported values of reaction energies of hfacH adsorption on a NiO surface with more realistic multi-layer surface material models. The second goal is to understand the mechanisms of the formation of nickel hexafluoroacetylacetonate $Ni(hfac)_2$ complexes on a NiO surface and their desorption.

The formation of $Ni(hfac)_2$ complex on a NiO surface and its desorption is discussed in this chapter.

4.2 Methodology

All QM calculations in this chapter were performed with TURBOMOLE V7.3.1 [2] software based on a DFT method with Gaussian type atomic orbitals. As in Refs. [3] and [4], where ZnO surfaces were modeled with the embedded cluster method (ECM) [3,4], we constructed a multi-layer material model representing crystalline NiO with its (100) surface, using the ECM. Figure 4-1 shows the entire model system (which we call the ECM model) representing a NiO material used in this chapter. Here the colored spheres represent atoms in our DFT calculations, whereas the colored dots represent point charges that provide the electrostatic field to the DFT calculation region.

To reduce the computational load without much affecting the physical processes of adsorption, we replaced Ni atoms of lower and outermost layers with Mg atoms while keeping Ni atoms on the top surface that can directly interact with adsorbing molecules. This is because Mg has fewer electrons than Ni while Ni and Mg have similar valence electron structures and both NiO and MgO have the halite (i.e., rock salt or NaCl) structure with similar lattice constants [5,6].

In Figure 4-1, the gray, red, and green spheres represent Ni, O, and Mg atoms, respectively, and small blue and red dots represent positive ($+2e$) and negative ($-2e$) point charges (PCs) with e being the elementary charge. We used a model of NiO, which has the halite (cubic) structure with a lattice constant of 4.19 Å taken from Materials Project [7], which was obtained by using the PBE functional. The PBE lattice constant is in good

agreement with those obtained by using pseudopotential [8] and all-electron [9] calculations with PBE as well as the experimental results[10]. The dimensions of the rectangular cube shown in Fig. 4-1 are 29.33 × 29.33 × 18.86 $Å^3$ and the top surface represents a (100) surface. In this ECM model, we call the region where atoms are represented by spheres in Fig. 4-1 the QM region, and the rest the embedding region. In the QM region, all atoms except for those in the outermost layer are treated quantum mechanically during DFT calculations, as will be explained more in detail momentarily.

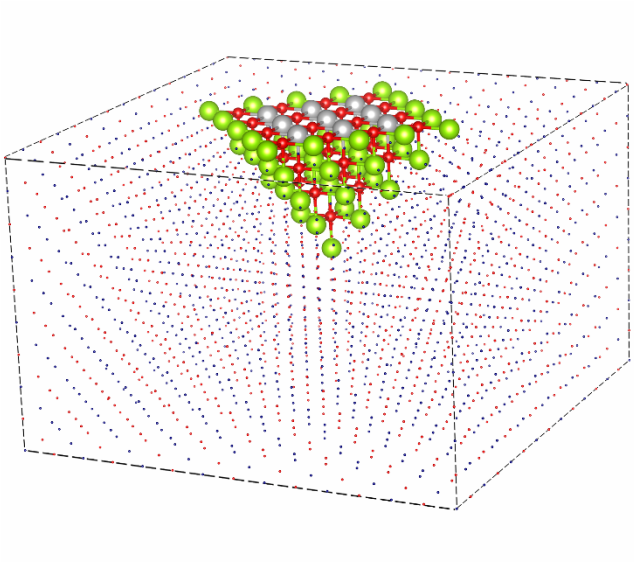


Fig. 4-1: Atomic configurations of the NiO four shell surface material model used in our DFT calculations. All atoms are in the lattice sites of the rectangular NiO crystalline structure with a dimension of 29.33 × 29.33 × 18.86 $Å^3$, having a (100) top surface. It consists of the QM region, represented by the collection of gray, red, and green spheres located near the center of the top surface and the embedding region represented by the blue and red dots occupying the NiO lattice sites outside the QM region. All calculations were performed for this rectangular box in the presence of the embedding region with different models of the QM region. Here, gray, red, and green spheres represent Ni, O, and Mg atoms, respectively, and blue and red dots represent PCs. For details, the reader is referred to the main text.

In this chapter, adsorbed hfacH molecules are set to interact only with the NiO top surface of this model, keeping sufficient distance from surrounding Mg atoms, so we believe that interaction of hfacH with a NiO (100) surface can be well represented with this model material.

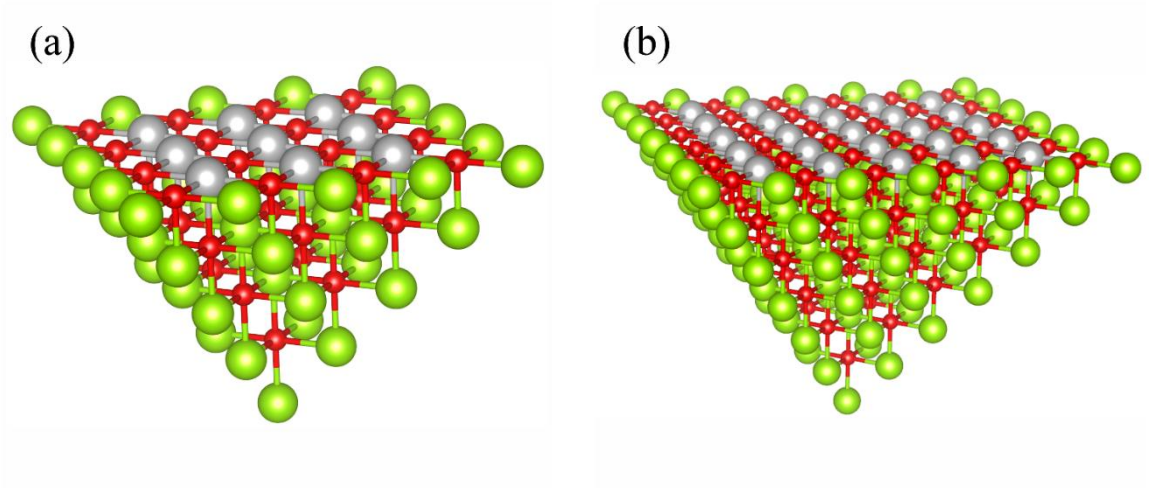


Fig. 4-2: Optimized structures of the (a) "four shell model" and (b) "six shell model" of the QM region having a NiO (100) surface, whose arrangement of atoms is given in Table I.

Figure 4-2(a) shows the QM region of Fig. 4-1. This region was formed in the following manner: First, we placed a single Ni atom. This atom corresponds to the one located at the center of the top surface of Fig. 2(a). Note that, if this Ni atom were in the bulk, six O atoms should occupy the first octahedral shell surrounding it. Second, to create a NiO (100) surface with this Ni atom being in the center, we placed five O atoms (excluding the O atom just above the Ni atom) in the octahedral shell around the Ni atom, with four of them together with the Ni atom forming a plane [the (100) surface] and another O atom being just below the Ni atom, as seen in Fig. 4-2(a). These five O atoms form the

first shell of the model material. We then placed 13 metal atoms in the second shell surrounding the first shell, excluding the region above the (100) surface. Among the 13 metal atoms, eight of them occupying the same (100) surface were Ni atoms and the other five (below the top surface) were Mg atoms. Similarly, we formed the third shell consisting of 25 O atoms. In the fourth shell, all 41 metal atoms on or below the (100) surface were Mg atoms. As seen in Fig. 4-2(a), the outermost edge of the flat (100) surface in the QM region consists of 16 Mg atoms. We call this model material the NiO four shell model. The shell structures and the number of atoms in each shell are summarized in Table 4-1.

As seen in Fig. 4-1, in the embedding region, the positive and negative PCs occupy the lattice sites of Ni and O atoms. The total number of PCs in this model is 2165. Our DFT calculations were performed for atoms in the QM region with the electric field produced by the immobile PCs (i.e., the positions of all PCs were fixed during the calculations) to include the influence of far ionic atoms of the bulk material. In what follows, all DFT calculations are performed in the presence of the PC electric field even when the figure shows only the QM region without PCs.

For some calculations, we used an extended shell model, as shown in Fig. 4-2(b). It is in the shape of an inverse square pyramid (i.e., the bottom half of an octahedron) similar to Fig. 4-2(a) with additional O and Mg shells. The outermost shell is the sixth shell that consists only of Mg atoms. We call this model system the NiO six shell model. The number of atoms in each shell is also summarized in Table 4-1. It consists of 25 Ni atoms on the top (100) surface. The QM region of the NiO six shell model is embedded in the same NiO rectangular box of Fig. 4-1, which makes the number of PCs 2019.

No periodic boundary condition is imposed on the surface material model in this chapter. The embedding region has no global dipole moment arising from the PCs because each plane boundary surface of the rectangular box consists of the same number of positive and negative charges, i.e., carries no net charge. Therefore, unlike the ECM of ZnO in Refs. [3] and [4], no counter charge needs to be added to this system.

TABLE 4-1: Information on atomic configurations in the QM regions of two NiO surface material models used in this study. In the "Coordinates" column, "Fixed" indicates that the atoms listed in the same row are set immobile during structural optimization.

	QM region		Numbers	Coordinates
Four Shell Model	Central	Ni	1	
	1st shell	O	5	
	2nd shell	Ni, Mg	8 , 5	Fixed
	3rd shell	O	25	
	4th shell	Mg	41	Fixed and treated as ECP
	PCs		2165	Fixed
Six Shell Model	Central	Ni	1	
	1st shell	O	5	
	2nd shell	Ni, Mg	8, 5	Fixed
	3rd shell	O	25	
	4th shell	Ni, Mg	16, 25	Fixed
	5th shell	O	61	
	6th shell	Mg	85	Fixed and treated as ECP
	PCs		2019	Fixed

In our DFT calculations, we employed generalized gradient approximation (GGA) PBE functionals [11-14]. As to the basis sets, we employed def2-SVP [15] for Ni and Mg atoms, except for Mg atoms in the outermost shell, and def2-TZVP [16] for all O atoms of the surface material model as well as all atoms of hfacH. Furthermore, the Grimme's D3 dispersion corrections [17,18] with Becke-Johnson (BJ) [19] damping were used to represent London dispersion forces (or what are loosely called van der Waals forces).

Each Mg atom in the outermost shell was approximated by the effective core potential (ECP) of ecp-10-sdf [20] as well as -2*e* fixed charge and served as an additional embedding potential to prevent leakage of the electron density of the negatively charged O atoms. In other words, the Mg atoms in the outermost shell of the QM region were not evaluated quantum-mechanically.

All geometries were fully optimized using gradient minimization techniques with the Resolution of the Identity approximation for the Coulomb energy (RI-J) [21,22] and multipole accelerated RI-J (MARIJ) [23] option as implemented in TURBOMOLE 7.3.1 code [2]. The structural optimization of the QM region of the surface material model was performed in the following manner: The positions of all Mg atoms and PCs were set immobile and the positions of all Ni and O atoms were optimized to achieve the lowest total energy of the system. The QM regions are given in Fig. 4-2(a) and (b) are depicted after converged structural optimizations.

As a model of a non-smooth or “rough” surface, we placed single Ni and O atoms just above the surface O and Ni atoms and performed the structural optimization, as shown in Fig. 4-3(a). Here, the added O atom was placed above the Ni atom at the center of the

surface area and the added Ni atom was placed above one of the surface O atoms in the first shell.

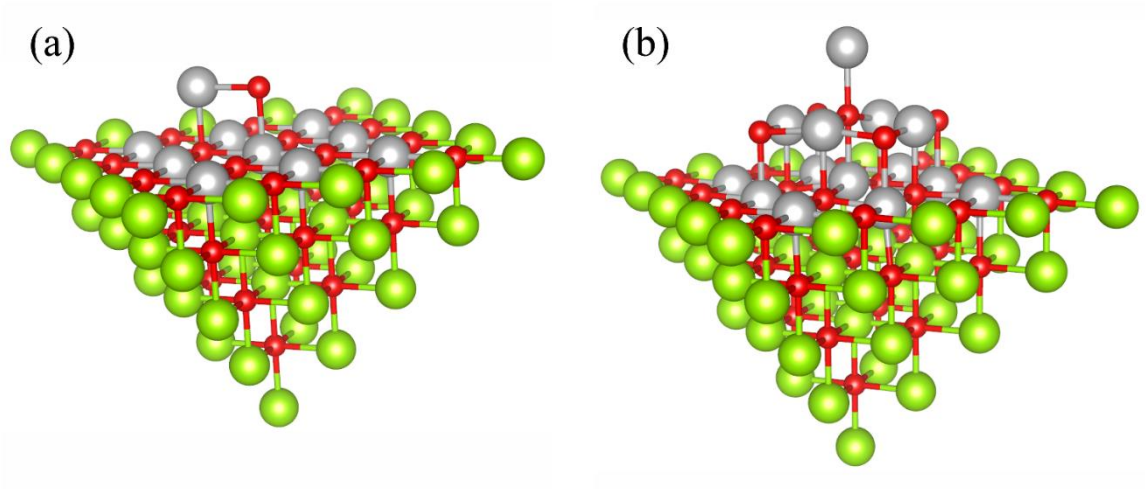


Fig. 4-3: Optimized structures of rough surface models with (a) Ni and O atoms added to the surface of the four shell model and (b) 5 Ni and 5 O atoms arranged in a pyramid-like structure added to the four shell model.

Another model of a rough surface was formed with five additional NiO units stacked on the NiO surface, as shown in Fig. 4-3(b). Here the NiO structure was formed by extending the first and third octahedral shells of O atoms up to the first monolayer above the original (100) surface of Fig. 4-2(a) and completing the second octahedral shell of Ni atoms above the (100) surface. Figure 4-3(b) shows this rough surface model after the DFT structural optimization.

As to an hfacH molecule, the enol form is known to be more stable than the keto form [1,21-28]. Therefore, we only use the enol form of hfacH, as shown in Fig. 4-4. Here, dark gray, blue, and white spheres represent carbon (C), fluorine (F), and hydrogen (H) atoms, respectively.

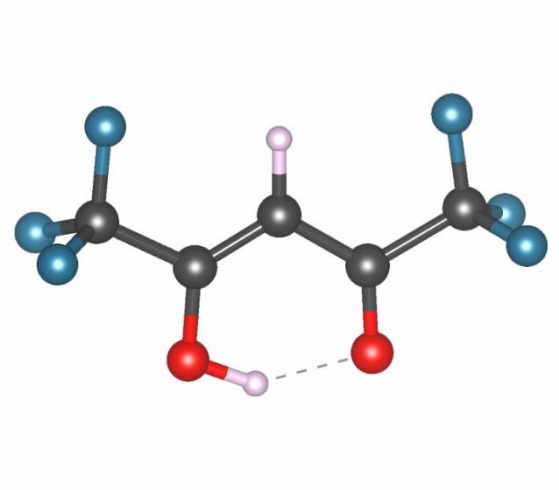


Fig. 4-4: Optimized structure of an enol-type hfacH molecule. Here, dark gray, red, blue, and white spheres represent C, O, F, and H atoms, respectively.

4.3 Results and discussion

First, we evaluate the reaction energy of hfacH adsorption on a NiO surface. The reaction energy of a surface-molecule interaction is defined in general as

$$\text{Reaction energy} = E_{\text{total}} - E_{\text{ad}} - E_{\text{surf}}, \qquad (4.1)$$

where E_{total} is the total energy of the system with (a) molecule(s) adsorbed on a NiO model surface, E_{ad} is the total energy of the molecule(s) prior to the interaction, and E_{surf} is the total energy of the surface material model prior to the interaction, all after the structural optimization.

We studied the adsorption of an hfacH molecule on the model surface of Fig. 2(a) by placing an hfacH molecule at various positions just above the model surface near its center and performing the structural optimization of the entire system. The structural optimization was performed with the positions of all Mg and PCs being fixed, as described in the previous section. Prior to the structural optimization, the hfacH molecule was placed

vertically to the surface with its two O atoms closest to the surface. The two O atoms were positioned at equal distances from the (100) surface.

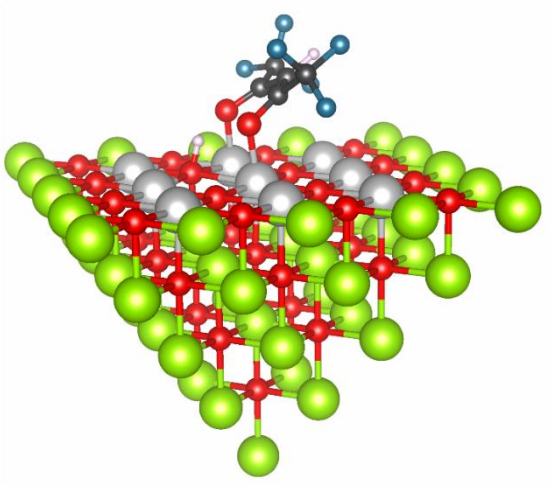


Fig. 4-5: Optimized structure of the four shell model for a NiO (100) surface with an adsorbed hfacH molecule after deprotonation.

Upon obtaining converged calculation, we observed that the hfacH molecule was deprotonated by transferring its H atom to one of the surface O atoms in a barrierless process, which is in agreement with the results in chapter 3 that is reported in Ref. [1]. Among various adsorption sites examined in this study, the most stable configuration of an hfacH adsorbed surface is shown in Fig. 4-5, where an $hfac^-$ anion is found to be stabilized with its two O atoms being bonded with two adjacent Ni atoms of the top surface. The reaction energy of this adsorption process was found to be -2.26 eV. The reaction energy of the same adsorption process evaluated with the six shell model of Fig. 2(b) was found to be -2.08 eV. The same calculations were also performed with two other exchange-correlation functionals, namely, PBE0 [29], and B3LYP [30-35] and the same basis sets, including or excluding dispersion corrections D3 with BJ damping, for the four shell model of Fig. 4-2(a). These results are summarized in Table 4-2. In Fig. 4-5, the tilted angle of

the hexafluoroacetylacetonate (hfac) group measured from the normal direction of (100) surface is 52°. The Mulliken charge distribution of Fig. 4-5 is shown in Fig. 4-6. which shows that the positively charged O atoms of the deprotonated hfacH are bonded with positively charged Ni atoms on the surface, as discussed in the earlier study [1].

Although a hybrid exchange-correlation functional B3LYP is considered more accurate in evaluating valence orbitals of transitions metals and their oxides [31,33-35], it typically requires much more computational time than PBE, whereas, as seen in Table 4-2, the calculated energies by all three functionals are within a relative deviation of 10%. Therefore, in this chapter, we use PBE for our DFT calculations unless otherwise indicated. Since our goal is not to pursue a highly accurate energy evaluation, we are content with a single decimal approximation to the energy level (in eV units) obtained in this chapter. However, we keep up to two decimal places of all energy values obtained from our calculations in this manuscript for the reader who may be interested in reproducing our results with the same computational method.

TABLE 4-2: Reaction energies of Fig. 4-5 for the adsorption of a single hfacH on a NiO (100) surface, evaluated with different functionals and assumptions of the dispersion effects.

Functionals	PBE	PBE0	B3LYP
with D3-BJ	-2.26 eV	-2.36 eV	-2.45 eV
without D3-BJ	-1.55 eV	-1.59 eV	-1.47 eV

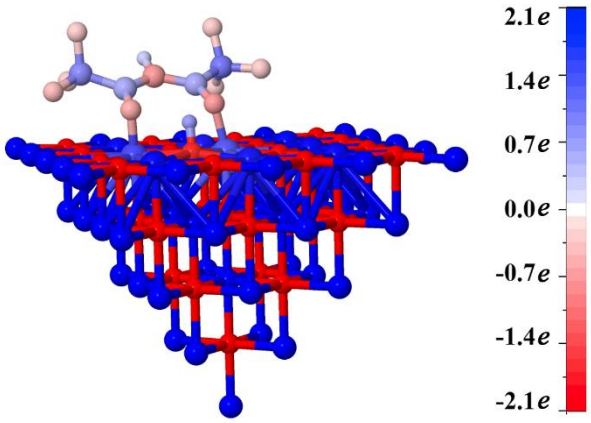


Fig. 4-6: Mulliken partial charge distribution state of Fig. 4-5.

As seen in Table II, the calculated reaction energies without dispersion correction D3 / BJ damping are much lower in magnitude than those with the dispersion correction. This clearly shows that dispersion energy accounts for a significant part (~ 1 eV) of the total energy for the stable absorption of deprotonated hfacH (i.e., $hfac^{-}$) and the proton H^{+} on the NiO surface. The reaction energy obtained here is in reasonable agreement with what was reported in the last chapter and Ref. [1].

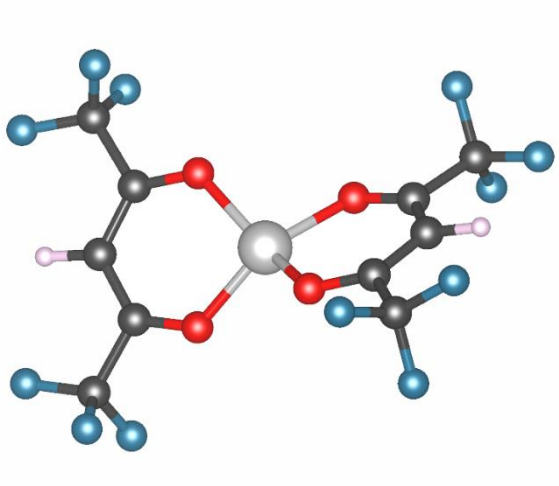


Fig. 4-7: Optimized structure of a $Ni(hfac)_2$ complex. Here, dark gray, red, blue, and white spheres represent Ni, O, F, and H atoms, respectively.

Second, we examined the formation process of volatile organometallic complex $Ni(hfac)_2$ on a NiO surface. The optimized structure of a $Ni(hfac)_2$ complex is shown in Fig. 4-7. For this complex to be formed, two hfac groups need to bond with a single Ni atom. Therefore, we placed another hfacH molecule near the bonding site of the hfac group of Fig. 4-5 and performed the structural optimization of the system, which led to the atomic configuration shown in Fig. 4-8. The structural optimization showed that the second hfacH molecule deprotonated but two hfac groups did not bond with a single Ni atom on the surface. The reaction energy for the adsorption of these two hfacH molecules was found to be -4.20 eV. (It was found to be -4.73 eV when the B3LYP functional and same basis sets were used.) The tilting angles of the left and right hfac groups in Fig. 4-8 are 29° and 56°.

Despite an extensive search for an optimal position of the second hfacH molecule that could form a $Ni(hfac)_2$ like structure, we were unable to find a stable configuration where two hfac groups bonded to a single Ni atom of the flat surface. This suggests that the formation of $Ni(hfac)_2$ is unlikely to occur on the flat (100) NiO surface. The atomic configuration of Fig. 4-8 suggests that a geometrical interference of two hfac groups prevents them from bonding to a single Ni atom on the surface.

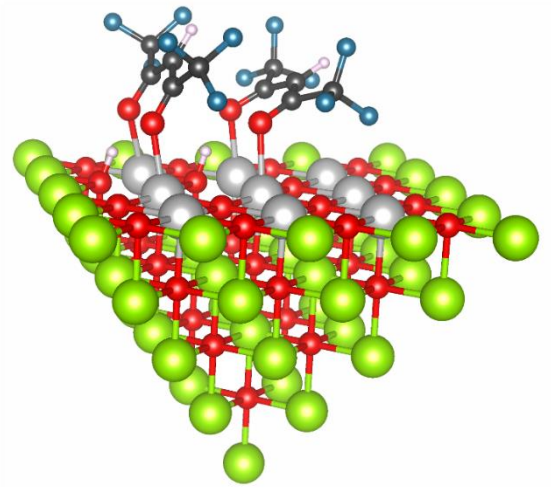


Fig. 4-8: Optimized structure of the four shell model for a NiO (100) surface with two adsorbed hfacH molecules after deprotonation.

Rough surfaces such as those of Fig. 4-3(a) and (b) may allow two hfac groups to bond to a single Ni atom protruding from the surface without much geometrical interference. By performing the structural optimization after placing two hfacH molecules near the protruding Ni atom of Fig. 4-3(b), we found both hfacH molecules deprotonated and three O atoms of the two hfac groups clearly bonded to the Ni atom, as seen in Fig. 4-8(a). The reaction energy for this adsorption process for the two hfacH molecules was found to be -4.60 eV. Similarly, the structural optimization of two hfacH molecules placed near the topmost Ni atom of Fig. 4-3(b) led to the atomic configuration shown in Fig. 4-8(b), where a $Ni(hfac)_2$ – like structure is clearly seen to be formed, although its Ni atom is still bonded with an O atom of the surface. Its reaction energy was found to be -5.41 eV.

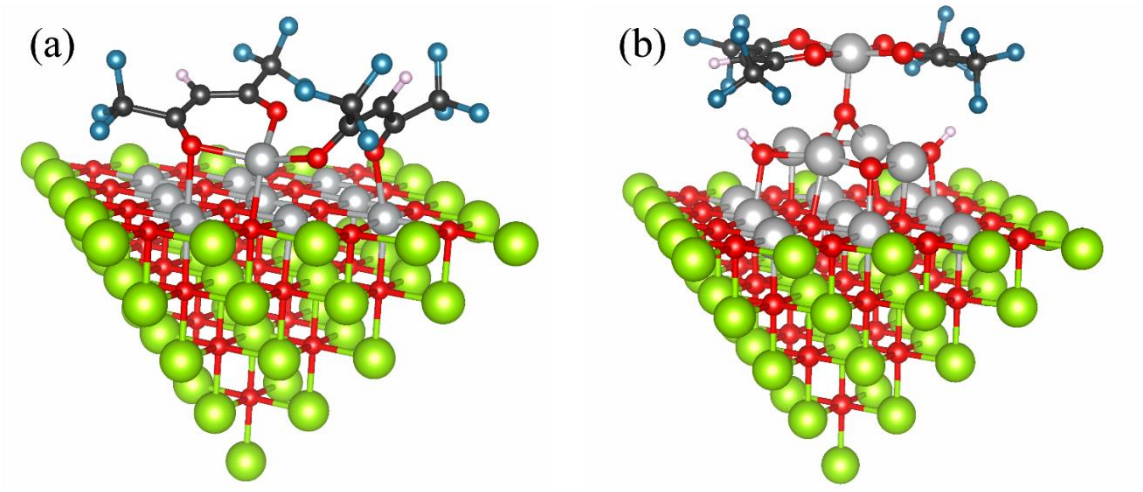


Fig. 4-9: Optimized structures of the rough surface models of (a) Figs. 4-3 (a) and 4-3 (b) with two adsorbed hfacH molecules after deprotonation. In each surface, a $Ni(hfac)_2$-like structure is formed around the topmost Ni atom.

The minimum energy required to desorb a $Ni(hfac)_2$ complex and a water molecule H_2O from each atomic configuration of Fig. 4-9 was also evaluated. Figure 4-10 shows

how the system energy changes if the Ni atom bonded with two hfac groups is detached from the surface in the vertical direction, where the black and red curves show the cases of Fig. 4-9(a) and (b). The abscissa represents the distance of the Ni atom measured from its original position given in Fig. 4-9. The ordinate represents the change in the system energy. In this approach, only the Ni atom in the center, surrounded by the two hfac groups, was moved stepwise vertically in the upward direction, and then the structural optimization was performed for the rest of the atoms, including those of hfac groups. (In the surface material model, all Mg atoms and PCs were immobile during the optimization, as stated before). It is seen that the system energy increases monotonically until $Ni(hfac)_2$ desorbs completely from the surface. (Note that the H atoms are still on the surface.) The energy required for the complete isolation of $Ni(hfac)_2$ from the surface is the desorption energy, which is 3.81 eV for the system of Fig. 4-9(a) and 2.97 eV for the system in Fig. 4-9(b).

Figure 4-11 depicts the difference in system energy among each atomic configuration when the rough surface of Fig. 4-3(a) is exposed to two hfacH molecules. The total energy prior to adsorption is set to be zero (a). As given in Fig. 4-9(a), the adsorption energy for two hfacH molecules on the surface is -4.60 eV (b). After both an organometallic complex $Ni(hfac)_2$ and a water molecule H_2O desorb from the surface, as illustrated in (c), the system energy becomes -1.68 eV, which makes the energy difference between the adsorbed and desorbed states 2.93 eV. As discussed earlier, the structural optimization was performed for all atomic configurations shown in Fig. 4-11.

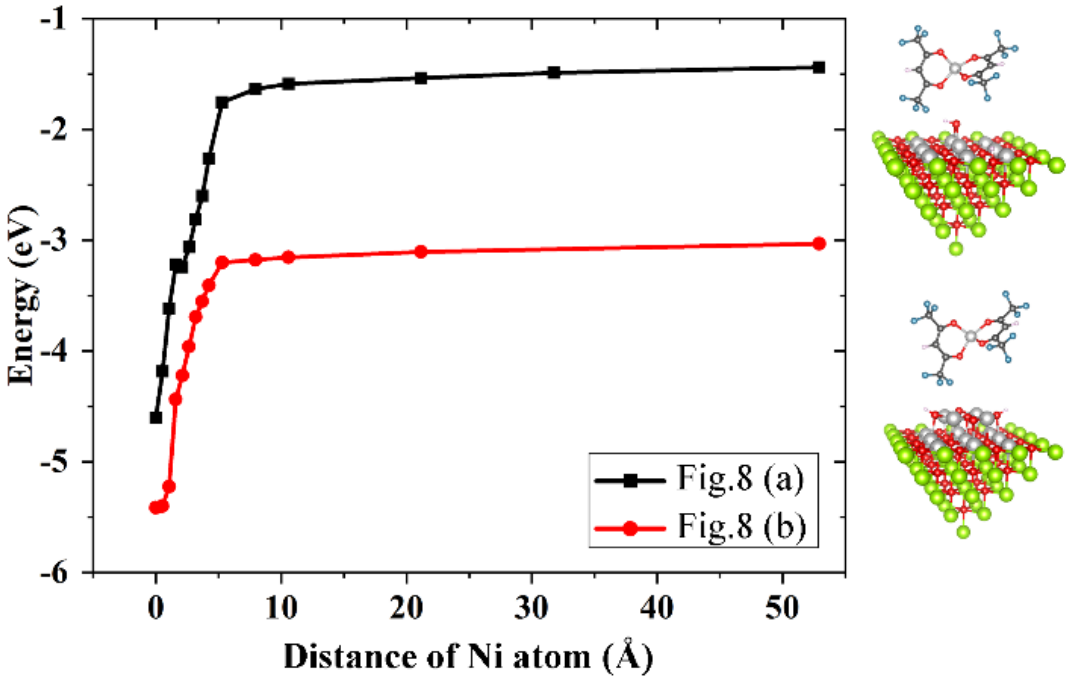


Fig. 4-10: System energy as a function of the position of the topmost Ni when two hfacH molecules are adsorbed around the protruding Ni atom of a rough surface. The black and red curves represent the cases of Figs. 4-9 (a) and 4-9 (b). The abscissa represents the distance of the Ni atom measured from its initial position given in Fig. 4-9 in each case. The ordinate represents the change in energy measured from the initial system energy prior to adsorption, i.e., the total energy of the system consisting of the surface material model of Fig. 4-3 and two hfacH molecules of Fig. 4-4 away from the surface.

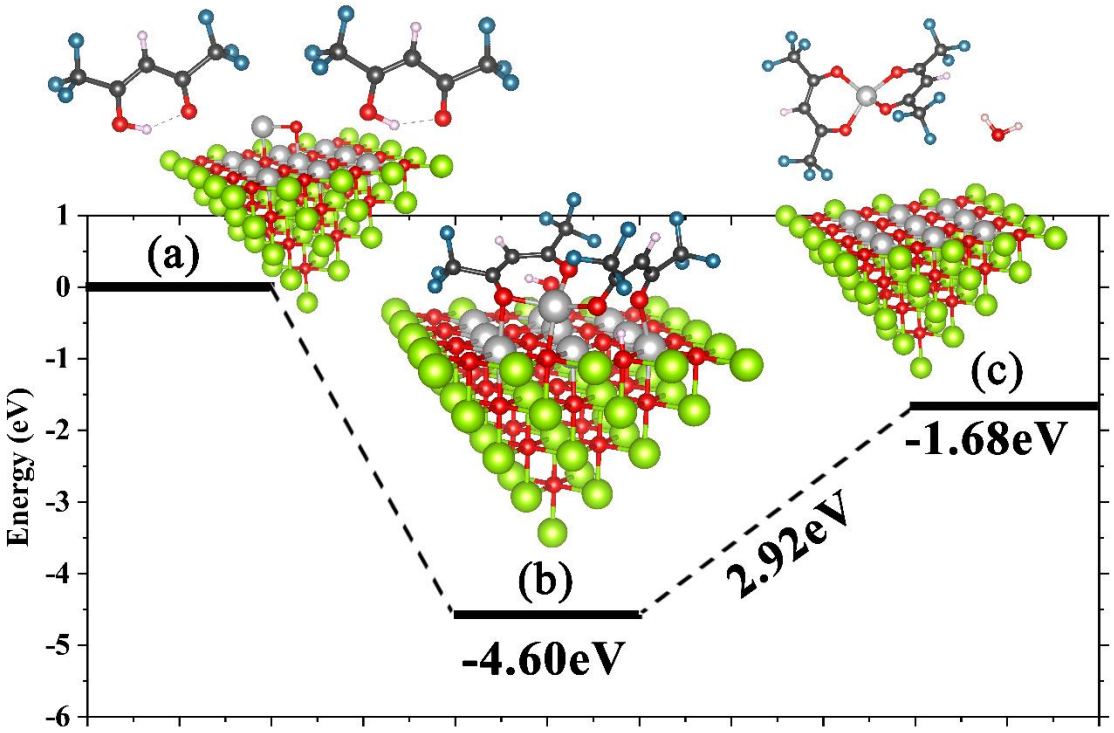


Fig. 4-11: System energies of different states of atomic configurations. The initial state prior to the adsorption of two hfacH molecules on the rough surface of Fig. 4-3 (a) is depicted in (a), where the system energy is set to be zero. The state of two hfacH molecules adsorbed on the surface [i.e., Fig. 4-9 (a)] is shown in (b). The final state where both an H_2O molecule and a $Ni(hfac)_2$ complex have desorbed from the surface is depicted in (c). The structural optimization among all Ni, O, C, F, and H atoms was performed for each state.

Similarly Fig. 4-12 depicts the difference in system energy among each atomic configuration when the rough surface of Fig. 4-3(b) is exposed to two hfacH molecules. The total energy prior to adsorption is set to be zero (a), as in Fig. 4-11. As given in Fig. 4-9(b), the adsorption energy of two hfacH molecules on the surface was -5.41 eV (b). After a water molecule desorbs from the surface, as illustrated in (c), the system energy becomes -3.95 eV. After both an organometallic complex $Ni(hfac)_2$ and a water molecule

H_2O desorb from the surface, as illustrated in (d), the system energy becomes -2.19 eV. Although we have not evaluated the activation energy from one state to another, the energy diagram of Fig. 4-12 suggests that such stepwise desorption may take place at an elevated surface temperature. The energy diagram of Fig. 4-11 including a similar H_2O desorption state is shown in Fig. 4-13.

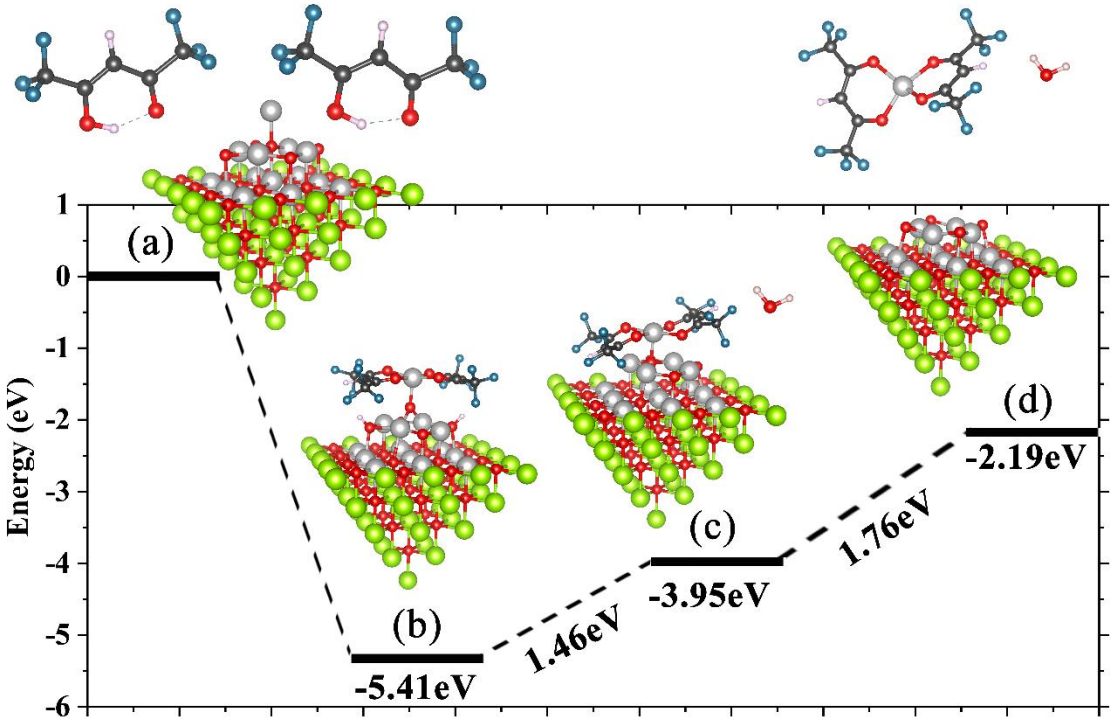


Fig. 4-12: System energies of different states of atomic configurations. The initial state prior to the adsorption of two hfacH molecules on the rough surface of Fig. 4-3(b) is depicted in (a), where the system energy is set to be zero. The state of two hfacH molecules adsorbed on the surface [i.e., Fig. 4-9 (b)] is shown in (b). The state of H_2O molecule desorption from (b) while two hfac groups remain adsorbed on the surface is presented in (c). The final state where both an H_2O molecule and a $Ni(hfac)_2$ complex desorbed from the surface is depicted in (d). The structural optimization among all Ni, O, C, F, and H atoms was performed for each state.

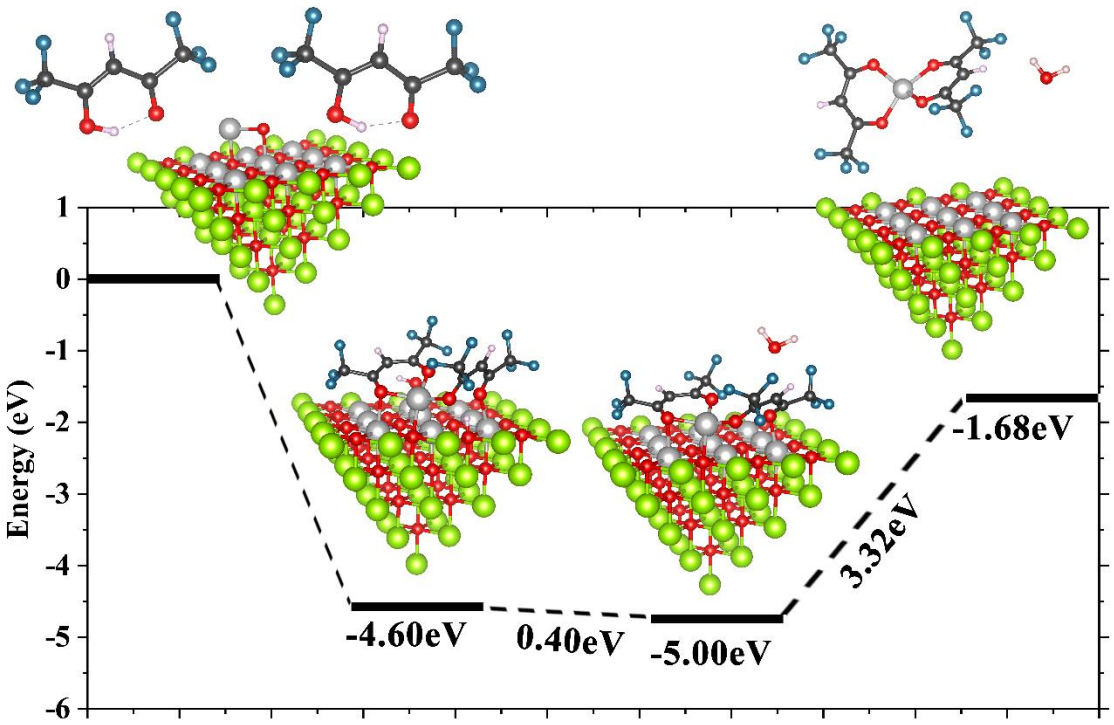


Fig. 4-13: The energy diagram of Fig. 4-11 including a similar H_2O desorption state.

To demonstrate the difficulty of removing Ni and O atoms from the flat (100) surface, we also present the energy diagram in Fig. 4-14 for the case of Fig. 4-8. The total energy prior to adsorption is set to be zero (a), as in the previous figures. As discussed earlier, the adsorption energy for two hfacH molecules on the Ni (100) surface is -4.20 eV (b). Although we have stated that the formation of $Ni(hfac)_2$ on this surface is very unlikely, we can evaluate the energy levels of desorbed states. The energy levels of desorption of an H_2O molecule only (c) and both desorption and both $Ni(hfac)_2$ and H_2O (d) are -2.11 eV and 7.89 eV. Since we have not evaluated the activation energies for such desorption processes, it is not clear how likely desorption depicted in (c) or (d) takes place from the adsorbed state of (b). However, even without the consideration of activation energy, this energy diagram indicates that the direct transition from the adsorbed state (b) or (d) to the

formation and desorption of $Ni(hfac)_2$ on the flat surface is very unlikely even at an elevated surface temperature of 300 ~ 400 °C.

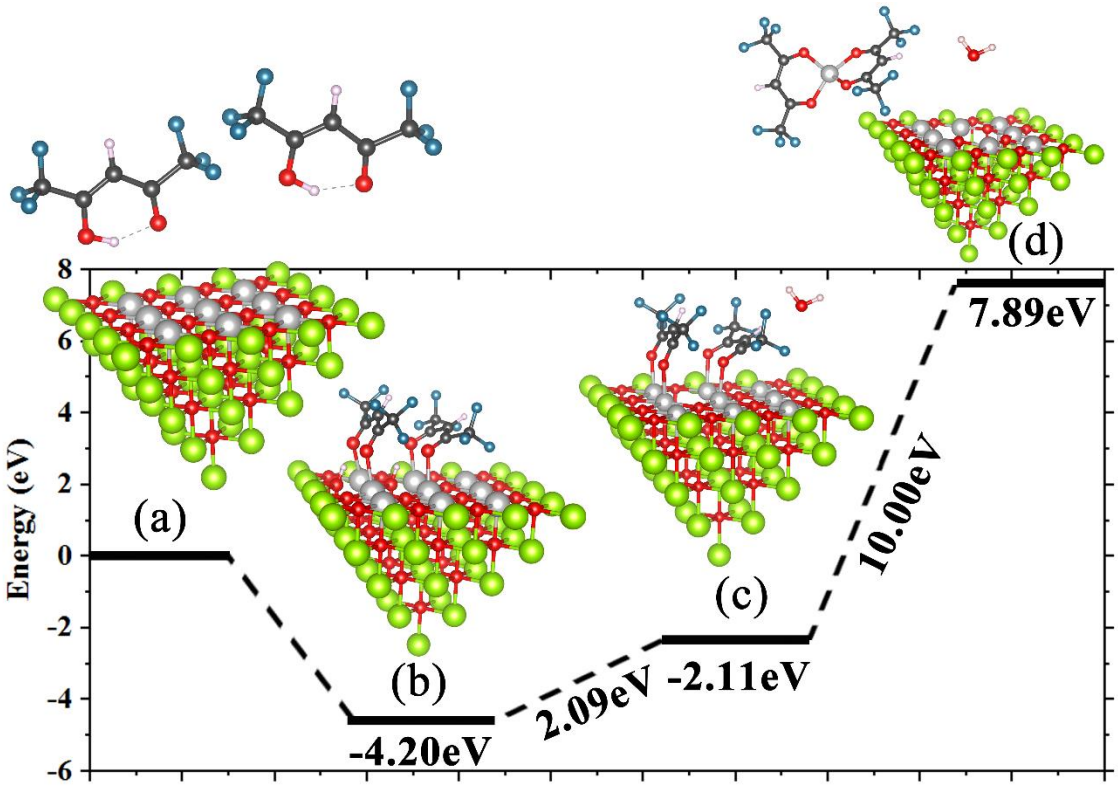


Fig. 4-14: System energies of different states of atomic configurations. The initial state prior to the adsorption of two hfacH molecules on the Ni (100) surface of Fig. 4-2(a) is depicted in (a), where the system energy is set to be zero. The state of two hfacH molecules adsorbed on the surface [i.e., Fig. 4-8] is shown in (b). The state of H_2O molecule desorption from (b) while two hfac groups remain adsorbed on the surface is presented in (c). The final state where both an H_2O molecule and a $Ni(hfac)_2$ complex desorbed from the surface is depicted in (d). The structural optimization among all Ni, O, C, F, and H atoms was performed for each state.

4.4 Summary

We have examined stable adsorption of hfacH molecules on a NiO (100) surface and possible formation of volatile organo-nickel complexes $Ni(hfac)_2$ and water molecules H_2O from the surface at elevated surface temperature, using DFT calculations. This chapter uses a more realistic extended NiO surface model larger than the model surface used in the chapter 3 and Ref. [1]. We have confirmed in the new calculations that, when an hfacH molecule approaches a NiO (100) surface, it deprotonates barrierlessly and the negatively charged O atoms of the deprotonated $hfac^-$ anion bond with positively charged Ni atoms of the surface. The nature of ionic bonds (i.e., the charge distribution) of a metal oxide surface promotes the deprotonation and adsorption of hfacH molecules. The adsorption mechanism and adsorption energy of an hfacH molecule on a NiO (100) surface obtained in this chapter are consistent with what was reported in Ref. [1].

We have also examined how two hfacH molecules adsorbed on a NiO surface can form a $Ni(hfac)_2$ complex at an elevated surface temperature. On a flat NiO (100) surface, two hfacH molecules can deprotonate and adsorb barrierlessly. However, we were unable to find a (meta)stable configuration where two hfac groups bonded to a single Ni atom of the NiO surface. It seems such a configuration is unstable and two hfac groups tend to bond with different Ni atoms on the surface. This indicates that the formation of a $Ni(hfac)_2$ complex on the flat surface is very unlikely.

In the case of a rough NiO surface, some Ni atoms may protrude over their surrounding atoms and allow two hfac groups to bond to a single Ni atom without much geometrical interference. Models of rough NiO surfaces examined in this chapter are those given in Fig. 4-3(a) and (b). In each case, the topmost Ni atom is under-coordinated and

has enough space around it to capture two hfac groups stably after both hfacH molecules deprotonated, as shown in Fig. 4-9. In other words, our DFT calculations have demonstrated that roughness of a NiO surface can promote the formation of organo-nickel complexes $Ni(hfac)_2$ on its surface. In earlier experiments [36-37], volatile $Ni(hfac)_2$ and H_2O desorb from the surface at a temperature of around 300 °C or higher. In the case of Fig. 4-12, the required energy for the complete desorption to occur from the adsorbed state is less than 2.0 eV in each step. A more quantitative study on the relation between the energy diagrams of Figs. 4-12, 4-13, and 4-14 and experimental observation is the subject of a future study.

Our study indicates that, in a thermal ALE process of metal consisting of an oxidation step and a removal step aided by the formation of volatile organometallic complexes, the surface roughness incidentally caused by the oxidation step may play a critical role in enhancing the thermal desorption rate of organometallic complexes in the subsequent removal step. If protruding metal atoms are preferentially removed from the surface in the desorption step, the surface roughness decreases and so may the desorption rate. In other words, thermal ALE of this type for a rough metal surface tends to increase its smoothness. This is consistent with experimental observations of surface smoothing in a similar thermal ALE process of cobalt (Co) consisting of surface chlorination steps and removal steps of the chlorinated Co layers by hfacH at elevated surface temperature, as reported in Ref. 38 and 39. As pointed out by Kanarik *et al.* [40], the smoothing effect seems to be an intrinsic characteristic also of thermal ALE of this type.

Our results also indicate that the etching of a metal oxide by the formation and thermal desorption of organometallic complexes should be slower or may even hardly

proceed for a crystalline metal oxide compared with an amorphous or microcrystalline metal oxide. This is because the latter has more under-coordinated metal atoms near the surface or on the grain boundaries, which are more likely to interact with incident organic molecules and form organometallic complexes.

This chapter focused on the adsorption and desorption reactions taking place on an oxidized nickel surface in a thermal ALE using hfacH organic molecules. However, they can be generalized for any metals with different organic gases, at least a β-diketone type such as acetylacetone (acacH) and trifluoroacetylacetone (tfacH) gases that are deferred for future studies. Moreover, it does not explain why the etching process ceases when a metal surface reappears after the oxidized layer is completely removed. (Therefore the etching process is called self-limiting.) The earlier study [1] indicates that hfacH molecules do not deprotonate and tend to decompose on a metallic Ni surface. In the same line with this study, DFT calculations of interactions between incident hfacH molecules and a metallic Ni surface using a more realistic extended surface model than that used in Ref. [1] is desirable for a better theoretical understanding of the thermal ALE process. The results of such a study are deferred to the next chapter.

4.5 References

[1] A. H. Basher, M. Krstić, T. Takeuchi, M. Isobe, T. Ito, M. Kiuchi, K. Karahashi, W. Wenzel, and S. Hamaguchi, J. Vac. Sci. Technol. A 38, 022610 (2020).

[2] TURBOMOLE V7.3.1 2018, a development of University of Karlsruhe and Forschungszentrum Karlsruhe GmbH, 1989-2007, TURBOMOLE GmbH, since 2007; available from http://www.turbomole.com.

[3] K. Fink, J. Phys. Chem. Chem. Phys. 7, 2999 (2005).

[4] H. Li, K. Karahashi, P. Friederich, K. Fink, M. Fukasawa, A. Hirata, K. Nagahata, T. Tatsumi, W. Wenzel, and S. Hamaguchi, J. Vac. Sci. Technol. A, 35, 05C303 (2017).

[5] V.E. Henrich and P.A. Cox. *The Surface Science of Metal Oxides*, Cambridge University Press, Cambridge (1994).

[6] V. Butera and M. C. Toroker, Materials 10, 480 (2017).

[7] K. Persson, Materials Data on NiO (SG:225) by Materials Project. United States: N. P., 2014. Web. doi:10.17188/1193796.

[8] T. Archer, C. D. Pemmaraju, S. Sanvito, C. Franchini, J. He, A. Filippetti, P. Delugas, D. Puggioni, V. Fiorentini, R. Tiwari, and P. Majumdar, Phys. Rev. B 84, 115114 (2011).

[9] F. Tran, R. Laskowski, P. Blaha, and K. Schwarz, Phys. Rev. B 75, 115131 (2007)

[10] F. Fiévet, P. Germi, F. de Bergevin and M. Figlarz, J. Appl. Cryst. 12, 387 (1979).

[11] S. Nakagomi, T. Yasuda, and Y. Kokubun, Phys. Status Solidi. B, 1900669 (2019).

[12] J. P. Perdew and Y. Wang, Phys. Rev. B 45, 13244 (1992).

[13] J. P. Perdew, K. Burke, and M. Ernzerhof, Phys. Rev. Lett. 77, 3865 (1996).

[14] J. P. Perdew, K. Burke, and M. Ernzerhof, Phys. Rev. Lett. 78, 1396 (1997).

[15] J. Tao, J. P. Perdew, V. N. Staroverov, and G. E. Scuseria, Phys. Rev. Lett. 91, 146401 (2003).

[16] A. Schäfer, H. Horn and R. Ahlrichs, J. Chem. Phys. 97, 2571 (1992).

[17] F. Weigend, M. Häser, H. Patzelt and R. Ahlrichs, Chem. Phys. Lett. 294, 143 (1998).

[18] S. Grimme, J. Antony, S. Ehrlich, and H. Krieg, J. Chem. Phys. 132, 154104 (2010).

[19] S. Grimme, S. Ehrlich, and L. Goerigk, Theory. J. Comput. Chem. 32, 1456 (2011).

[20] E. R. Johnson, and A. D. Becke, J. Chem. Phys., 123, 024101 (2005).

[21] F. Weigend and A. Baldes, J. Chem. Phys. 133, 174102 (2010).

[22] K. Eichkorn, O. Treutler, H. Öhm, M. Häser and R. Ahlrichs, Chem. Phys. Lett. 242, 652 (1995).

[23] K. Eichkorn, F. Weigend, O. Treutler and R. Ahlrichs, Theor. Chem. Acc. 97, 119 (1997).

[24] M. Sierka, A. Hogekamp and R. Ahlrichs, J. Chem. Phys. 118, 9136 (2003).

[25] M. da Silva, L. Santos, and E. Giera, J. Chem. Thermodynamics 39, 361 (2007).

[26] K. Manbeck, N. Boaz, N. Bair, A. Sanders, A. Marsh, J. Chem. Educ. 88, 1444 (2011).

[27] S. Engmann, B. Ómarsson, M. Lacko, M. Stano, Š. Matejcík, and O. Ingólfsson, J. Chem. Phys. 138, 234309 (2013).

[28] D. L. Howard, H. G. Kjaergaard, J. Huang, and M. Meuwly, J. Phis. Chem. A 119, 7980 (2015).

[29] H. Kung and A. Teplyakov, J. Catalysis 330, 145 (2015).

[30] M. Ernzerhof and G. E. Scuseria, J. Chem. Phys. 110, 5029 (1999).

[31] A. D. Becke, J. Chem. Phys. 98, 5648 (1993).

[32] C. Lee, W. Yang, R.G. Parr, Phys. Rev. B 37, 785 (1988).

[33] V. Vetere, C. Adamo, and P. Maldivi, Chem. Phys. Lett. 325, 99 (2000).

[34] S.H. Vosko, L. Wilk, and M. Nusair, Can. J. Phys. 58, 1200 (1980).

[35] P.J. Stephens, F.J. Devlin, C.F. Chabalowski, M.J. Frisch, J. Phys. Chem. 98, 11623 (1994).

[36] P. Verma, and D. G. Truhlar, Theor. Chem. Acc. 135, 182 (2016).

[37] H. L. Nigg and R. I. Masel, J. Vac. Sci. Technol. A 17, 3477 (1999).

[38] T. Ito, K. Karahashi, and S. Hamaguchi, in Proceedings of the 39th International Symposium on Dry Process, Tokyo, Japan, 16–17 November 2017, edited by K. Kinoshita et al. (DPS Organizing Committee, 2017), Vol. E-4, p. 45.

[39] J. Zhao, M. Konh, and A. V. Teplyakov, Appl. Surf. Sci. 455, 438 (2018).

[40] M. Konh, C. He, X. Lin, X. Guo, V. Pallem, R. Opila, A. Teplyakov, Z. Wang, and B. Yuan, J. Vac. Sci. Technol. A 37, 021004 (2019).

[41] K. J. Kanarik, S. Tan, and R. A. Gottscho, J. Phys. Chem. Lett. 9, 4814 (2018).

CHAPTER 5:

Self-Limiting Processes in Thermal Atomic Layer Etching (ALE) of Nickel by Hexafluoroacetylacetone *

---

* Abdulrahman H. Basher, Ikutaro Hamada, and Satoshi Hamaguchi, "Self-limiting processes in thermal atomic layer etching (ALE) of nickel by hexafluoroacetylacetone," Jpn. J. Appl. Phys., (*in press* 2020). https://doi.org/10.35848/1347-4065/aba9a7

5.1 Introduction

The self-limiting processes – a process in which etching is automatically terminated without any adjustment of the process condition – can be considered as the hallmark of the thermal atomic layer etching (ALE) from other etching methods.

In thermal ALE of metallic Ni by hfacH gas, the surface of metallic Ni is modified, mostly oxidized, and the modified surface Ni layers are etched by hfacH molecules by formation and desorption of $Ni(hfac)_2$, the detailed processes of which are illustrated in the last chapter. In this chapter, we describe the adsorption and chemical reactions of hfacH molecule on a metallic surface; we show that deprotonation and thus the formation of $Ni(hfac)_2$ is unlikely on a metallic Ni, thereby clarifying the mechanism of the self-limiting process in thermal ALE

The stability of an hfacH molecule on a model Ni surface (Ni cluster) is discussed in chapter 3 [1] and it is shown that when an hfacH molecule approaches a metallic Ni surface, its C and F atoms are bonded with surface Ni atoms. An hfacH molecule is unlikely to be deprotonated to form $hfac^-$, thereby hindering the formation of $Ni(hfac)_2$. It is more likely to be dissociated, in agreement with the experimental observation [2,3]. In the previous study, however, the Ni surface was modeled by using a monolayer Ni cluster and therefore the metallic nature of Ni may not be captured. Furthermore, the possibility of deprotonation of the hfacH molecule has not been discussed. To discuss the probabilities of deprotonation and dissociation more quantitatively, we decided to perform periodic DFT calculations of an hfacH molecule on metallic Ni surfaces, and investigate the thermodynamic stability of hfacH, possible dissociated products, and reaction pathway of hfacH on a Ni surface.

5.2 Methodology

All the periodic DFT calculations in this chapter were performed by using the STATE code [4-7]. The rev-vdW-DF2 [8,9], a variant of vdW-DF [10-13], was used for the exchange-correlation functional. The rev-vdW-DF2 has been shown to describe the adsorption state of molecules on metal surfaces accurately [6,7,14-19]. Ionic cores were represented by using the ultra-soft pseudopotentials [20]. A plane-wave basis set was used to expand the valence electron states with the kinetic energy cutoffs of 36 Ry and 400 Ry for wave-functions and augmentation charge, respectively. The Ni (100), (110), and (111) surfaces were modeled by using a repeated slab model with four atomic layer-thickness with the two bottommost atomic layers fixed to its bulk configuration, while the two upper layers were relaxed. (4 × 4) surface unit cells were used for Ni (100), (110), and (111) surfaces. The optimized lattice constant of 3.50 Å obtained using the rev-vdW-DF2 functional is in good agreement with that obtained using the full-potential linearized augmented wave method and rev-vdW-DF2 [21] as well as the experimental result reported in Ref. [22]. The convergence criterion for forces acting on atoms in the structural optimization was set to 5.14×10^{-2} eV/Å (10^{-3} Hartree/Bohr).

In this study, we used enol hfacH, which is more stable than the keto-type by –0.285 eV/molecule[1,23,24]. The adsorption of enol hfacH was evaluated on Ni (100), (110), and (111) surfaces. The adsorption/reaction energy (E_{react}) of an hfacH molecule on a Ni surface is defined by

$$E_{\mathrm{react}} = E_{\mathrm{total}} - E_{\mathrm{ad}} - E_{\mathrm{surf}}, \qquad (5.1)$$

where E_{total} is the total energy of the system with a molecule adsorbed on a Ni model surface, E_{ad} is the total energy of an hfacH molecule prior to the interaction, and E_{surf} is the total energy of a Ni surface model prior to the interaction.

The climbing image nudged elastic band (CINEB) method [25,26] was used to investigate the reaction pathway and evaluate the activation energies for deprotonation and decomposition of hfacH on Ni. A transition state was typically identified by finding a replica with the highest energy in between the initial and final states with the maximum force below 5.14×10^{-2} eV/Å.

5.3 Results and discussion

In this work, we started by investigating the adsorption state of an hfacH molecule on the Ni (100), (110), and (111) surfaces by placing an hfacH molecule at various adsorption sites on the surfaces and performing structural optimization. The energies of most stable adsorption sites on (100), (110), and (111) surfaces were found to be –0.637 eV, –1.189 eV, and –0.419 eV, respectively, when hfacH approached to the surfaces vertically and its oxygen atoms closer to the surfaces as shown in Figs. 5-1, 5-2, and 5-3. The result that the (110) surface is most reactive among the facets considered agrees with Refs. [27,28]. This result also may explain why Nigg and Masel used Ni (110) in their experiments [2]. We decided to focus on the interaction between the hfacH molecule with a Ni (110) surface only since it has the lowest physisorption energy. The adsorption structure of the hfacH molecule on Ni(110) is shown in Fig. 5-2. We also performed calculations by using the PBE functional [29,30], which is not able to describe the vdW

forces properly, and obtained the adsorption energy of –0.41 eV. This confirms the important role of vdW forces in the adsorption of the hfacH molecule.

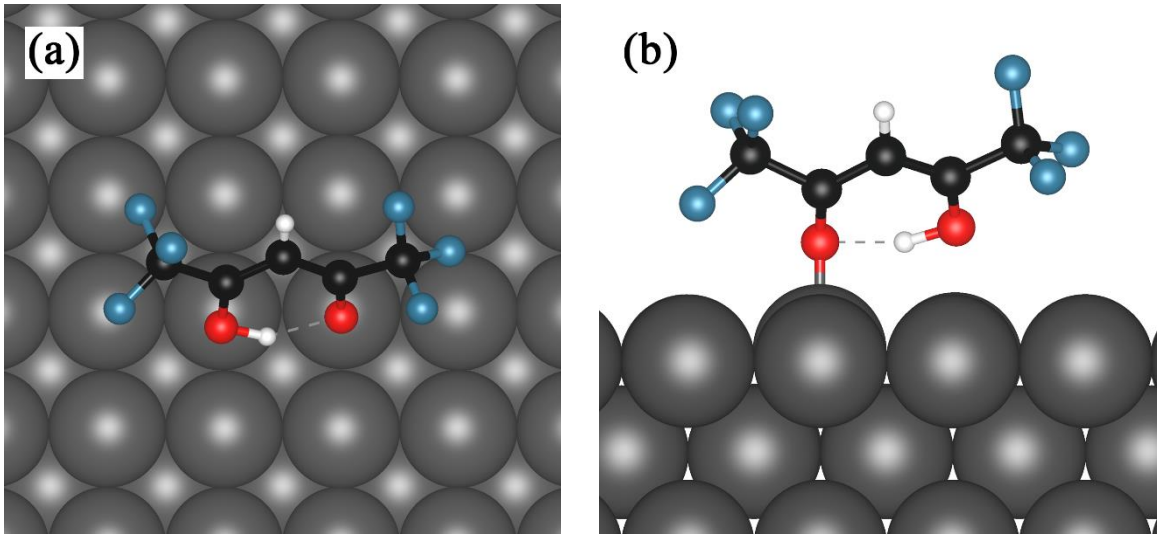


Fig. 5-1: (a) Top and (b) side views of an hfacH molecule physisorbed on a Ni (100) surface.

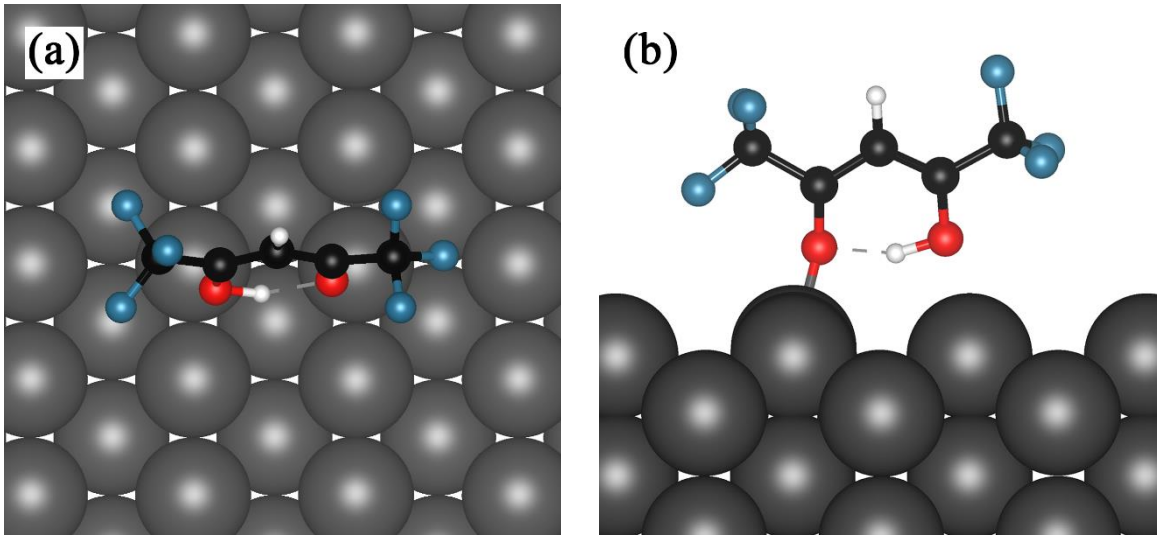


Fig. 5-2: (a) Top and (b) side views of an hfacH molecule physisorbed on a Ni (110) surface.

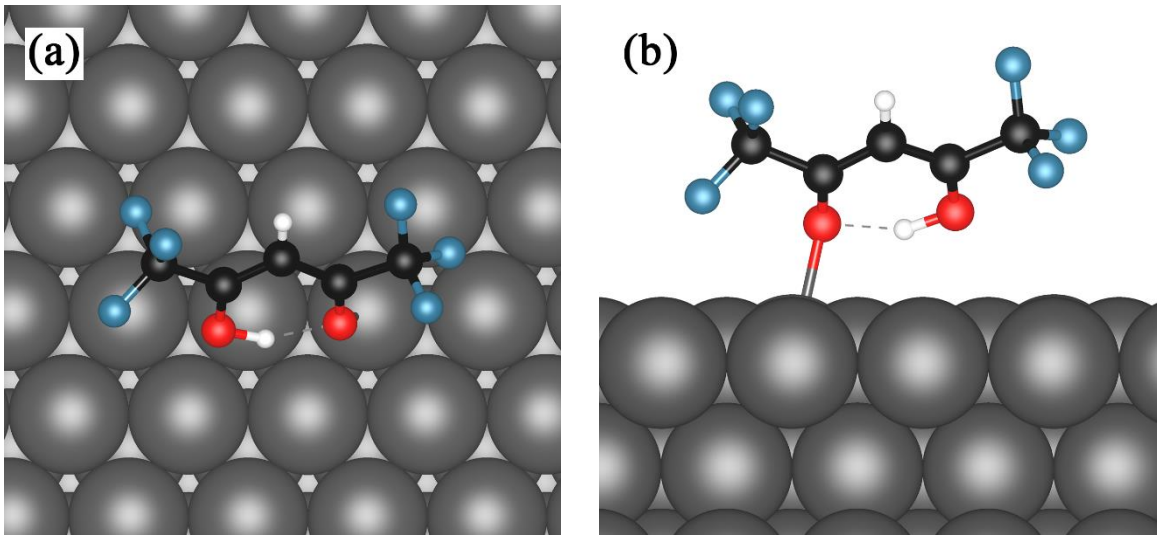


Fig. 5-3: (a) Top and (b) side views of an hfacH molecule physisorbed on a Ni (111) surface.

By further investigating the different orientation of an hfacH molecule on a Ni (110) surface, we could find chemisorption with the adsorption energy of –2.083 eV as shown in Fig. 5-4, where the angel between C, O, and Ni atoms is 88.4°, while that between C, OH, and Ni atoms is 92.9°. The calculated adsorption energy indicating that covalent type interaction is dominant in this configuration. Indeed, we calculated the charge density difference between hfacH and Ni(110) (Fig. 5-5) and found the charge accumulation between C atoms and Ni atoms underneath. Furthermore, by performing the crystal orbital overlap population analysis, we found that the lowest unoccupied molecular orbitals hybridize with the substrate Ni states and contribute to the hfacH-Ni bonding.

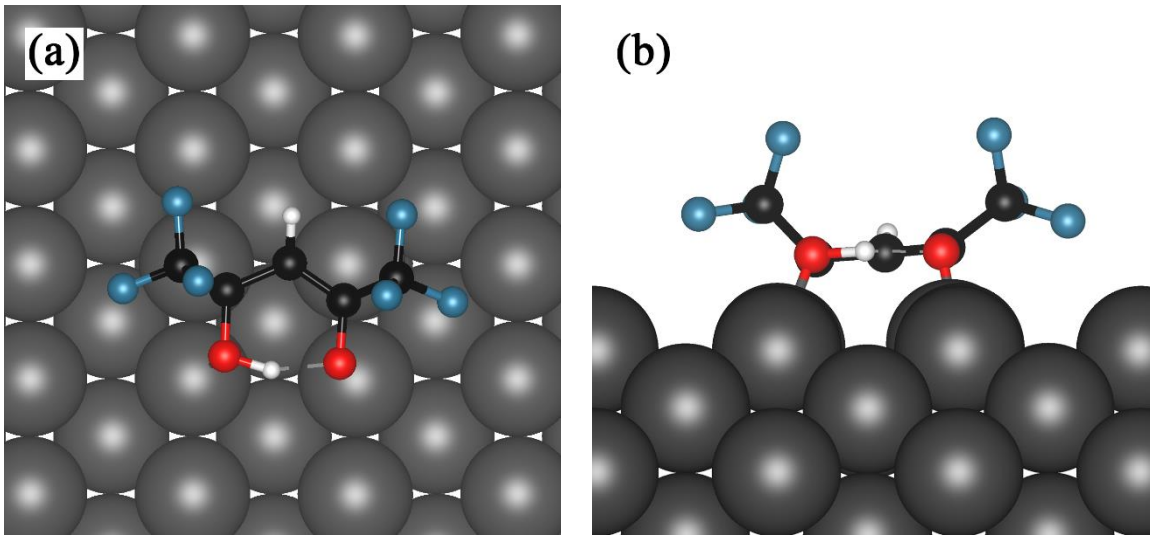


Fig. 5-4: (a) Top and (b) side views of an hfacH molecule chemisorbed on a Ni (110) surface.

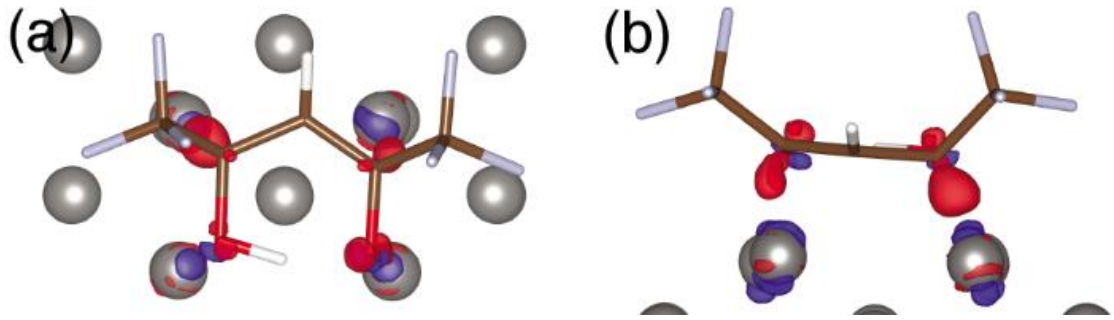


Fig. 5-5: (a) Top and (b) side views of the charge density difference of hfacH on a Ni (110) surface. The red (blue) isosurface indicates negative (positive) charge accumulation.

Then, the deprotonation of an hfacH molecule on a Ni(110) surface was investigated. The energy diagram of the deprotonation of hfacH on Ni(110) is shown in Fig. 5-6. We could not find spontaneous deprotonation during the optimization on several adoption sites, even when the H atom is closer to the surface than O atoms. Therefore, the H atom was transferred manually to the closest nickel atom in the surface to form

hexafluoroacetylacetonate anions ($hfac^-$) from chemisorption geometry and investigated the most stable deprotonated geometry (Fig. 5-6 (c)) with the adsorption energy of –1.815 eV. We then used the CINEB method to find search the transition state (Fig. 5-6 (b)) and activation barrier. The calculated adsorption energy corresponding to the transition state is -0.985 eV and the activation barrier is 1.098 eV.

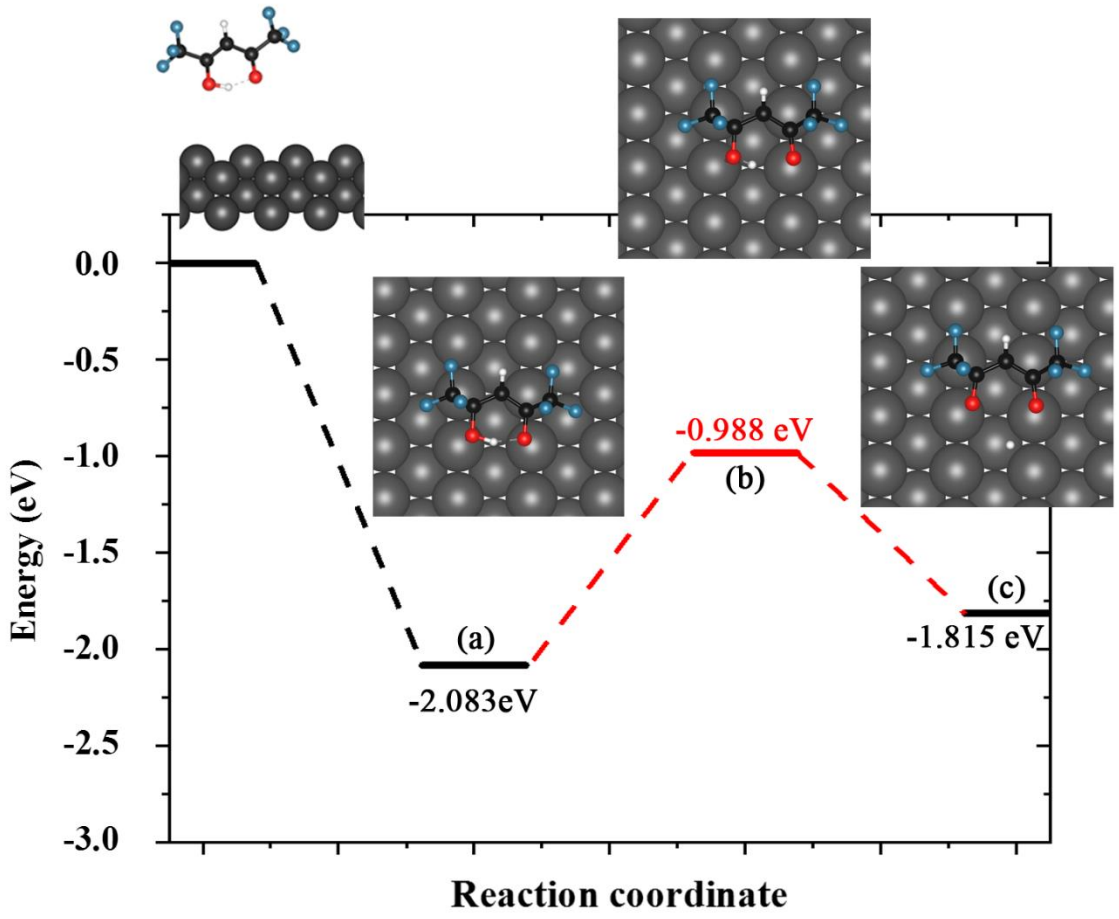


Fig. 5-6: Energy diagram of the deprotonation process of an hfacH molecule on a Ni (110) surface obtained with CINEB calculation.

When the distance between hfacH and Ni(110) in the chemisorption state is further shortened, a C-F bond was spontaneously dissociated (dissociated/defluorination) as

shown in Fig. 5-7 (c). This is one of the smallest fragments found experimentally in Ref. 2. The energy of the defluorinated hfacH on Ni(110) is –2.647 eV (Fig. 5-7 (c)). We performed a CINEB calculation and found the reaction energy of –1.056 eV at the transition state and the activation energy of 1.027, which is slightly smaller than that for the deprotonation.

By comparing the activation barriers for deprotonation and dissociation, both reactions are likely. However, the deprotonated state is energetically less stable than the dissociated state. Even more, the deprotonated state is less stable than the chemisorption state, meaning that it is thermodynamically unstable. On the other hand, the dissociated state is more stable than the intact one, and therefore it is more likely the deprotonation occurs in the etching process. These results indicate that on a metallic Ni surface, deprotonation of hfacH to form $hfac^{-}$, and hence the formation of Ni(hfac)2 is less probable, unlike the modified Ni layer, i.e., NiO layer. Instead, dissociation of hfacH occurs and therefore the self-limiting process is realized in the thermal ALE of Ni.

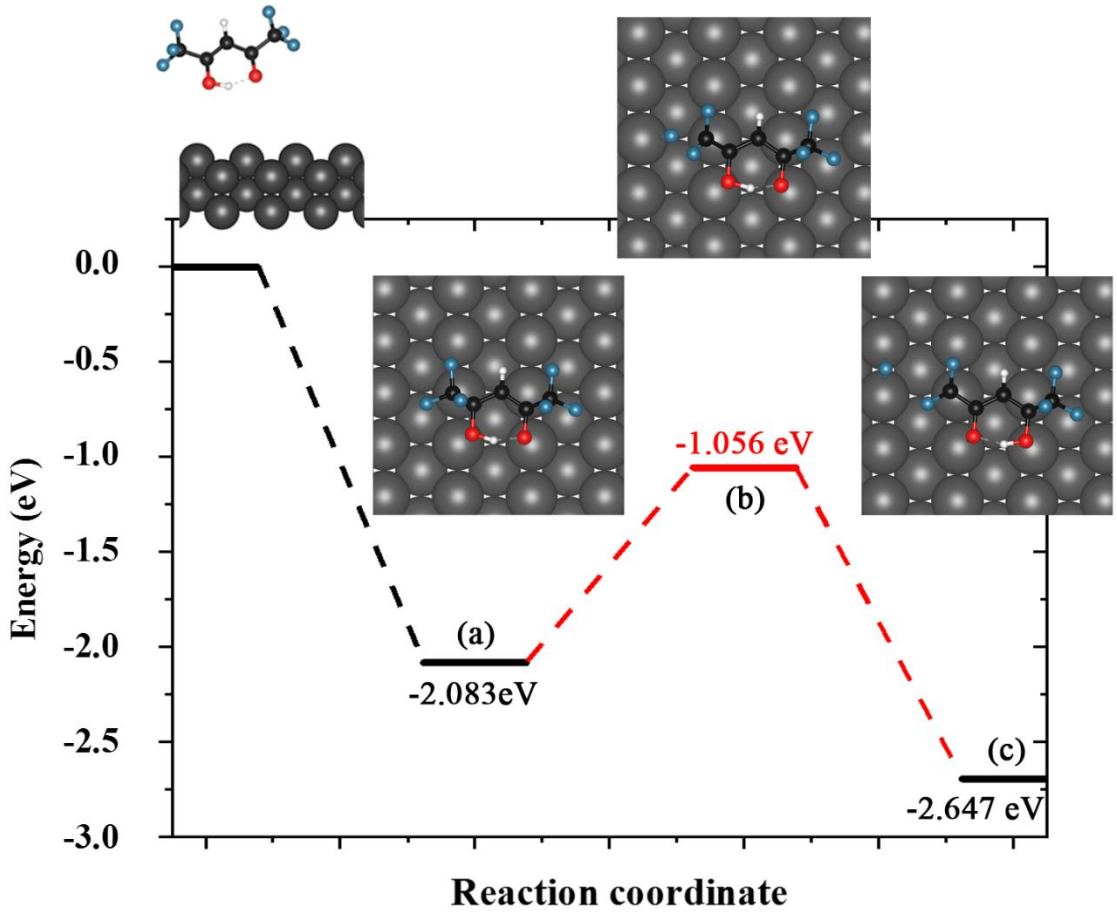


Fig. 5-7: Energy diagram of the defluorination (dissociation) process of a hfacH molecule on a Ni(110) surface obtained with the CINEB calculation.

5.4 Summary

In this study, the mechanism of the self-limiting process in thermal ALE of metallic Ni has been proposed based on the DFT calculations. Our results have illustrated that when Ni surface appears after etching of the modified Ni layer is complete, etchant hfacH is more likely to be defluorinated than to be deprotonated and to form volatile $Ni(hfac)_2$ (and finally to form H_2O molecules). Our simulations demonstrated the self-limiting nature of thermal ALE for Ni with an hfacH gas, which is consistent with earlier experimental observations

[2,3]. On the other hand, there are several small fragments of dissociated hfacH on a pure Ni surface which observed experimentally that is a subject of future study.

Finally, these mechanisms are not limited to thermal ALE for a Ni surface with hfacH molecules as an etchant gas. We anticipate that they can be generalized for other metals with different organic gases, at least a β-diketone type such as acetylacetone (acacH) and trifluoroacetylacetone (tfacH) gases.

5.5 References

[1] A. H. Basher, M. Krstić, T. Takeuchi, M. Isobe, T. Ito, M. Kiuchi, K. Karahashi, W. Wenzel, and S. Hamaguchi, J. Vac. Sci. Technol. A 38, 022610 (2020).

[2] H. L. Nigg and R. I. Masel, J. Vac. Sci. Technol. A 17, 3477, (1999).

[3] T. Ito, K. Karahashi, and S. Hamaguchi, in Proceedings of the 39th International Symposium on Dry Process, Tokyo, Japan, 16–17 November 2017, edited by K. Kinoshita et al. (DPS Organizing Committee, 2017), Vol. E-4, p. 45.

[4] Y. Morikawa, Phys. Rev. B: Condens. Matter Mater. Phys. 51, 14802 (1995).

[5] Y. Hamamoto, I. Hamada, K. Inagaki, and Y. Morikawa, Phys. Rev. B: Condens. Matter Mater. Phys. 93, 245440 (2016).

[6] F. Muttaqien, Y. Hamamoto, I. Hamada, K. Inagaki, Y. Shiozawa, K. Mukai, T. Koitaya, S. Yoshimoto, J. Yoshinobu, and Y. Morikawa, J. Chem. Phys. 147, 094702 (2017).

[7] F. Muttaqien, H. Oshima, Y. Hamamoto, K. Inagaki, I Hamada, and Y. Morikawa, Chem. Commun. 53, 9222 (2017).

[8] I. Hamada, Phys. Rev. B: Condens. Matter Mater. Phys. 89, 121103 (2014).

[9] M. Callsen and I. Hamada, Phys. Rev. B 91, 195103 (2015).

[10] D.C. Langreth, M. Dion, H. Rydberg, E. Schröder, P. Hyldgaard, and B.I. Lundqvist, Int. J. Quantum Chem. 101, 599 (2004).

[11] M. Dion, H. Rydberg, E. Schröder, D.C. Langreth, and B.I. Lundqvist, Phys. Rev. Lett. 92, 246401 (2004).

[12] D.C. Langreth, B.I. Lundqvist, S.D. Chakarova-Käck, V.R. Cooper, M. Dion, P. Hyldgaard, A. Kelkkanen, J. Kleis, L. Kong, S. Li, P.G. Moses, E. Murray, A. Puzder,

H. Rydberg, E. Schröder, and T. Thonhauser, J. Phys.: Condens. Matter 21, 084203 (2009).

[13] I. Hamada and M. Tsukada, Phys. Rev. B 83, 245437 (2011).

[14] K. Berland, V.R. Cooper, K. Lee, E. Schröder, T. Thonhauser, P. Hyldgaard, and B.I. Lundqvist, Rep. Prog. Phys. 78, 066501 (2015).

[15] J. A. Garrido Torres, B. Ramberger, H. A. Früchtl, R. Schaub, and G. Kresse, Phys. Rev. Mater. 1, 60803 (2017).

[16] L. Yan, Y. Sun, Y. Yamamoto, S. Kasamatsu, I. Hamada, and O. Sugino, J. Chem. Phys. 149, 164702 (2018).

[17] S. E. M. Putra, F. Muttaqien, Y. Hamamoto, K. Inagaki, I. Hamada, and Y. Morikawa, J. Chem. Phys. 150, 154707 (2019).

[18] J. G. Brandenburg, A. Zen, D. Alfe, and A. Michaelides, J. Chem. Phys. 151, 164702 (2019).

[19] T. N. Pham, Y. Hamamoto, K. Inagaki, D. N. Son, I. Hamada, and Y. Morikawa, J. Phys. Chem. C 124, 2968 (2020).

[20] D. Vanderbilt, Phys. Rev. B: Condens. Matter Mater. Phys. 41, 7892 (1990).

[21] F. Tran, R. Laskowski, P. Blaha, and K. Schwarz, Phys. Rev. B 75, 115131 (2007).

[22] W. P. Davey, Phys. Rev. 25, 753 (1925).

[23] K. Manbeck, N. Boaz, N. Bair, A. Sanders, A. Marsh, J. Chem. Educ. 88, 1444 (2011).

[24] S. Engmann, B. Ómarsson, M. Lacko, M. Stano, Š. Matejcík, and O. Ingólfsson, J. Chem. Phys. 138, 234309 (2013).

[25] G. Mills, H. Jónsson, and G. K. Schenter, Surf. Sci. 324, 305 (1995).

[26] G. Henkelman, B. P. Uberuaga, and H. Jónsson, J. Chem. Phys. 113, 9901 (2000).

[27] H. Seenivasan, B. Jackson, and A. K. Tiwari, J. Chem. Phys. 146, 074705 (2017).

[28] E. S. Menkah, N. Y.Dzade, R. Tia, E. Adei, and N. H.de Leeuw, Applied Surface Science 480, 1014 (2019).

[29] J. P. Perdew, K. Burke, and M. Ernzerhof, Phys. Rev. Lett. 77, 3865 (1996).

[30] J. P. Perdew, K. Burke, and M. Ernzerhof, Phys. Rev. Lett. 78, 1396 (1997).

CHAPTER 6:

Summary

In this thesis, I have started in chapter one by giving a general introduction about atomic layer etching (ALE), its importance, and its categories. Then, the motivation of this study was reported with the literature and the objective. The first chapter is ended by showing the structure of this thesis. After that, I gave the theoretical and computational basis of the first-principles quantum mechanical (QM) programs that are used in this study in chapter two. I have shown the many-particle Schrödinger equation and how it is linked to density functional theory (DFT). The used approximations to solve the Hamiltonian of Schrödinger equation to obtain the energy are illustrated such as Born-Oppenheimer approximation, one-electron approximation, Hartree-Fock approximation, local spin density approximation, generalized gradient approximation…etc. The used type of dispersion correction is explained as well in this chapter. I finished chapter two by giving a short brief about basis functions and pseudopotential or effective core potentials (ECP). In general, the general background about atomic layer etching and proceeding processes to understand its mechanisms are given in these two chapters. The results of investigating thermal atomic layer etching (ALE) mechanisms for metals are stated and discussed in chapters three, four, and five.

In chapter three, stability of hexafluoroacetylacetone molecules on metallic and oxidized nickel surfaces in atomic-layer-etching (ALE) processes has been studied. The content of this chapter is published in JVST A [Abdulrahman H. Basher, M. Krstić, T. Takeuchi, M. Isobe, T. Ito, M. Kiuchi, K. Karahashi, W. Wenzel, and S. Hamaguchi, "Stability of hexafluoroacetylacetone molecules on metallic and oxidized nickel surfaces in atomic layer etching (ALE) Processes," J. Vac. Sci. Technol. A 38, 022610 (2020)]. In chapter three, DFT-based first-principles QM simulations were used to clarify why hfacH

can be adsorbed stably on a NiO surface while it can be dissociated on a metallic Ni surface. The used program to run the calculations of chapter three is GAUSSIAN 09 Revision D.01 that is a first-principles QM program based on the density functional theory (DFT). B3LYP functional is used with the Gaussian type atomic orbitals (AO) basis set 6-311G (d). The simulation results showed that, when a stable enol hfacH molecule approaches a NiO surface, its negatively-charged O atoms are attracted to Ni atoms of the NiO surface, where all Ni atoms are positively charged. If the distance between the hfacH molecule and the NiO surface is sufficiently short, the system becomes more stable once the H atom located between the two O atoms of hfacH is transferred to a nearby surface O atom. In this process, the dissociated H atom is positively charged and the remaining part, i.e., $hfac^-$, is negatively charged (i.e., deprotonation of hfacH). Because of this charge transfer, the two negatively-charged O atoms of $hfac^-$ are bonded more strongly with positively-charged surface Ni atoms. Once this structure is established, the adsorbed $hfac^-$ anion may be slightly tilted but will not fall down on the NiO surface. This prevents the strong interaction of its C and F atoms with surface atoms and the breakdown of the $hfac^-$ anion on the surface, as our simulation indicates. In this sense, the adsorption of $hfac^-$ anion on a NiO surface is stable.

Reciprocally, if the surface is charge neutral, every Ni surface is equally charged in a Ni metallic surface, or charge neutral. Therefore, when an hfacH molecule approaches a metallic Ni surface, there are no particular preferential sites to which it can stably attach and it is less likely to transfer its H atom or H^+ cation to the surface (i.e., to deprotonate). At room temperature or higher, accidental tilting of an hfacH molecule allows its C and F atoms to be bonded with surface Ni atoms, resulting in dissociation of hfacH on a metallic surface.

These results are qualitatively consistent with experimental observations obtained in earlier studies. The results of chapter three indicate that the adsorption of hfacH or other diketones (or even other polarized molecules) on a surface is promoted by the presence of ionic bonds (or polarization) on the surface. On an oxidized or halogenated metal surface, surface atoms are polarized, and approaching diketones may similarly deprotonate and have their O atoms bonded with positively-charged metal atoms on the surface. On a metal surface, however, such polarized molecules cannot find any preferred adsorption sites and may disintegrate when they approach the surface closely.

As discussed earlier, small surface models were employed herein to represent Ni and NiO surface for analysis via first-principles QM simulations. Furthermore, we have not yet tested various DFT functionals with dispersion interactions or basis sets with the diffuse functions. Therefore, the values of adsorption energies and other physical quantities obtained in this study should not be construed to represent the true values of a real system, where the surface size is far greater than the hfacH molecule. A more accurate evaluation of the reaction energies via DFT-based first-principles QM simulations for larger systems will be discussed in the next chapter.

Stable adsorption of hfacH is only the first step of the thermal ALE process of a metal surface. At an elevated surface temperature, adsorbed $hfac^-$ anions on a metal oxide surface form volatile organometallic complexes such as $Ni(hfac)_2$. Analysis of the formation process of such organometallic complexes is also beyond the scope of the present study and is deferred to reported results in chapter four.

In chapter four, formation and desorption of nickel hexafluoroacetylacetonate $Ni(hfac)_2$ on a NiO surface in atomic layer etching (ALE) processes have been discussed. The content of this chapter is accepted to be published in JVST A [Abdulrahman H. Basher, M. Krstić, F. Karin, T. Ito, K. Karahashi, W. Wenzel, and S. Hamaguchi, "Formation and desorption of nickel hexafluoroacetylacetonate $Ni(hfac)_2$ on a NiO surface in ALE processes," J. Vac. Sci. Technol. A, (*in press* 2020)]. In chapter four, stable adsorption of hfacH molecules on a NiO (100) surface has been examined with the possible formation of volatile organo-nickel complexes $Ni(hfac)_2$ and water molecules H_2O from the surface at elevated surface temperature, using TURBOMOLE V7.3.1 program, i.e., based on a DFT method with PBE, PBE0, and B3LYP functionals, the def2-SVP and def2-TZVP Gaussian type AO basis, and ecp-10-sdf as the effective core potential (ECP) with Grimme's D3 dispersion corrections and Becke-Johnson (BJ) damping. This chapter uses a more realistic extended NiO surface model larger than the model surface used in chapter three. We have confirmed in the new calculations in chapter four that, when an hfacH molecule approaches a NiO (100) surface, it deprotonates barrierlessly and the negatively charged O atoms of the deprotonated $hfac^-$ anion bond with positively charged Ni atoms of the surface. The nature of ionic bonds (i.e., the charge distribution) of a metal oxide surface promotes the deprotonation and adsorption of hfacH molecules. The adsorption mechanism and adsorption energy of an hfacH molecule on a NiO (100) surface obtained in this chapter are consistent with what was reported in chapter three.

We have also examined how two hfacH molecules adsorbed on a NiO surface can form a $Ni(hfac)_2$ complex at an elevated surface temperature. On a flat NiO (100) surface, two hfacH molecules can deprotonate and adsorb barrierlessly. However, we were unable

to find a (meta)stable configuration where two hfac groups bonded to a single Ni atom of the NiO surface. It seems such a configuration is unstable and two hfac groups tend to bond with different Ni atoms on the surface. This indicates that the formation of a $Ni(hfac)_2$ complex on the flat surface is very unlikely.

In the case of a rough NiO surface, some Ni atoms may protrude over their surrounding atoms and allow two hfac groups to bond to a single Ni atom without much geometrical interference. In each tested case in chapter four, the topmost Ni atom is under-coordinated and has enough space around it to capture two hfac groups stably after both hfacH molecules deprotonated. In other words, our DFT calculations have demonstrated that roughness of a NiO surface can promote the formation of organo-nickel complexes $Ni(hfac)_2$ on its surface. In earlier experiments, volatile $Ni(hfac)_2$ and H_2O desorb from the surface at a temperature of around 300 °C or higher. The lowest required energy indicated in this study for the complete desorption to occur from the adsorbed state is less than 2.0 eV in each step. However, a more quantitative study on the relation between the required energy and experimental observation is the subject of a future study.

Chapter four indicates that, in a thermal ALE process of metal consisting of an oxidation step and a removal step aided by the formation of volatile organometallic complexes, the surface roughness incidentally caused by the oxidation step may play a critical role in enhancing the thermal desorption rate of organometallic complexes in the subsequent removal step. If protruding metal atoms are preferentially removed from the surface in the desorption step, the surface roughness decreases and so may the desorption rate. In other words, thermal ALE of this type for a rough metal surface tends to increase its smoothness. This is consistent with experimental observations of surface smoothing in

a similar thermal ALE process of cobalt (Co) consisting of surface chlorination steps and removal steps of the chlorinated Co layers by hfacH at elevated surface temperature. As pointed out in earlier studies, the smoothing effect seems to be an intrinsic characteristic also of thermal ALE of this type. The results also indicate that the etching of a metal oxide by the formation and thermal desorption of organometallic complexes should be slower or may even hardly proceed for a crystalline metal oxide compared with an amorphous or microcrystalline metal oxide. This is because the latter has more under-coordinated metal atoms near the surface or on the grain boundaries, which are more likely to interact with incident organic molecules and form organometallic complexes.

In addition, chapter four focused on the adsorption and desorption reactions taking place on an oxidized metal surface in a thermal ALE using organic molecules. However, it does not explain why the etching process ceases when a metal surface reappears after the oxidized layer is completely removed. (Therefore the etching process is called self-limiting.) The earlier study in chapter three indicates that hfacH molecules do not deprotonate and tend to decompose on a metallic Ni surface. In the same line with this study, DFT calculations of interactions between incident hfacH molecules and a metallic Ni surface using a more realistic extended surface model than that used in chapter three is desirable for a better theoretical understanding of the thermal ALE process. The results of such a study are deferred to chapter five.

In chapter five, the mechanism of the self-limiting process in thermal ALE of metallic Ni has been proposed based on the DFT calculations. The content of this chapter is accepted to be published in Jpn. J. Appl. Phys. [Abdulrahman H. Basher, Ikutaro Hamada, and Satoshi Hamaguchi, "Mechanism of a self-limiting process in thermal atomic

layer etching (ALE) of a nickel surface by hexafluoroacetylacetone," Jpn. J. Appl. Phys., (in press 2020)]. Our results have illustrated that when Ni surface appears after etching of the modified Ni layer is complete, etchant hfacH is more likely to be defluorinated than to be deprotonated and to form volatile $Ni(hfac)_2$ (and finally to form H_2O molecules). Our simulations demonstrated the self-limiting nature of thermal ALE for Ni with an hfacH gas, which is consistent with earlier experimental observations. On the other hand, there are several small fragments of dissociated hfacH on a pure Ni surface which observed experimentally that is a subject of future study.

Finally, the investigated mechanisms in this study are not limited to thermal ALE for a Ni surface with hfacH molecules as an etchant gas. We anticipate that similar mechanisms are followed for other transition metals such as Fe, Co, Cu, Zn, W … etc. or even it can be generalized for more metals such as Mg, Al, Ga, … etc. Furthermore, different polarized organic gases can be used as etchants and we expect also analogous mechanisms are followed, at least a β-diketone type such as acetylacetone (acacH), trifluoroacetylacetone (tfacH), Dipivaloylmethane (DPM), Diisobutyrylmethane(DBN), and other gases. Generalizing these mechanisms for several metals with different etchants is a subject of future study.

Research Achievements

I. Refereed journals

1- **Abdulrahman H. Basher**, M. Krstić, T. Takeuchi, M. Isobe, T. Ito, M. Kiuchi, K. Karahashi, W. Wenzel, and S. Hamaguchi, "Stability of hexafluoroacetylacetone molecules on metallic and oxidized nickel surfaces in atomic layer etching (ALE) Processes," J. Vac. Sci. Technol. A 38, 022610 (2020). https://doi.org/10.1116/1.5127532

2- **Abdulrahman H. Basher**, M. Krstić, F. Karin, T. Ito, K. Karahashi, W. Wenzel, and S. Hamaguchi, "Formation and desorption of nickel hexafluoroacetylacetonate $Ni(hfac)_2$ on a NiO surface in ALE processes," J. Vac. Sci. Technol. A, (*in press* 2020). https://doi.org/10.1116/6.0000293

3- **Abdulrahman H. Basher**, Ikutaro Hamada, and Satoshi Hamaguchi, "Self-limiting processes in thermal atomic layer etching (ALE) of nickel by hexafluoroacetylacetone" Jpn. J. Appl. Phys., (*in press* 2020). https://doi.org/10.35848/1347-4065/aba9a7

II. Conference papers

1- **A. H. Basher,** M. Isobe, T. Ito, M. Kiuchi, T. Takeuchi, K. Karahashi, I. Hamada, Y. Morikawa, and S. Hamaguchi, "The mechanism of hexafluoroacetylacetone (HFAC) interaction with Ni and NiO surfaces in atomic layer etching (ALE) of

magnetic films by organic molecules," Conference paper, the 40th (DPS2018), (2018).

2- **A. H. Basher,** M. Isobe, T. Ito, M. Kiuchi, T. Takeuchi, K. Karahashi, I. Hamada, Y. Morikawa, and S. Hamaguchi, "The interaction between hexafluoroacetylacetone (HFAC) with nickel and nickel oxide surfaces for atomic layer etching (ALE) applications," Conference paper, SAPP XXII and the 11th EU-Japan Joint Symposium on Plasma Processing, (2019).

3- **A. H. Basher,** M. Isobe, T. Ito, M. Kiuchi, T. Takeuchi, K. Karahashi, and S. Hamaguchi, "Reaction of hexafluoroacetylacetone on nickel and nickel oxide surfaces and its effects on thermal atomic layer etching (ALE) processes," Conference paper, XXXIV ICPIG & ICRP-10, (2019).

4- **A. H. Basher,** M. Krstic, K. Fink, T. Takeuchi, K. Nakamura, T. Ito, M. Kiuchi, K. Karahashi, W. Wenzel and S. Hamaguchi, "Estimating the Performed Etchant of Acetylacetone and Hexafluoroacetylacetone for Dry Thermal Atomic Layer Etching (ALE) of a Nickel Oxide Surface," Conference paper, the 41st (DPS2019), (2019).

III. International conferences (Oral presentations)

1- **A. H. Basher**, M. Isobe, T. Ito, K. Karahashi, M. Kiuchi, T. Takeuchi, and S. Hamaguchi, Oral presentation at ICMAP 2018, Incheon, Korea, 24-28 July 2018.

2- **A. H. Basher**, M. Isobe, T. Ito, K. Karahashi, M. Kiuchi, T. Takeuchi, and S. Hamaguchi, Oral presentation at AVS 65th International Symposium & Exhibition, Long-Beach, USA, 21-26 Oct. 2018.

3- **A. H. Basher,** M. Isobe, T. Ito, M. Kiuchi, T. Takeuchi, K. Karahashi, I. Hamada, Y. Morikawa, and S. Hamaguchi, Oral presentation at the 40th DPS2018, Nagoya, Japan, 13-15 Nov. 2018.

4- **A. H. Basher,** M. Isobe, T. Ito, M. Kiuchi, T. Takeuchi, K. Karahashi, and S. Hamaguchi, Oral presentation at SAPP XXII and the 11th EU-Japan JSPP, Štrbské Pleso, Slovakia, 18-24 Jan. 2019.

5- **A. H. Basher,** M. Isobe, T. Ito, M. Kiuchi, T. Takeuchi, K. Karahashi, and S. Hamaguchi, Oral presentation at the XXXIV ICPIG & ICRP-10, Sapporo, Hokkaido, Japan, 14-19 July 2019.

6- Takae Takeuchi, Kana Nakamura, **Abdulrahman H. Basher**, Tomoko Ito, Kazuhiro Karahashi, and Satoshi Hamaguchi, 12th International Symposium on Atomic Level Characterizations for New Materials and Devices '19 (ALC'19), Kobe, Japan, 20-25 Oct. 2019.

7- **A. H. Basher**, I. Hamada, M. Krstić, M. Isobe, T. Ito, K. Fink, K. Karahashi, Y. Morikawa, W. Wenzel, and S. Hamaguchi, Oral presentation at AVS 66th International Symposium & Exhibition, Columbus, Ohio, USA, 20-25 Oct. 2019.

8- **A. H. Basher**, M. Krstić, M. Isobe, T. Ito, K. Fink, M. Kiuchi, K. Karahashi, T. Takeuchi, W. Wenzel, and S. Hamaguchi, Oral presentation at The 72nd Annual Gaseous Electronics Conference GEC, Collage Station-Texas, USA, 28 Oct. - 1 Nov. 2019.

IV. International conferences (Posters)

1- **A. H. Basher**, M. Isobe, T. Ito, K. Karahashi, and S. Hamaguchi, "Interaction of hexafluoroacetylacetone (HFAC) molecules with nickel or nickel oxide film surfaces for atomic-layer etching (ALE) applications," Poster at ALD/ALE2018, Incheon, Korea, 29 July -1 Aug. 2018.

2- **A. H. Basher,** M. Krstic, K. Fink, T. Takeuchi, K. Nakamura, T. Ito, M. Kiuchi, K. Karahashi, W. Wenzel and S. Hamaguchi, "Estimating the Performed Etchant of Acetylacetone and Hexafluoroacetylacetone for Dry Thermal Atomic Layer Etching (ALE) of a Nickel Oxide Surface," Poster at the 41st (DPS2019), Hiroshima, Japan, 21-22 Nov. 2019.

V. Domestic conferences (Oral presentations)

1- **A. H. Basher**, M. Isobe, T. Ito, K. Karahashi, M. Kiuchi, T. Takeuchi, I. Hamada, Y. Morikawa1 and S. Hamaguchi, Oral presentation at the 79th JSAP Autumn Meeting 2018, Nagoya, Japan, 18-21 Sep. 2018.

VI. Domestic conferences (Posters)

1- 中村花菜, **Abdulrahman H. Basher**, 伊藤智子, 唐橋一浩, 浜口智志, 竹内孝江, "Ab initio DFT Study on Surface Reaction Mechanisms of Acetyl Acetone on Ni and NiO Surfaces," 2018 年日本表面真空学会学術講演会, Kobe, Japan, 19-21 Nov. 2018.

VII. Awards, grants, and scholarships

1- **Six months scholarship** from (**JASSO**) Oct2017-April2018 to study Ph.D. degree in Osaka University (2017).

2- **One-year scholarship** from (**MEXT**) May2018 - April2019 to study Ph.D. degree in Osaka University (2018).

3- **2nd place of the best posters** in **ALD/ALE 2018** by AVS in Incheon, Korea, (2018).

4- Awarded a **PCoMS IPD fellow** to join Karlsruhe Insatiate of Technology (KIT), Germany for three months from Professional Development Consortium for Computational Materials Scientists (PCoMS) 6 Jan. - 24 March 2019.

5- Awarded **Student Travel Grant** to attend AVS 65th International Symposium & Exhibition, Long Beach, 21-26 Oct. 2018.

6- Nominated from DPS 40th 2018 to be **the best young researcher** of DPS 41st 2019, Japan.

7- Finalist for **Students Award** in SAPP XXII and the 11th EU-Japan Joint Symposium on Plasma Processing, Štrbské Pleso, Slovakia, Jan. 2019.

8- Awarded **Student Travel Grant** to attend AVS 66th International Symposium & Exhibition, Columbus, Ohio, USA, 20-25 Oct. 2019.

9- Finalist for **the Coburn & Winters Awards** in AVS 66th International Symposium & Exhibition, Columbus, Ohio, USA, 20-25 Oct. 2019.

10- Awarded **Student Travel Grant** to attend the 72nd Annual Gaseous Electronics Conference **GEC**, Collage Station-Texas, USA, Oct. 2019.

11- Finalist for **Students Award** in the 72nd Annual Gaseous Electronics Conference **GEC**, Collage Station-Texas, USA, Oct. 2019.

12- Awarded **JSPS Doctoral Fellowship** for **2 years** starting from April 2020.